Turun yliopisto
University of Turku

NIR-VIS UP-CONVERSION LUMINESCENCE IN THE Yb^{3+},Er^{3+} DOPED Y_2O_2S, ZrO_2, AND $NaYF_4$ NANOMATERIALS

Laura Pihlgren

TURUN YLIOPISTON JULKAISUJA – ANNALES UNIVERSITATIS TURKUENSIS
Sarja - ser. AI osa - tom. 502 | Astronomica - Chemica - Physica - Mathematica | Turku 2014

University of Turku

Faculty of Mathematics and Natural Sciences
Department of Chemistry
Laboratory of Materials Chemistry and Chemical Analysis
Doctoral Programme in Physical and Chemical Sciences

Supervised by

Professor Jorma Hölsä, Professor Emeritus
Jouko Kankare and Docent Mika Lastusaari
University of Turku
Department of Chemistry
Laboratory of Materials Chemistry and Chemical Analysis
FI-20014 Turku, FINLAND

Custos

Docent Mika Lastusaari
University of Turku
Department of Chemistry
Laboratory of Materials Chemistry and Chemical Analysis
FI-20014 Turku, FINLAND

Reviewed by

Professor Ulrich Kynast
University of Applied Sciences Muenster / Steinfurt Campus
Department of Chemical Engineering
D-48565 Steinfurt, GERMANY

Doctor Michael Schäferling
BAM Federal Institute for Materials Research and Testing
Department 1.10 Biophotonics
D-12489 Berlin, GERMANY

Opponent

Doctor Artur Bednarkiewicz
Polish Academy of Sciences in Wrocław
W. Trzebiatowski Institute of Low Temperature and Structure Research
PL-50-950 Wrocław 2, POLAND

The originality of this thesis has been checked in accordance with the University of Turku quality assurance system using the Turnitin OriginalityCheck service.

ISBN 978-951-29-5956-3 (PRINT)
ISBN 978-951-29-5957-0 (PDF)
ISSN 0082-7002
Painosalama Oy - Turku, Finland 2014

PREFACE

This work was carried out in the Laboratory of Materials Chemistry and Chemical Analysis, University of Turku, during the years 2004-2014 within the study program of Graduate School of Materials Research. The financial support from the Graduate School of Materials Research, Finnish Funding Agency for Technology and Innovation (Tekes), as well as Palomaa-Erikoski Fund enabled this work which is gratefully acknowledged.

I express my deep gratitude to my supervisors Prof. Jorma Hölsä, Prof. Emer. Jouko Kankare and Docent Mika Lastusaari (University of Turku) for all the help, guidance and sharing of knowledge on all aspects of this work. I wish also to thank Prof. Tero Soukka for his ideas, helpful advice and valuable guidance during all these years I have worked in the collaboration with his research team.

I also want to express my sincere thanks to Prof. Ulrich Kynast and Dr. Michael Schäferling for reviewing the thesis and for their valuable comments.

The whole staff and students of the Laboratory of Materials Chemistry and Chemical Analysis in the University of Turku earn thanks for the good working atmosphere. I wish to thank M.Sc. Emilia Palo, Dr. Iko Hyppänen, M.Sc. Marja Malkamäki, Dr. Taneli Laamanen, M.Sc. Tero Laihinen, M.Sc. Minnea Tuomisto and M.Sc. Hellen Santos for the help, discussions and good humor. Also Dr. Johanna Vuojola, M.Sc. Riikka Arppe, Dr. Terhi Riuttamäki, Dr. Katri Kuningas and M.Sc. Henna Päkkilä (Laboratory of Biotechnology, University of Turku) are thanked. Dr. Philippe Smet (LumiLab, University of Ghent) and Mr. Tiago Batalhão (Universidade de São Paulo) are acknowledged for carrying out the selected EDX spectroscopy and up-conversion luminescence measurements. Mr. Kari Loikas and Mr. Mauri Nauma (University of Turku, Chemistry Workshop) are thanked for the technical support.

I want to express my gratitude to my family: Marianne, Aaro and Annamari with her family as well as my family-in-law: Merja and Antti as well as Liisa, Elina and Jenni with their families for the encouragement and support. Finally, my husband Jukka and my daughters Jasmin and Jenny deserve the warmest thanks for all the love during these years.

Lieto, November 2014

Laura Pihlgren

ABSTRACT

Since the discovery of the up-conversion phenomenon, there has been an ever increasing interest in up-converting phosphors in which the absorption of two or more low energy photons is followed by emission of a higher energy photon. Most up-conversion luminescence materials operate by using a combination of a trivalent rare earth (lanthanide) sensitizer (*e.g.* Yb or Er) and an activator (*e.g.* Er, Ho, Tm or Pr) ion in a crystal lattice. Up-converting phosphors have a variety of potential applications as lasers and displays as well as inks for security printing (*e.g.* bank notes and bonds). One of the most sophisticated applications of lanthanide up-conversion luminescence is probably in medical diagnostics. However, there are some major problems in the use of photoluminescence based on the direct UV excitation in immunoassays. Human blood absorbs strongly UV radiation as well as the emission of the phosphor in the visible. A promising way to overcome the problems arising from the blood absorption is to use a long wavelength excitation and benefit from the up-conversion luminescence. Since there is practically no absorption by the whole-blood in the near IR region, it has no capability for up-conversion in the excitation wavelength region of the conventional up-converting phosphor based on the Yb^{3+} (sensitizer) and Er^{3+} (activator) combination.

The aim of this work was to prepare nanocrystalline materials with high red (and green) up-conversion luminescence efficiency for use in quantitative whole-blood immunoassays. For coupling to biological compounds, nanometer-sized (crystallite size below 50 nm) up-converting phosphor particles are required. The nanocrystalline ZrO_2:Yb^{3+},Er^{3+}, Y_2O_2S:Yb^{3+},Er^{3+}, $NaYF_4$:Yb^{3+},Er^{3+} and $NaRF_4$-$NaR'F_4$ (R: Y, Yb, Er) materials, prepared with the combustion, sol-gel, flux, co-precipitation and solvothermal synthesis, were studied using the thermal analysis, FT-IR spectroscopy, transmission electron microscopy, EDX spectroscopy, XANES/EXAFS measurements, absorption spectroscopy, X-ray powder diffraction, as well as up-conversion and thermoluminescence spectroscopies. The effect of the impurities of the phosphors, crystallite size, as well as the crystal structure on the up-conversion luminescence intensity was analyzed. Finally, a new phenomenon, persistent up-conversion luminescence was introduced and discussed.

For efficient use in bioassays, more work is needed to yield nanomaterials with smaller and more uniform crystallite sizes. Surface modifications need to be studied to improve the dispersion in water. On the other hand, further work must be carried out to optimize the persistent up-conversion luminescence of the nanomaterials to allow for their use as efficient immunoassay nanomaterials combining the advantages of both up-conversion and persistent luminescence.

Keywords: Yttrium oxysulfide, Zirconium oxide, Sodium yttrium tetrafluoride, Ytterbium, Erbium, Nanomaterials; Up-conversion luminescence, Whole blood

TIIVISTELMÄ

Fotonien pinoamiseen perustuvan luminesenssin (up-konversioluminesenssi) löytämisen jälkeen siitä on kiinnostuttu yhä enenevissä määrin. Up-konversioluminesenssissa yhden tai useamman matalaenergisen fotonin absorptiota seuraa korkeampienergisen fotonin emissio. Suurin osa up-konversiomateriaaleista käyttää kidehilassa olevaa, kolmenarvoisista harvinaisista maametalleista (lantanideista) koostuvaa herkistin-aktivaattori-yhdistelmää, jossa herkistin on esimerkiksi ytterbium tai erbium ja aktivaattori erbium, holmium tai praseodyymi.

Up-konversioloisteaineita voidaan käyttää useissa sovelluksissa, kuten lasereissa, näytöissä sekä arvopaperien varmenteissa. Eräs sovelluskohde on myös lääketieteellinen diagnostiikka. Kuitenkin suoraan UV-viritykseen perustuvan fotoluminesenssin käyttö esimerkiksi immunomäärityksissä on erittäin ongelmallista. Ihmisen veri absorboi voimakkaasti UV-säteilyä, kuten myös loisteaineen emissiota näkyvällä aallonpituusalueella. Lupaava menetelmä, jolla päästään eroon kokoveren absorptiosta aiheutuvasta ongelmasta, on käyttää matalaenergistä viritystä ja hyödyntää up-konversiomekanismia. Kokoveri ei absorboi lähi-infrapuna-alueen säteilyä, eli se ei kykene käyttämään up-konversiomateriaalin herkistin-aktivaattori-yhdistelmän viritysaallonpituutta.

Väitöskirjatyön tarkoitus oli valmistaa voimakkaasti punaista (ja vihreää) valoa luminoivia nanokiteisiä materiaaleja, joita voidaan käyttää kokoveren kvantitatiivisiin immunomäärityksiin. Nanokokoisia (kidekoko alle 50 nm) up-konversioloisteaineita tarvitaan, jotta ne toimisivat biologisten yhdisteiden kanssa. Nanokiteiset ZrO_2:Yb^{3+},Er^{3+}-, Y_2O_2S:Yb^{3+},Er^{3+}-, $NaYF_4$:Yb^{3+},Er^{3+}- ja $NaRF_4$-$NaR'F_4$ (R: Y, Yb, Er) -materiaalit valmistettiin poltto-, sooli-geeli-, sulate- ja kerasaostusmenetelmillä sekä solvotermisen synteesin avulla ja ne tutkittiin käyttäen termoanalyysiä, FT-IR-spektroskopiaa, läpäisyelektronimikroskopiaa, EDX-spektroskopiaa, XANES/EXAFS-mittauksia, absorptiospektroskopiaa, jauheröntgendiffraktiota sekä up-konversio- ja termoluminesenssispektroskopiaa. Lisäksi tutkittiin materiaalien epäpuhtauksien, kidekoon ja kiderakenteen vaikutusta up-konversioluminesenssin voimakkuuteen. Lopuksi esiteltiin täysin uusi ilmiö, viivästynyt up-konversioluminesenssi.

Jotta nanomateriaalit toimisivat tehokkaasti biomäärityksissä, tulee niiden hiukkaskoko ja kokojakauma optimoida. Vesiliukoisuuden parantamiseksi tulee pinnan muokkausta myös tutkia. Nanomateriaalien viivästynyt up-konversioluminesenssi vaatii myös lisätutkimusta, jotta sekä up-konversioettä viivästyneen luminesenssin edut voidaan yhdistää entistä tehokkaammissa immunomäärityksissä.

Avainsanat: Yttriumoksidi, Zirkoniumoksidi, Natriumyttriumtetrafluoridi, Ytterbium, Erbium, Nanomateriaalit, Up-konversioluminesenssi, Kokoveri

TABLE OF CONTENTS

SYMBOLS AND ABBREVIATIONS

AMP	2-amino-2-methyl-1,3-propanediol
APTE	Addition of photons by transfer of energy
CCD	Charge coupled device
CR	Cross-relaxation
c	Concentration / $moldm^{-3}$
d	Particle diameter / m
DTA	Differential thermoanalysis
E	Energy
EDTA	Ethylene diamine tetra-acetic acid
EDX	Energy-dispersive X-ray spectroscopy
Em	Emission
Er'_{Zr}	Trivalent erbium in Zr^{IV} site, single negative net charge
ESA	Excited state absorption
ETU	Energy transfer up-conversion
Exc	Excitation
EXAFS	Extended X-Ray absorption near edge structure
FT-IR	Fourier transform infrared
FWHM	Full width at half maximum
GGG	Gadolinium gallium garnet, $Gd_3Ga_5O_{12}$
GSA	Ground state absorption
HPGe	High purity germanium
I	Intensity
IR	Infrared
K	Kelvin
LD	Laser diode
LED	Light emitting diode
Ln	Lanthanide
LRET	Luminescence resonance energy transfer
LuGG	Lutetium gallium garnet, $Lu_3Ga_5O_{12}$
M	Medium
n	Number of photons required to excite the corresponding emitting level
NIR	Near infrared
No.	Number
PA	Photon avalanche
R	Rare earth
S	Strong
SEM	Scanning electron microscopy
S.H.G	Second harmonic generation
T	Temperature

TEM	Transmission electron microscopy
TG	Thermogravimetry
TGA	Thermogravimetric analysis
TL	Thermoluminescence
TPA	Two-photon absorption
TSTF	Two-step, two-frequency
UPC	Up-conversion
UV	Ultraviolet
Vis	Visible
$V_O^{\bullet\bullet}$	Oxygen vacancy, double positive net charge
W	Weak
XANES	X-ray absorption near edge structure
XPD	X-ray powder diffraction
YAG	Yttrium aluminium garnet, $Y_3Al_5O_{12}$
Yb'_{Zr}	Trivalent ytterbium in Zr^{IV} site, single negative net charge
YGG	Yttrium gallium garnet, $Y_3Ga_5O_{12}$
YSGG	Yttrium scandium gallium garnet, $Y_3Sc_2Ga_3O_{12}$
YSZ	Yttria stabilized zirconia
Z	Number of formula units per unit cell
3D	3-dimensional
λ	Wavelength / nm
β	Lattice parameter / °
θ	Bragg angle / °

1. INTRODUCTION

Luminescence is a phenomenon in which a material emits electromagnetic radiation [1]. Luminescence is due to the radiative transitions between the electronic levels characteristic to the material. The radiation is usually in the visible range, but the basic process may yield also ultraviolet (UV) or infrared (IR) radiation. Such emissions can also be described as luminescence. The conventional luminescent materials usually follow the well-known principle of the Stokes law which simply states that excitation photons are at higher energy than emitted ones or, in other words, that output energy is weaker than input photon energy.

Photon up-conversion is an anti-Stokes process generating higher-energy emission from low-energy excitation radiation [2-7]. The increase in energy is achieved by absorbing multiple (usually two or three) photons per single emitted photon. The transition from the excited energy level back to the ground level, or to another lower-lying level, produces luminescence at shorter wavelengths than the original excitation wavelength. Most up-conversion luminescence materials operate by using a combination of a trivalent rare earth (lanthanide) sensitizer (*e.g.* Yb, Er or Dy) and an activator (*e.g.* Er, Ho, Pr or Tm) ion in a crystal lattice.

The simplest up-conversion mechanism is the two-steps absorption or the ground-state absorption/excited-state absorption (GSA/ESA), in which a single ion absorbs two sequential photons (Fig. 1) [8]. The first absorption excites the ion from the ground state into an intermediate level (GSA, ground state absorption). The second absorption is by the ion in this intermediate state and is termed excited state absorption (ESA). The excitation must be high enough for the second absorption to happen within the lifetime of the intermediate excited state. Since the two-steps absorption involves only a single ion, it can occur in materials with low doping levels.

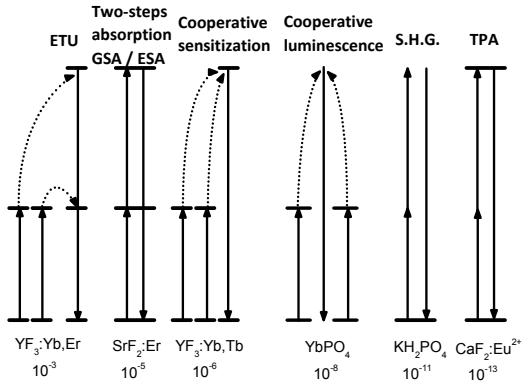

Figure 1. Various two-photon up-conversion luminescence mechanisms, examples of the materials and their typical relative quantum efficiencies (cm^2W^{-1}) [6]. The efficiencies are normalized for the incident flux.

Substantial improvement in the up-conversion efficiencies is realized by exploiting energy transfers between rare-earth ions [2-4]. This scheme is often called energy transfer up-conversion (ETU) or addition of photons by transfer of energy (APTE) (Fig. 1). Very similar mechanisms to ETU are cooperative sensitization and cooperative luminescence [4,9,10], although these are capable of much

lower conversion efficiencies. The second harmonic generation (S.H.G.; also called frequency doubling) occurs in a non-linear medium without any absorption transitions [11]. The two-photon absorption excitation (TPA) resembles the two-steps absorption process but there is no intermediate level, hence a simultaneous absorption of two photons is required [12].

Photon avalanche (PA) induced up-conversion features an unusual pump mechanism that requires a pump intensity above a certain threshold value (Fig. 2) [13,14]. For example, the threshold value for the $LiYF_4:Er^{3+}$ system is 222 mW [6]. The PA process starts with the population of the intermediate excited level E1 by non-resonant weak GSA, followed by resonant ESA to populate higher excited level E2. After the metastable level population is established, the cross-relaxation energy transfer (or ion pair relaxation) occurs between the excited ion and a neighboring ground state ion, resulting in both ions occupying the intermediate level E1. The two ions readily populate the level E2 to further initiate cross-relaxation and exponentially increase level E2 population by ESA, producing strong up-conversion emission as an avalanche process.

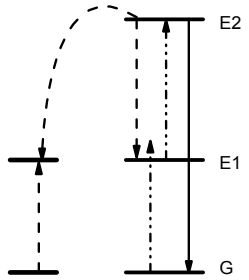

Figure 2. Photon avalanche (PA) [6]. The dashed/dotted, dashed and full arrows represent photon excitation, energy transfer and emission processes, respectively.

Different up-conversion processes may exist simultaneously [5,15,16] or the excitation process can be a mixture of two mechanisms [17]. The dominant mechanism may depend on several factors including the composition of the material, the temperature and the excitation power [18-20]. Furthermore, it is not always straightforward to identify which mechanism is in question. The following criteria have been used to distinguish the prevailing mechanism: the position of the respective energy levels of the sensitizer and activator ions; the power law dependence of the emission intensity vs. the excitation power and the sensitizer concentration; the rise and decay times of the emission as well as the shape of the excitation spectrum [5,21,22].

The up-conversion is most often a two-photon process but three-photon or higher-order up-conversion processes also occur [6,23]. Due to its multiphoton nature, the response to infrared excitation intensity is typically considered to be nonlinear. The emission intensity (I_{Em}) is proportional to a power n of the excitation intensity (I_{Ex}), where n is the number of the summed excitation photons (Eq. 1) [24].

$$I_{Em} \propto I_{Ex}^{n} \tag{1}$$

However, this has been demonstrated to be true only with reasonably low excitation powers, especially when the up-conversion process is based on energy transfer between a sensitizer and an activator ion [6,25]. The dependence on absorbed pump power decreases from the *n*:th order dependence towards linear response with increasing excitation power, regardless of the actual number of energy transfer up-conversion steps involved in the excitation process [25,26].

Since its recognition, conversion of the infrared radiation into the visible has generated much of interest in generating and incorporating novel areas of investigation. Up-converting phosphors have a variety of potential applications as lasers, diodes, displays, inks for security printing (bank notes, bonds), solar cells, enhancement of photosynthesis as well as in medical diagnostics [27-32]. One of the most sophisticated applications of lanthanide up-conversion luminescence is in diagnostic assays [33]. There are some major problems in the use of photoluminescence based on the direct UV excitation in immunoassays [34]. Human blood absorbs strongly UV radiation as well as the emission of the phosphor in the visible [35]. A promising way to overcome the problems arising from the blood absorption is to use a long wavelength excitation and benefit from the up-conversion luminescence [36]. Since there is practically no absorption by the whole-blood in the near IR region it has no capability for up-conversion in the excitation wavelength region of the conventional up-converting phosphors based on the Yb^{3+} (sensitizer) and Er^{3+} (activator) combination. In order to accomplish an efficient coupling to biological compounds, nanosized material particles are needed. Nanomaterials with high up-conversion luminescence efficiency are also required in the development of novel homogeneous label technology for quantitative all-in-one whole-blood immunoassay which uses low-cost measurement devices [37-39].

Nanoscale manipulation of lanthanide-doped up-converting nanocrystals leads to important modification of their optical properties in excited-state dynamics, emission profiles and up-conversion efficiency [40]. For example, the reduction in particle size provides the ability to modify the lifetime of intermediate states [41]. The control of spatial confinement of dopant ions within a nanoscopic region can lead to marked enhancement of a particular wavelength emission as well as generation of new types of emissions.

The aim of the present work was to study the preparation, structure and up-conversion luminescence properties of the Yb^{3+} and Er^{3+} doped Y_2O_2S, ZrO_2 and $NaYF_4$ nanomaterials as well as to compare the properties of these host materials. The nanocrystalline materials were prepared with the flux method (Y_2O_2S) [42,43], combustion [44-50] and sol-gel [51-53] synthesis (ZrO_2) as well as with the co-precipitation [54,55] and solvothermal [56-59] synthesis ($NaYF_4$). The materials' formation was studied with the thermal analysis, and the purity with the FT-IR spectroscopy. The particle morphology and the crystal structure and phase purity were studied with the transmission electron microscopy (TEM) and X-ray powder diffraction (XPD), respectively. The up-conversion luminescence and luminescence decays were studied with the NIR laser excitation (λ_{exc}: 970 nm). Also the elemental distribution (EDX) measurements were made. The effect of the luminescence intensities and the crystallite size, the crystal structure, as well as the impurities of the phosphors on the up-conversion luminescence intensity was analyzed. Finally, a new phenomenon, persistent up-conversion luminescence is introduced and discussed.

Most of the work included in this thesis has been presented in the following publications referred to as I-IX in the text.

I Hyppänen, I., Hölsä, J., Kankare, J., Lastusaari, M., and Pihlgren, L., Upconversion Properties of Nanocrystalline ZrO_2:Yb^{3+},Er^{3+} Phosphors, *J. Nanomater.*, 2007, Article ID 16391, 8 pages. doi:10.1155/2007/16391.

II Hyppänen, I., Hölsä, J., Kankare, J., Lastusaari, M., Pihlgren, L., and Soukka, T., Preparation and Up-Conversion Luminescence Properties of the $NaYF_4$:Yb^{3+},Er^{3+} Nanomaterials, *Terrae Rarae* **16** (2009) 1-6. doi: 10.3286/tr.200916.

III Hyppänen, I., Hölsä, J., Kankare, J., Lastusaari, M., and Pihlgren, L., Preparation and Characterization of Nanocrystalline ZrO_2:Yb^{3+},Er^{3+} Up-conversion Phosphors, *Ann. N.Y. Acad. Sci.* **1130** (2008) 267-271. doi: 10.1196/annals.1430.045.

IV Hyppänen, I., Hölsä, J., Kankare, J., Lastusaari, M. and Pihlgren, L., The Effect of Y^{3+} Co-Doping on the Persistent Up-Conversion Luminescence of the ZrO_2:Yb^{3+},Er^{3+} Nanomaterials, *J. Lumin.* **129** (2009) 1739-1743. doi: 10.1016/j.jlumin.2009.04.076.

V Arppe, R., Hyppänen, I., Hölsä, J., Kankare, J., Lastusaari, M., Palo, E., Pihlgren, L., Soukka, T., and Vuojola, J., Structure and Up-Conversion Luminescence of the $NaYF_4$:Yb^{3+},Er^{3+} Nanomaterials Prepared with the Solvothermal Synthesis, *manuscript*.

VI Hyppänen, I., Hölsä, J., Kankare, J., Lastusaari, M., Pihlgren, L., and Soukka, T., Up-Conversion Luminescence of the $NaRF_4$-$NaR'F_4$ (R: Y, Yb, Er) Core-Shell Nanomaterials, *J. Fluoresc.* **21** (2011) 963-969. doi: 10.1007/s10895-010-0655-8.

VII Hyppänen, I., Hölsä, J., Kankare, J., Lastusaari, M., and Pihlgren, L., Up-Conversion Luminescence Properties of the Y_2O_2S:Yb^{3+},Er^{3+} Nanophosphors, *Opt. Mater.* **31** (2009) 1787-1790. doi:10.1016/j.optmat.2008.12.034.

VIII Pihlgren, L., Laihinen, T., Rodrigues, L.C.V., Carlson, S., Eskola, K.O., Kotlov, A., Lastusaari, M., Soukka, T., Brito, H.F., and Hölsä, J., On the Mechanism of Persistent Up-Conversion Luminescence Mechanism in the ZrO_2:Yb^{3+},Er^{3+} Nanomaterials, *Opt. Mater.* **36** (2014) 1698-1704. doi: 10.1016/j.optmat.2014.01.027.

IX Harju, E., Hyppänen, I., Hölsä, J., Kankare, J., Lahtinen, M., Lastusaari, M., Pihlgren, L., and Soukka, T., Polymorphism of $NaYF_4$:Yb^{3+},Er^{3+} Up-Conversion Luminescence Materials, *Z. Kristallogr. Proc.* **1** (2011) 381-387. doi: 10.1524/zkpr.2011.0058.

2. UP-CONVERTING NANOMATERIALS

2.1. Host materials

Selection of the appropriate host materials (Table 1) is essential to obtain favorable optical properties such as high up-conversion efficiency and controllable emission profile [40].

Table 1. Oxide, halide, oxysulfide, garnet, phosphate, oxyfluoride and selected other compounds used as up-conversion luminescence host materials.

	Material	Ref.
Oxides	Y_2O_3, Gd_2O_3	44,49,60-63
	ZrO_2, TiO_2	51-53,64-66
Fluorides	$NaRF_4$, (R: Y, La-Lu)	6,54-59,67-74
	$LiYF_4$, KYF_4	75-78
	YF_3, LaF_3	6,73,79-85
	BaY_2F_8, $BaLu_2F_8$	6,86,87
	MgF_2, SrF_2, CaF_2, CdF_2	6,88
	$Pb_5Al_3F_{19}$	89
	$KLiYF_5$	90-92
Chlorides, bromides and iodides	NaCl, $BaCl_2$, $SrCl_2$, $CaCl_2$	6,93,94
	$ThCl_4$, $ThBr_4$	6,95
	$Cs_2NaGdCl_6$, Cs_2NaYCl_6, Cs_2NaYBr_6	6,21,96-98
	$CsCdBr_3$, $CsCdCl_3$, $CsMnCl_3$	6,99
	Cs_2ZrBr_6, Cs_2ZrCl_6, Cs_2GeF_6	6,100-102
	$RbCdCl_3$, $RbMnCl_3$, Rb_2CdCl_4, Rb_2MnCl_4	6,21,103
	$Cs_3Lu_2Cl_9$, $Cs_3Yb_2Cl_9$, $Cs_3Lu_2Br_9$, $Cs_3Er_2Br_9$, $Cs_3Er_2Br_9$, $Cs_3Er_2I_9$	6,99,102
	Ba_2YCl_7, Ba_2ErCl_7	6,102,104
Oxysulfides	Y_2O_2S, Gd_2O_2S, La_2O_2S	42,43,107-111
Garnets	$Y_3Al_5O_{12}$ (YAG), $Y_3Ga_5O_{12}$ (YGG), $Y_3Sc_2Ga_3O_{12}$ (YSGG), $Gd_3Ga_5O_{12}$ (GGG), $Lu_3Ga_5O_{12}$ (LuGG)	6,21,112-116
Phosphates	$YbPO_4$, $LuPO_4$, $LaPO_4$	117-120
Oxyfluorides	YOF, GdOF	121,122
Others	$LiNbO_3$, $LiTaO_3$	123-126
	TmP_5O_{14}	127,128
	$BaTiO_3$	129-131
	$La_2(MoO_4)_3$	132
	ZnS	133,134
	$NaGd(WO_4)_2$, $KYb(WO_4)_2$	6, 135,136
	$LaVO_4$, YVO_4	21,137,138
	$ZnAl_2O_4$	139
	$K_5Nd(MO_4)_4$	6
	$YAlO_3$, $GdAlO_3$	140,141

As the trivalent rare earth ions exhibit similar ionic size and chemical properties, their inorganic compounds are ideal host materials for up-converting lanthanide dopant ions [40]. In addition, alkaline earth ions (Ba^{2+},Sr^{2+},Ca^{2+}) and some transition metal ions (Zr^{IV} and Ti^{IV}) also exhibit close ionic size to lanthanide ions [105]. Therefore, inorganic compounds containing these ions (*e.g.* BaY_2F_8, SrF_2, CaF_2, ZrO_2, TiO_2) are frequently used as host materials for up-conversion processes [51-53,64-66,86-88]. However, lanthanide doping in the nanocrystals is accompanied by the formation of crystal defects such as interstitial anions and cation vacancies to maintain charge neutrality. To maintain a single crystal phase of the host for efficient up-conversion, the dopant concentration should be stringently controlled.

Ideal host materials should also have a low lattice phonon energy, which is a requirement to minimize non-radiative loss and maximize the radiative emission [18,51]. Heavy halides like chlorides, bromides and iodides generally exhibit low phonon energies of less than 300 cm^{-1}. However, they are hygroscopic and are of limited use [40,106].

Rare-earth oxysulfides (*e.g.* Y_2O_2S, La_2O_2S, Gd_2O_2S) have been known for a long time as excellent phosphor host materials and used in cathode ray tubes, field emission displays and X-ray luminescent screens [42,43,107-111]. The up-converting oxysulfide phosphor has higher up-conversion efficiency when compared to the respective oxide (same doping level and similar particle size). The enhancement in the visible up-conversion efficiency can be due to the lower phonon energy in yttrium oxysulfide, when compared to yttrium oxide.

The variation of the crystal structure in the host materials can significantly influence the optical properties of the nanocrystals [40]. For example, the hexagonal-phase $NaYF_4$:Yb^{3+},Er^{3+} bulk materials exhibit about an order of magnitude enhancement of the up-conversion efficiency relative to their cubic phase counterparts [142,143]. The phase-dependent optical property can be ascribed directly to the different crystal fields around the trivalent lanthanide ions in matrices of various symmetries [144]. Low symmetry hosts typically exert a crystal field containing more uneven components around the dopant ions compared to the high symmetry counterparts. The uneven components enhance the electronic coupling between the 4f energy levels and higher electronic configuration and subsequently increase f–f transition probabilities of the dopant ions. In addition, the decrease in the cation size (or unit-cell volume) of the host can cause an increase in the crystal field strength around the dopant ions and lead to the enhanced up-conversion efficiency. For example, the $NaYF_4$:Yb^{3+},Er^{3+} material exhibits an up-conversion luminescence two times stronger than that of $NaLaF_4$:Yb^{3+},Er^{3+}. The distance between the atoms affects also to the efficiency of the energy transfer.

The up-conversion emission color of the lanthanide-doped nanocrystals can be modified by changing the size of the nanocrystals [40,49,145]. When the crystallite size is smaller, there are more impurities (*e.g.* NO_3^-, OH^-) due to the large surface area. This increases the probability of the multiphonon relaxation. For example, in the case of the ZrO_2:Yb^{3+},Er^{3+} nanomaterial, the multiphonon relaxation weakens the green luminescence, and increases the intensity of the red luminescence. By controlling the size of the nanocrystals, also the concentration of the surface dopant ions can be precisely modulated, leading to a gradual variation in the emission color [40].

2.2. Sensitizers

In singly doped nanocrystals (*e.g.* Er^{3+} or Tm^{3+} doped), the two major parameters that affect the up-conversion processes are the distance between the two neighboring activators and the absorption cross-section of the ions [6,40]. High doping levels can lead to deleterious cross-relaxation, resulting in quenching of the excitation energy. The concentration of the activator ions should be kept low and precisely adjusted to avoid the quenching effect. In addition, most lanthanide activator ions exhibit low absorption cross-sections, leading to the low pump efficiency. Therefore, the overall up-conversion efficiency for singly doped nanocrystals is relatively low.

To enhance the up-conversion luminescence efficiency, a sensitizer with a sufficient absorption cross-section in the NIR region is usually co-doped along with the activator to take advantage of the efficient ETU process between the sensitizer and activator [6,7,40]. Trivalent ytterbium possesses an extremely simple energy level scheme with only one excited 4f level of $^2F_{5/2}$. The absorption band of Yb^{3+}, that is located around 980 nm due to the $^2F_{7/2} \rightarrow {}^2F_{5/2}$ transition, has a high absorption cross-section ($11.7 \pm 1.0 \times 10^{-21}$ cm^2) [146]. The absorption cross-section of Yb^{3+} at 980 nm is about an order of magnitude higher than that of the Er^{3+}. Commercial laser diodes are also available for this wavelength. Additionally, the $^2F_{7/2} \rightarrow {}^2F_{5/2}$ transition of Yb^{3+} is well resonant with many f–f transitions of typical up-converting lanthanide ions (Er^{3+}, Tm^{3+}, and Ho^{3+}), thus facilitating efficient energy transfer from Yb^{3+} to other ions. These optical characteristics make Yb^{3+} particularly suitable for use as an up-conversion sensitizer. The sensitizer content is normally kept high (*ca.* 20 mol-%) in doubly or triply doped nanocrystals, while the activator content is relatively low (below 2 mol-%), minimizing the cross-relaxation energy loss.

It is also found that Dy^{3+} ion can act as an sensitizer in a $YBr_3:Dy^{3+},Er^{3+}$ codoped materials [147,148]. In these materials, the Dy^{3+} ion has an absorption band ($^6H_{9/2}$) around 7700 cm^{-1} (1300 nm) higher than the ground state ($^6H_{15/2}$). The energy can then transfer to the $^4F_{9/2}$ level of Er^{3+} and finally cause a radiative transition from the $^4F_{9/2}$ to the $^4I_{15/2}$ ground level causing luminescence at 660 nm.

2.3. Activators

The requirement of the multiple metastable levels for up-conversion makes the lanthanides well-suited for this application [40,144]. To generate practically useful up-conversion emission, the energy difference between each excited level and its lower-lying intermediate level (ground level) should be close to the excitation energy to facilitate the photon absorption and energy transfer steps involved in the up-conversion processes. Er^{3+}, Tm^{3+}, and Ho^{3+} typically feature such ladder-like arranged energy levels and are thus frequently used activators.

2.3.1. Yb^{3+}/R^{3+} PAIRS

In the Yb^{3+} sensitized Er^{3+} up-conversion luminescence, the first photon of near-infrared (NIR) radiation excites the Yb^{3+} ion to the sole excited $^2F_{5/2}$ level from which the excitation may relax radiatively back to the ground $^2F_{7/2}$ level (Fig. 3) [6,22,149,150].

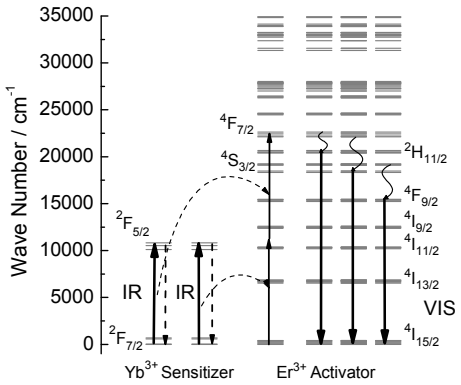

Figure 3. Schematic diagram of the Yb^{3+} sensitized Er^{3+} up-conversion luminescence [6,22,149-151]. In this figure, the excited and emitting energy levels of the activator are drawn separately for clarity. Further on, the excitations and emissions are drawn together to save space.

Taken into account the long lifetime of the excited $^2F_{5/2}$ level (typically one ms), the Yb^{3+} ion may well transfer the excitation energy to an Er^{3+} ion with higher probability than decaying radiatively. The Er^{3+} ion is promoted to the $^4I_{11/2}$ level, and further to $^4F_{7/2}$ due to the absorption and energy transfer of another NIR photon. Then Er^{3+} decays rapidly and non-radiatively to the $^2H_{11/2}$, $^4S_{3/2}$ or $^4F_{9/2}$ levels. The up-conversion emission is customarily assigned to the following transitions: green emission in the 520-580 nm region to the ($^2H_{11/2}$, $^4S_{3/2}$)→$^4I_{15/2}$ transitions and red emission in the 650-700 nm region to the $^4F_{9/2}$→$^4I_{15/2}$ transitions of the Er^{3+} ion. It should be noted that other pathways (including the initial ground (GSA) and further excited state (ESA) absorptions) may be possible involving the Er^{3+} ions only.

In the Yb^{3+}-Ho^{3+} system, the excited Yb^{3+} can transfer the energy to the Ho^{3+} ion (Fig. 4).

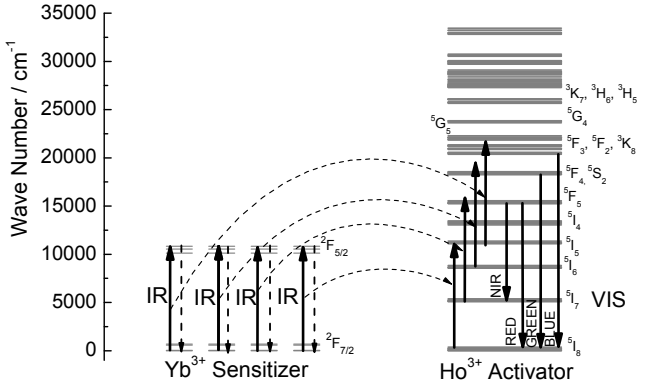

Figure 4. Schematic diagram of the Yb^{3+} sensitized Ho^{3+} up-conversion luminescence [110].

The Ho^{3+} ion is promoted to the $^5I_6$ level, and further to the $^5F_5$, $^5F_4$,$^5S_2$ or $^5F_2$,$^3K_8$ levels due to the absorption and energy transfer of additional NIR photons. The Yb^{3+}, Ho^{3+} –codoped materials produce blue, green, and red luminescence due to the following transitions: blue emission in the

region of 480 nm due to the ($^5F_2$,$^3K_8$)→$^5I_8$ transitions, green emission in the 530-580 nm region due to the ($^5F_4$,$^5S_2$)→$^5I_8$ transition, and red emission 630-680 nm due to the $^5F_5$→$^5I_8$ transition. In addition, NIR emission between 735–775 nm are attributed to the Ho^{3+} ions $^5F_4$,$^5S_2$→$^5I_7$ transition.

In the Yb^{3+} and Tm^{3+} doped materials, under the 980 nm excitation, the Yb^{3+} ion is exited from $^2F_{7/2}$ to $^2F_{5/2}$ level (Fig. 5) [142,143]. The energy can be transferred to the Tm^{3+} ion nonradiatively to excite it up to the corresponding excited level. The emission bands at 450, 475, 645, 690 and 800 nm are due to $^1D_2$→$^3F_4$ (violet), $^1G_4$→$^3H_6$ (blue), $^1G_4$→$^3F_4$ (red), $^3F_3$→$^3H_6$ (red) and $^3H_4$→$^3H_6$ (NIR) transitions of Tm^{3+} ion, respectively.

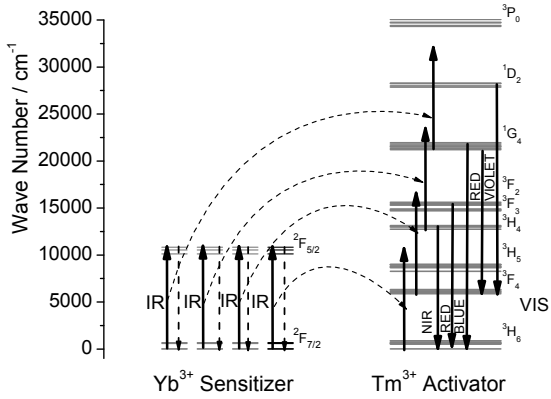

Figure 5. Schematic diagram of the Yb^{3+} sensitized Tm^{3+} up-conversion luminescence [142,143].

In the Yb^{3+}-Tb^{3+} system, two NIR photons excite two Yb^{3+} ions to the $^2F_{5/2}$ level (Fig. 6) [19]. After that, the photons may relax radiatively from this excited level back to the ground level ($^2F_{7/2}$). Alternatively, two excited photons may combine and produce co-operative luminescence, which energy is twice the energy of the $^2F_{5/2}$ level. This high energy photon then excites one Tb^{3+} ion to the $^5D_4$ level. The excited Tb^{3+} ion can then be excited to the $^5D_1$ level and relax nonradiatively to the $^5D_3$ level. Therefore, visible up-conversion emission is obtained when the Tb^{3+} ion is relaxed from the $^5D_3$ or $^5D_4$ level to the ^7F_J (J = 6, 5, 4 or 3) level.

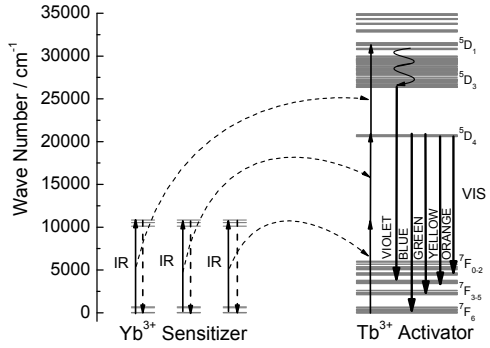

Figure 6. Schematic diagram of the Yb^{3+} sensitized Tb^{3+} up-conversion luminescence [19].

2.3.2. $Yb^{3+}/R1^{3+}/R2^{3+}$ COMBINATIONS

Utilization of varied dopant-host combinations is the most straightforward approach to the generation of multicolor up-conversion nanocrystals [40]. Typical dopant-host combinations to prepare multicolor up-conversion nanocrystals (Table 2) contain Yb^{3+} ions, which are either intentionally added or act as host lattice constituents, to absorb excitation radiation [40].

Table 2. Typical dopant-host combinations for making multicolored up-conversion nanocrystals [40].

		Major emissions* (nm)			
Dopant Yb^{3+} +	Host	Blue	Green	Red	Ref.
Tm^{3+}	α-$NaYF_4$[#]	450; 475 (S)		647 (W)	142
	β-$NaYF_4$[#]	450; 475 (S)			152
	LaF_3	475 (S)			83
	$LuPO_4$	475 (S)		649 (S)	119
Er^{3+}	α -$NaYF_4$[#]	411 (W)	540 (M)	660 (S)	142
	β -$NaYF_4$[#]		523; 542 (S)	656 (M)	152
	LaF_3		520; 545 (S)	659 (S)	83
	$YbPO_4$		526,550 (S)	657; 667 (S)	119
	Y_2O_3		525; 550 (W)	650 (S)	62
Ho^{3+}	α -$NaYbF_4$[#]		540 (S)		153
	LaF_3		542 (S)	645; 658 (M)	83
	Y_2O_3		540 (S)	650 (M)	154

*S, M, and W refer to strong, moderate and weak emission intensities, respectively.

[#]α-$NaYF_4$: cubic crystal form, β-$NaYF_4$: hexagonal crystal form.

Although different dopant-host combinations can lead to multiple up-conversion emissions, the color output that can be produced by this method is somewhat limited and associated with several apparent drawbacks. Nanoparticles in the form of different host materials can exhibit significantly different surface chemistry, while nanoparticles with different dopant ions generate only a limited number of efficient up-conversion colors upon activation with Tm^{3+}, Er^{3+}, and Ho^{3+} ions.

The up-conversion emission color also varies with the concentration of the dopant ions [40]. The dopant concentration, which determines both the relative amount of the dopant ions in the nanocrystals as well as the average distance between neighboring dopant ions, has a strong influence on the optical properties of the nanocrystals. For example, an increase in the dopant concentration of Yb^{3+} in Y_2O_3:Yb^{3+},Er^{3+} nanoparticles induces enhanced back-energy-transfer from Er^{3+} to Yb^{3+}, thereby leading to a relative increase in intensity of red emission of Er^{3+}. A similar phenomenon also has been observed in ZrO_2 nanocrystals co-doped with Yb and Er. By reducing the concentrations of the both Yb^{3+} and Er^{3+} ions, a relative decrease of the red emission intensity have observed in the $NaYF_4$:Yb^{3+},Er^{3+} nanocrystals.

The up-conversion multicolor fine-tuning in the visible spectral region can be alternatively achieved *via* a three-component dopant system (Yb^{3+}-Er^{3+}-Tm^{3+}, Yb^{3+}-Ho^{3+}-Tm^{3+}, Yb^{3+}-Tb^{3+}-Tm^{3+}, Yb^{3+}-Er^{3+}-

Tb^{3+} or Yb^{3+}-Pr^{3+}-Tm^{3+}) in a dual emission process [40,155-157]. The presence of the three activator ions with the close energy level schemes ensures effective energy transfer between these.

In the Yb^{3+} sensitized Er^{3+},Tm^{3+} up-conversion luminescence the close location of the energy levels suggests effective energy transfer between them (Fig. 8) [155]. For example, the phonon-assisted energy transfer from the $^2F_{5/2}$ energy level of Yb^{3+} to the $^3H_5$ and $^3H_4$ levels of Tm^{3+} can take place. The energy transfer from the $^2F_{5/2}$ state of Yb^{3+} to the $^4I_{11/2}$ manifold of Er^{3+} can also be expected. These two possible transfer processes would not lead to the visible photon emission. Nevertheless, if two Yb^{3+} ions are excited, such an Yb-Yb pair can transfer electron excitation energy to the $^1G_4$ state of Tm^{3+} and/or ^4F_J (J = 3/2, 5/2, 7/2) states of Er^{3+} with subsequent emission of blue light. The cooperative energy transfer mechanism can be responsible for the up-converted emission in all considered systems. Intensity of such up-converted emission should grow up with increasing laser pump energy [25,26].

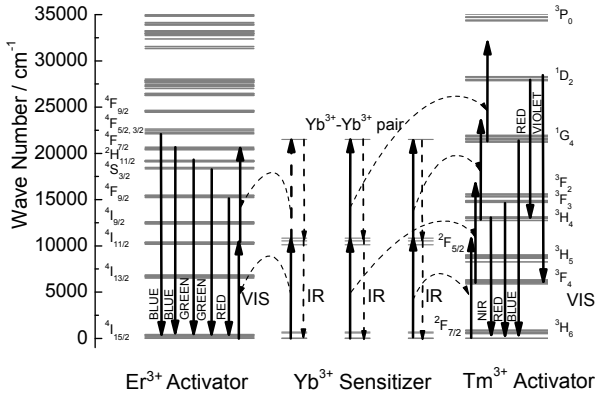

Figure 8. Schematic diagram of the Yb^{3+} sensitized Er,Tm^{3+} up-conversion luminescence [155].

The tunable red-green-blue mechanism was rooted in the nearly resonant cross-relaxation process $^1G_4$ (Tm) + $^5I_7$ (Ho)→$^3H_5$ (Tm) + $^5S_2$ (Ho) (CR2, Fig. 9) [156]. There are several reasons responsible for the occurrence of the cross-relaxation process: firstly, the energy mismatch of 135 cm^{-1} can easily be dissipated by the lattice phonons and allow this process to efficiently occur. Secondly, both the $^1G_4$ (Tm) and $^5I_7$ (Ho) states are metastable states, which have enough time to allow this process to occur. Thirdly, the rise time for the $^5S_2$ (Ho) is reduced as compared to that of Yb^{3+}/Ho^{3+} doped nanocrystals because the lifetime of $^5I_7$ (Ho) (817 μs) state is longer than that of $^1G_4$ (Tm) (550 μs) state. The blue up-conversion emission arose from Yb^{3+}/Tm^{3+} pairs mainly via a well-known three-photon process, and the green band from Yb^{3+}/Ho^{3+} pairs was a two-photon process. There is also another cross-relaxation process $^1G_4$ (Tm) + $^5I_8$ (Ho)→$^3F_4$ (Tm) + $^5S_2$ (Ho) (CR1, Fig. 9), which is responsible for the red up-conversion emission energy transfer (energy mismatch of 151 cm^{-1}). All facts have been identified by spectral and kinetic investigations, suggesting the occurrence of the proposed cross-relaxation process.

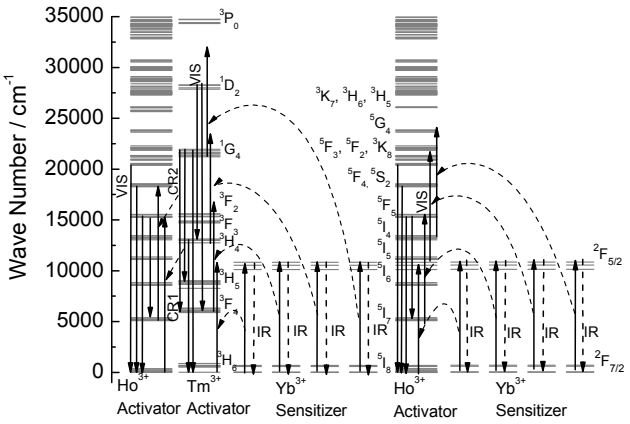

Figure 9. Schematic diagram of the Yb^{3+} sensitized Ho,Tm^{3+} up-conversion luminescence [156].

When Er^{3+} ion is substituted with Tb^{3+} ion (Fig. 10), it becomes possible that the Yb–Yb pair can effectively excite Tb^{3+} ions in their $^5D_4$ state, which is about 15 000 cm^{-1} above the nearest $^7F_0$ manifold of Tb^{3+} [155].

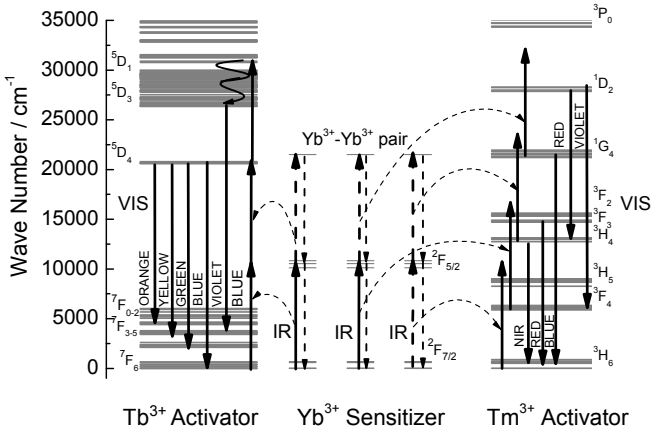

Figure 10. Schematic diagram of the Yb^{3+} sensitized Tb,Tm^{3+} up-conversion luminescence [155].

Such a large energy gap makes multiphonon relaxation to this $^7F_0$ state practically impossible, and emission of a visible photon at about 480 nm can be expected. All other processes involving energy transfer between the Yb^{3+} and Tm^{3+} ions have been described above.

If the Pr^{3+} ion is added to the Yb^{3+}/Tm^{3+} dopants pair, the ^3P_J (J = 0, 1, 2) and $^1I_6$ manifolds of Pr^{3+} ion can be excited by the Yb–Yb pair (Fig. 11) [155]. In addition, the $^1G_4$ manifold of Pr^{3+} at about 10,000 cm^{-1} can be excited by a direct energy transfer from a single Yb^{3+} ion. So, these possible processes of energy transfer allow getting up-conversion luminescence in the considered crystals, after resonant excitation of Yb^{3+} ion at 980 nm.

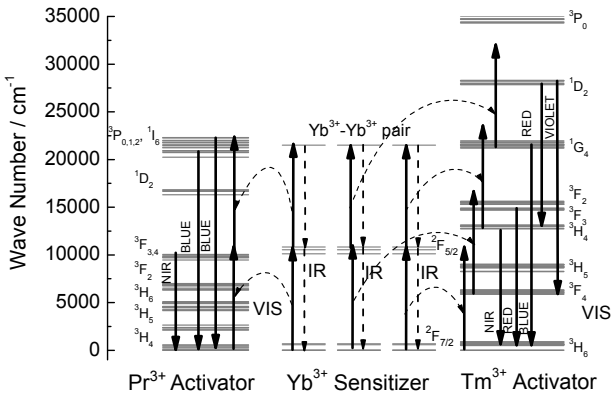

Figure 11. Schematic diagram of the Yb^{3+} sensitized Pr,Tm up-conversion luminescence [155].

Especially the Er^{3+} ions has a role in the excitation process for the up-conversion emission of Tb^{3+} ion in the Yb^{3+},Tb^{3+} co-doped materials (Fig. 12) [157].

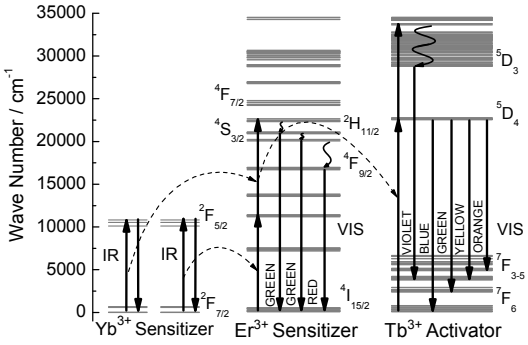

Figure 12. Schematic diagram of the Yb^{3+} and Er^{3+} sensitized Tb^{3+} up-conversion luminescence [157].

The first NIR photon excites the Yb^{3+} ion to the $^2F_{5/2}$ level (Fig. 12). The excitation may then relax radiatively back to the ground level ($^2F_{7/2}$). Alternatively, the energy can be transferred to the Er^{3+} ion. This energy can promote the Er^{3+} ion from the $^4I_{15/2}$ to the $^4I_{11/2}$ level, and if the latter is already populated a transition from the $^4I_{11/2}$ to the $^4F_{7/2}$ level can occur. The Er^{3+} ion can relax nonradiatively to the $^2H_{11/2}$, $^4S_{3/2}$ or $^4F_{9/2}$ level. Therefore, both green ($^2H_{11/2}$, $^4S_{3/2} \rightarrow {}^4I_{15/2}$) and red ($^4F_{9/2} \rightarrow {}^4I_{15/2}$) up-conversion emission is obtained. Alternatively, the energy can be transferred to the Tb^{3+} ion. This energy can promote the Tb^{3+} ion from the $^7F_6$ to the $^5D_4$ level. Excited Tb^{3+} ion can then be excited to the $^5D_1$ level and relax nonradiatively to the $^5D_3$ level. Therefore, visible up-conversion emission is obtained when Tb^{3+} ion relax from $^5D_3$ or $^5D_4$ level to the ^7F_J (J = 6, 5, 4 or 3) level. Energy transfer from Tm^{3+} $^1G_4$ level to the Tb^{3+} $^5D_4$ level and co-operative luminescence from Yb^{3+} in the Yb^{3+},Tb^{3+} co-doped materials can also enhance the Tb^{3+} up-conversion luminescence.

By adding two emitters (Tm^{3+} and Er^{3+}) with different concentration ratios, the relative intensity of the dual emissions can be precisely controlled, resulting in tunable color output from blue to white [40]. In addition, the approach was also utilized to expand the emission fine-tuning in the NIR spectral region. By increasing the concentration of Tm^{3+} ions in the $NaYF_4:Yb^{3+},Tm^{3+}$ nanocrystals, the NIR emission of Tm^{3+} can be considerably enhanced with respect to the blue emission. The phenomenon is primarily attributed to enhanced population of the $^3H_4$ level generated by the energy resonant between $^1G_4 \rightarrow {}^3H_4$ and $^3F_4 \rightarrow {}^3F_2$ at elevated dopant concentration of Tm^{3+}. Given the broad range of available dopant-host combinations, this approach as well as its complementary version of down-conversion multicolor tuning should allow generation of a large library of emission spectra in the visible and NIR spectral region that are particularly useful in multiplexed labeling.

Recently, four-color emissions have been demonstrated from $NaYbF_4:Tm^{3+}$, $NaYbF_4:Ho^{3+}$, $NaYbF_4:Er^{3+}$, and $NaYF_4:Yb^{3+}$ nanocrystals, respectively [153]. Under a single wavelength excitation at 980 nm, the nanoparticle solutions exhibit characteristic emission spectra and four different colors without the use of any color filter.

2.3.3. MULTIPHONON AND CROSS-RELAXATION

Non-radiative multiphonon relaxation rate between energy levels is an important factor that dictates the population of intermediate and emitting levels and subsequently determines the efficiency of the up-conversion process [22,151]. The prerequisites for efficient multiphonon relaxation are an energy level below the luminescent level and/or high-energy phonon. For Tb^{3+}, the energy difference between the $^4S_{3/2}$ (and $^2H_{11/2}$) levels yielding the green luminescence and the next lower level ($^4I_{9/2}$) is *ca.* 3000 (and *ca.* 3700) cm^{-1}. When the crystallite size is smaller, there exist usually more impurities (*e.g.* NO_3^-, OH^-) and the large surface area to facilitate the quenching of luminescence. The probability of the multiphonon relaxation is increased because the impurities have high phonon energies (up to 1500 and 3500 cm^{-1}) and thus less phonons (one or two) are needed for quenching. The multiphonon relaxation of the green luminescence enhances the intensity of the red luminescence by populating the $^4F_{9/2}$ level.

Another process that may affect the luminescence intensities is cross-relaxation [6,52-53,151]. For Er^{3+}, there are three possible cross-relaxation processes resulting in the quenching of the green luminescence (Fig. 7). The first process involves the $^4F_{7/2} \rightarrow {}^4F_{9/2}$ relaxation and $^4I_{11/2} \rightarrow {}^4F_{9/2}$ excitation. The energy is *ca.* 5200 cm^{-1}. In the second possible cross-relaxation process there are coupled the $^2H_{11/2} \rightarrow {}^4I_{13/2}$ relaxation and the $^4I_{15/2} \rightarrow {}^4I_{9/2}$ excitation. The energy in these two processes is *ca.* 12500 cm^{-1}. The quenching of the emission from the $^4S_{3/2}$ level proceeds through the thermally activated $^2H_{11/2}$ level. In the third process there are coupled the $^2H_{11/2} \rightarrow {}^4I_{9/2}$ relaxation and the $^4I_{15/2} \rightarrow {}^4I_{13/2}$ excitation. The energy difference related to these processes is *ca.* 6700 cm^{-1}. These two last mentioned cross-relaxation processes are competing with the green luminescence, the multiphonon relaxation and also with each other. The cross-relaxation processes of Er^{3+} is naturally favored by the rather high erbium concentration.

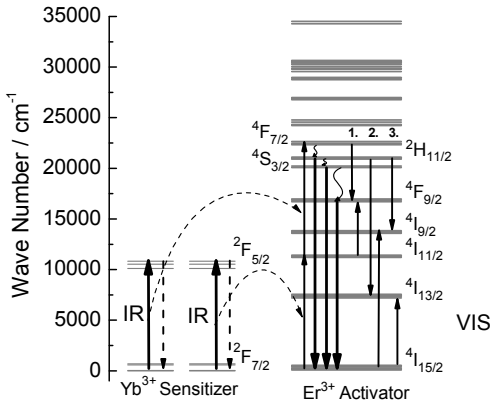

Figure 7. Cross-relaxation processes of the Yb-Er up-conversion luminescence [6,52-53,151].

2.3.4. d TRANSITION METALS

In addition to the lanthanides, some transition metals (including Ti^{2+}, Cr^{3+}, Ni^{2+}, Mo^{3+}, Re^{IV}, and Os^{IV}) are capable of photon up-conversion [6,151,158-161], but the degree of the nonradiative relaxation of the excited d-electrons is higher than that of the lanthanide f-electrons. Due to the lower up-conversion efficiency of the transition metal dopants, the usability in commercial applications are in minor relevance.

2.4. Applications

2.4.1. BIOANALYTICAL APPLICATIONS

2.4.1.1. Bioaffinity assays

Up-conversion applications have been devised for detection of cell and tissue surface antigens as luminescent bioassays [31,32,37-39]. The main advantage is that IR up-converting phosphors are excited by wavelengths (980 nm) that cannot excite the biological materials (*e.g.* blood) (Fig. 13). The main merit of the up-conversion-based assay technology is the absence of autofluorescence at visible wavelengths, which commonly deteriorates the detection limits of assays involving biological components. The autofluorescence originates from endogeneous fluorophores of biological material and is observed at wavelengths longer than the excitation radiation. However, under NIR excitation the possible autofluorescence is observed at the NIR region several hundred nanometers away from the visible wavelengths where the emission is collected (anti-Stokes shift up to 500 nm). This advantage enables, at least in theory, more sensitive bioanalytical methods as the background fluorescence can be minimized.

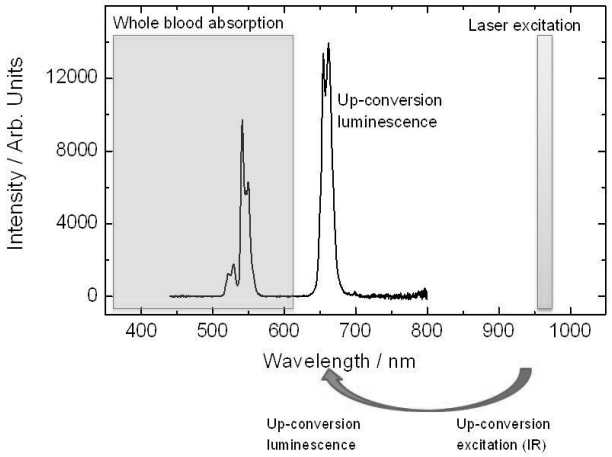

Figure 13. Excitation and emission of the up-converting particles and the absorption wavelength of the whole blood.

The operation of the bioaffinity assays relies on reversible binding events between biomolecules [162]. These recognitions may be, for example, between two proteins, between a protein and a small ligand molecule, or between nucleic acids. Often the aim is to determine the concentration of an analyte of interest. There are different ways to categorize the bioaffinity assays. One division can be made into heterogeneous and homogeneous bioaffinity assays based on how the signal from the specific binding reaction is generated. In the former type, the formed complex is physically separated from other interfering assay components with the help of one or more washing steps before measuring the signal. This requires that one of the biomolecules in the complex is bound to a solid surface. In the latter type, no washing steps are required, as the binding reaction itself causes a modulation in the signal level. Another categorization can be made to competitive and non-competitive assays based on the source of the signal. In non-competitive assays the signal arises from the labeled recognition biomolecule that is bound to the analyte of interest. In the competitive format, on the other hand, the signal typically arises from a labeled analyte analogue. This principal difference causes the dose-response curves to appear essentially opposite, so that in a non-competitive assay the signal increases, and in a competitive assay the signal decreases with increasing analyte concentration. The non-competitive format is generally considered to be the more sensitive of the two formats.

The inorganic lanthanide crystals have been proven to be useful in bioaffinity assays [162]. In addition to immunoassays, up-converting nanoparticles have been used, for example, in enzyme activity assays and DNA-hybridization assays taking advantage of the up-conversion phenomenon (Fig. 14).

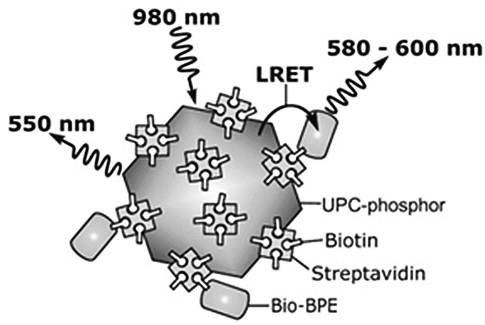

Figure 14. Principle of the competitive homogeneous up-conversion LRET assay using biotin as a model analyte [38]. Yb^{3+},Er^{3+}-doped up-conversion phosphor (donor) produces emission at 550 nm upon excitation at 980 nm.

2.4.1.2. Luminescent sensors

Chemical sensors are small instruments that respond to the presence of certain analytes by producing a measurable signal [162]. Sensors have been designed mainly for pH, temperature, oxygen, carbon dioxide, hydrogen peroxide, glucose, proteins, nucleic acids, anions, metal ions, cofactors and coenzymes. Chemical sensors usually consist of two connected units: a chemical receptor for analyte recognition, and a physicochemical transducer for producing a signal proportional to the analyte concentration. Traditionally, chemical sensors have contained organic dye molecules, such as rhodamine, as luminescent compounds. Currently, there has been increasing interest in using NIR emitting lanthanide ions and up-converting nanoparticles for better tissue penetration. Up-converting nanoparticles have been applied in sensor systems to detect *e.g.* pH [163], temperature [164], NH_3 [165], and O_2 [166].

2.4.1.3. Microscopy and imaging

The non-toxic up-converting nanoparticles are very promising for imaging applications [162]. The NIR excitation minimizes photodamage and allows deep tissue penetration. The elimination of autofluorescence resulting from the up-conversion phenomenon further increases the detection sensitivity compared to imaging applications using more traditional reporters. Additionally, up-converting nanoparticles are readily internalized by many cell types and in the imaging of blood vessels. There is currently an increasing interest towards multifunctional (dual-mode) reporters also in imaging. For example, the particulate reporters can be made electron dense, which enables their use in electron microscopy, or elements applicable for MRI (such as gadolinium) can be incorporated into the particle. As an example, gadolinium-doped UCPs have been used *in vivo* combining luminescence imaging with MRI [167].

2.4.1.4. Lateral flow assays

Both immunochromatic assays and lateral flow assays for nucleic acid detection have been demonstrated using sub-micrometer-sized up-converting particles [168]. The assay strip for UCP-based lateral flow assays consists of a sample pad, an adsorbent pad, and a nitrocellulose

membrane with specific capture molecules deposited at test and control lines. Both benchtop and portable readers for the detection of up-conversion luminescence have been developed offering a simple instrumented method to read assays and removing the possibility of human error compared to interpreting a visual strip.

2.4.2. LASERS

Because optically pumped lasers are originally based on a Stokes pumping process, one basic problem is to obtain a high-density pumping source at a shorter wavelength than their emitting wavelength [25]. At this moment, the most widely studied up-conversion laser is $LiYF_4:Er^{3+}$ where green (551 nm) and red (619, 669, 702, and 702 nm) lasing has been demonstrated by pumping into either $^4I_{9/2}$ level with wavelengths around 800 nm or the $^4I_{11/2}$ level with wavelengths around 970 nm [76].

2.4.3. DIODES

Infrared up-conversion devices generally consisted of Yb^{3+}-sensitized and Er^{3+}- or Tm^{3+}-activated fluoride phosphors and GaAs:Si light emitting diodes (LEDs) as excitation sources [169]. However, since the overall efficiency of the up-conversion display devices were generally low and inferior to that of green emitting GaP LEDs, the devices were forsaken and little attention was paid to them thereafter.

However, a 980 nm emitting laser diode (LD) has been developed for pumping an Er^{3+}-doped fiber amplifier for optical communication systems [169]. This wavelength region is also in fair agreement with the peak wavelength of Yb^{3+} ion absorption. The LD has high output (over 50 mW) and good reliability. Since the LD output light can be finely focused, adoption of LD has pronouncedly increased the infrared excitation density and also made it possible to accomplish effective optical confinement.

2.4.4. DISPLAYS

The physical mechanism on which the 3D display technology is based is known as two-step, two-frequency (TSTF) up-conversion (Fig. 15) [28]. It is crucial that the two-step excitation process in the active ion occurs from only the selective absorption of two different IR wavelengths, as it is this mechanism that enables a visible point of light to be "turned on" only where the two laser beams cross and nowhere else [28]. By controlling the spatial coordinates of the intersection of the two lasers, one can address a "voxel," or volumetric pixel, at a specific location inside the bulk imaging medium. Rapidly scanning the point of intersection around inside the display volume moves the position of the voxel and allows 3D images to be drawn.

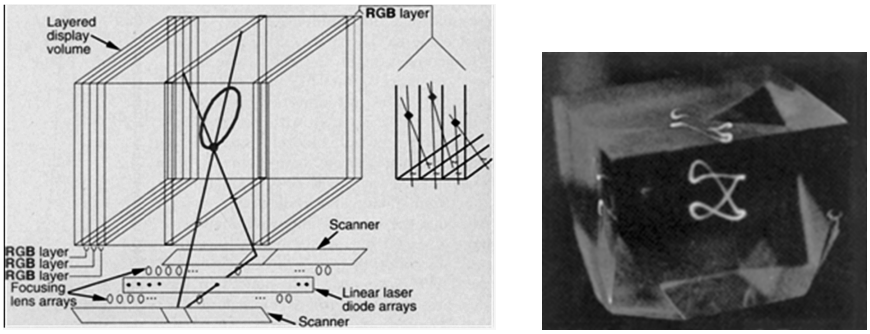

Figure 15. Layered device architecture proposed for providing wavelength-addressable red, green, and blue colors in a solid-state, 3D display (left) [28]. Photograph of a monochrome, solid-state, 3D display in a 1 cm^3 Pr^{3+}-doped sample (right) [28].

For example, the transparent host materials used for the display are heavy metal fluoride glasses doped with rare earth lanthanides: praseodymium (red), erbium (green) and thulium (blue) [28]. These glasses, the most common of which is ZBLAN (ZrF_4-BaF_2-LaF_3-AlF_3-NaF) [170], have been developed for fiber laser and optical amplifier applications and are characterized by low (below 500 cm^{-1}) phonon energies, a critical parameter leading to reduced nonradiative losses and increased up-conversion efficiencies.

2.4.5. INKS FOR SECURITY PRINTING

Security inks are specialized inks used for the purpose of authentication, anti-counterfeiting, and loss or theft prevention [29]. Up-conversion phosphors are suitable for various kinds of printing application, and can be mixed with several types of inks. These security inks can be added *e.g.* in plastics, papers, cloths, ceramics, glasses or in solutions.

Invisible inks contain unconventional dyes or pigments which become visible when exposed to an excitation light source which causes luminescence [29]. Invisible inks are a subcategory of a class of security inks. Such inks are widely used in bank notes or currency as an anti-counterfeit measure.

2.4.6. SOLAR CELLS

One of the most interesting and highly promising suggestions for a future application of the efficient up-conversion phosphors is as an active coating on solar cells for increased sun light to electric energy conversion efficiencies [21,171,172]. The application of a layer of a suitably chosen up-converting material adhered to a silicon solar cell will enable such a solar cell to indirectly utilize sub-band gap radiation (λ > 1100 nm) that would otherwise not be absorbed by the silicon. This principle was demonstrated using a silicon solar cell with a microcrystalline $NaYF_4$:Er^{3+} coating [21].

A contribution to the photocurrent extracted from the cell was found under excitation from 1500 to 1600 nm, coinciding with the Er^{3+} $^4I_{15/2}\rightarrow{}^4I_{13/2}$ transition. Even though this contribution had somewhat poor external quantum efficiency, this value is many orders of magnitude higher than the intrinsic absorption of silicon in this wavelength region. As the up-conversion process is nonlinear, a higher

excitation density will also significantly increase the efficiency of such a device. Therefore, at least in principle, an up-conversion phosphor adhered to an optimized bifacial solar cell operating under high excitation density, most likely through the use of focusing optics, may significantly increase the overall efficiency of the solar cell.

2.4.7. ENHANCEMENT OF PHOTOSYNTHESIS

An interesting biological application of up-conversion luminescence is in the photosynthesis [173]. The rate of hydrogen production with photosynthetic systems is critically dependent on the light use efficiency of the photosynthetic electron transfer chain [174-176]. In the photosynthesis, plants, algae and cyanobacteria convert light to chemical energy. The photosystems can only use photons whose energy exceeds a threshold value of approximately 1.8 eV (700 nm). Longer wavelengths are not even absorbed by chlorophylls and other photosynthetic antenna pigments. However, radiation between 400 and 700 nm represents only 44 % of total solar energy while the range above 700 nm comprises 52 %, and therefore the light use efficiency of photosynthetic systems would be greatly improved if photosynthesis could also use near-infrared (NIR) radiation. A possible method for making the energy content of NIR photons available for photosynthesis is to convert NIR radiation to visible light with the photon up-conversion mechanism [6].

3. EXPERIMENTAL

3.1. Materials preparation

3.1.1. $Y_2O_2S:Yb^{3+},Er^{3+}$

$Y_2O_2S:Yb^{3+},Er^{3+}$ materials were obtained with the flux method [42,43]. The rare earth oxide prepared with the combustion synthesis [44-50] is heated in the Na_2S_x flux composition to form the corresponding oxysulfide (Eq. 2). Suitable fluxes include sulfur and sodium carbonate.

$$Y_2O_3:Yb^{3+},Er^{3+} + 1.5Na_2CO_3 + 4S \rightarrow Y_2O_3:Yb^{3+},Er^{3+} + 1.5Na_2S_x \rightarrow Y_2O_2S:Yb^{3+},Er^{3+} + 1.5Na_2S_2O_4 \quad (2)$$

Heating of the starting materials was carried out in an Al_2O_3 crucible under static N_2 gas sphere by heating to the desired temperature and maintaining this temperature for 2 h. After the heating, the products were allowed to cool down naturally to the room temperature under the same gas sphere. The products were ground in an agate mortar and washed with deionized water to remove the $Na_2S_2O_4$ impurities. The products were also washed with an aqueous solution of acetic acid (c: 2.5 $moldm^{-3}$) to remove the rest of the impurities.

3.1.2. $ZrO_2:Yb^{3+},Er^{3+}$

3.1.2.1. Combustion synthesis

The precursor materials of $ZrO_2:Yb^{3+},Er^{3+}$ prepared with the combustion synthesis were the aqueous solutions of zirconyl nitrate ($ZrO(NO_3)_2$) as well as ytterbium and erbium nitrates ($Yb(NO_3)_3$ and $Er(NO_3)_3$, respectively) [44-50]. The nominal concentrations of Yb^{3+} and Er^{3+} were 5 or 10 and 2 or 4 mole-%, respectively, of the Zr^{IV} amount (yttrium 14, 28 or 42 mol-%). Glycine (NH_2CH_2COOH), semicarbazide ($H_2NCONHNH_2 \cdot HCl$), urea ($(NH_2)_2CO$), or 2-amino-2-methyl-1,3-propanediol (AMP, $(HOCH_2)_2C(NH_2)CH_3$) served as the fuel. Additional ammonium nitrate (NH_4NO_3) was used as an oxidizer with selected fuels. The combustion reaction was carried out in a glass reactor using a weak upward air flow. Selected products were post-annealed in air at 700 °C for 1 h if the materials' crystallinity was poor.

3.1.2.2. Sol-gel synthesis

The $ZrO_2:Yb^{3+},Er^{3+}$ nanomaterial was also prepared with the sol-gel synthesis by mixing first zirconium *n*-propoxide as the precursor in a solution of ethanol, nitric and hydrochloric acids at room temperature and stirring vigorously [51]. After that, aqueous ytterbium (10 mol-%) and erbium (4 mol-%) nitrate solutions were added. The obtained solution was stirred for 60 min, and subsequently CO_2-free distilled water was added dropwise. After the gelation, the material was dried and annealed for 6 h at 400 °C and 20 h at 1000 °C in static air in a ceramic crucible with a lid.

3.1.3. $NaYF_4:Yb^{3+},Er^{3+}$

3.1.3.1. Co-precipitation synthesis

The $NaYF_4:Yb^{3+},Er^{3+}$ nanomaterials were prepared with a co-precipitation synthesis [54]. In a typical procedure for the preparation of the $NaYF_4:Yb^{3+},Er^{3+}$ particles, 2.1 g of NaF (0.05 mol) was

first dissolved in 60 cm^3 of deionized water. Another solution was prepared by mixing together 16 cm^3 YCl_3, 3.4 cm^3 $YbCl_3$, 0.6 cm^3 $ErCl_3$ and 20 cm^3 EDTA solution. The concentration of each solution was 0.2 $moldm^{-3}$. The complex solution was injected into the NaF solution quickly, and the mixture was stirred for 1 h at room temperature. Precipitates from the reaction were centrifuged, washed three times using deionized water and once with anhydrous ethanol. The precipitates were then dried under vacuum for 24 h.

The nanocrystalline shell in the core-shell $Na(Y,Yb)F_4$-$NaErF_4$ nanomaterials was prepared with the same synthesis as the homogeneous material by dissolving first 2.1 g of NaF in 60 cm^3 of deionized water. Then dried $Na(Y,Yb)F_4$ core was mixed into this solution. The $ErCl_3$ solution (0.6 cm^3) was poured quickly into the NaF-core solution, and the mixture was stirred for 1 h at room temperature. The precipitate was centrifuged, washed and dried as above.

The annealing of the nanoparticles was carried out under a N_2 + 10 % H_2 gas sphere by heating to the desired temperature at a rate of 20 °C per minute, and maintaining this temperature for 5 h. After annealing, the products were cooled down naturally to room temperature under the same gas sphere. Selected materials were prepared without EDTA to study the effect of the EDTA amount on the particle size.

3.1.3.2. Solvothermal synthesis

Up-converting $NaYF_4$:Yb^{3+},Er^{3+} nanoparticles were also prepared with the solvothermal synthesis (Eq. 3) [56].

$$NaOH(aq) + C_{18}H_{34}O_2(l) + RCl_3(aq) + 4NaF(aq) \rightarrow$$
$$NaRF_4(s) + 3NaCl(aq) + C_{18}H_{33}O_2Na(aq) + H_2O \quad (3)$$

In a typical synthesis, NaOH (1.2 g, 30 mmol), water (9 cm^3), ethanol (10 cm^3), and oleic acid (20 cm^3) were mixed under agitation to form a homogeneous solution [56]. Then 0.6 mmol (total amounts) of rare-earth chloride (1.2 cm^3, 0.5 mol/dm^3 RCl_3, R: Y (78), Yb (20), Er (2 mol-%)) aqueous solution was added under stirring. Subsequently, 1.0 $moldm^{-3}$ aqueous NaF (4 cm^3) solution was added dropwise to the above solution. Some of the solutions became highly viscous due to a saponification reaction. The mixture (44 cm^3) was stirred for *ca.* 10 min, then transferred to a 25 cm^3 glass reactor, sealed, and hydrothermally treated at 140-185 °C for 4-12 h. The pressure of the reaction vessel was 0.9-2.0 MPa. The system was cooled to room-temperature naturally, and the products deposited at the bottom of the vessel. Cyclohexane was used to collect the products. The products were subsequently deposited by adding ethanol to the sample-containing cyclohexane solution. The resulting mixture was then centrifuged to obtain powder samples. The products were dried in a vacuum desiccator and washed with ethanol several times to remove oleic acid, sodium oleate, and other remnants.

3.2. Characterization

3.2.1. THERMAL ANALYSIS

The TG and DTA curves between 25 and 1200 °C were measured in flowing air (100 cm^3min^{-1}) with a TA Instruments SDT 2960 Simultaneous DTA-TGA thermoanalyzer with a heating rate of 5 $°Cmin^{-1}$. α-Al_2O_3 was used as both the reference and crucible material.

3.2.2. FT-IR SPECTROSCOPY

The FT-IR spectra between 400 and 4000 cm^{-1} were measured with a Mattson Instruments GALAXY 6030 or Nicolet Nexus 870 spectrometer with a 4 cm^{-1} resolution. The materials were mixed with KBr and then pressed to transparent discs.

3.2.3. PARTICLE SIZE AND MORPHOLOGY

The particle size and morphology of the materials were examined using a JEM 1200EX transmission electron microscope with a 0.14 nm resolution. The X-ray detector was a NORWAR-window Si(Li) detector. The materials were embedded in epoxy resin and cut on an ultramicrotome at 70 nm thickness.

The particle size and morphology were also studied with the Tecnai 12 Bio Twin transmission electron microscope equipped with a CCD camera. The measurement voltage was 120 kV and the resolution 0.49 nm. The materials were suspended to the 10 mM borate buffer with 0.1 % Tween-20 detergent and then added to the copper grid.

The EDX maps with the SEM images were obtained with the FEI Quanta 200 field emission scanning electron microscope with the EDAX Genesys 4000 equipment and the Sapphire Si(Li) detector.

3.2.4. X-RAY POWDER DIFFRACTION

The crystal structure and phase purity of the nanomaterials were analyzed with the X-ray powder diffraction (XPD) measurements. The patterns were collected with a Huber G670 image plate (2θ range: 4-100°) Guinier-camera ($CuK_{\alpha 1}$ radiation: 1.5406 Å). The reference patterns were calculated with the PowderCell program [177] using the crystallographic data from [178].

3.2.5. CRYSTALLITE SIZE CALCULATIONS

The crystallite size of each $ZrO_2:Yb^{3+},Er^{3+}$ nanomaterial was estimated from the diffraction data by using the Scherrer formula (Eqs. 4 and 5) [179]. In this equation, d (m) is the mean crystallite size, λ (m) the X-ray wavelength, β (rad) the full width at half maximum (FWHM) of the most appropriate reflection and θ (°) half of the Bragg´s angle (2θ). The reflection broadening due to the diffractometer set-up was eliminated from the β_s-value by using a microcrystalline reference (β_r).

$$d = \frac{0.9\lambda}{\beta\cos\theta} \tag{4}$$

$$\beta^2 = \beta_s^2 - \beta_r^2 \tag{5}$$

3.2.6. XANES / EXAFS

The XANES and EXAFS measurements were made at Hamburger Synchrotronstrahlungslabor (HASYLAB) at Deutsches Elektronen-Synchrotron (DESY) (Hamburg, Germany), Beamline C. The data was collected on the Er L_{III} and Yb L_{II} edges because Yb L_{III} could not be used due to the close proximity of Er L_{II}. Si(111) double crystal monochromator and Canberra 7 pixel High Purity

Germanium (HPGe) detector were used. The measurements were made in fluorescence mode. The EXAFS data was treated with the EXAFSPAK program suite [180].

3.2.7. ABSORPTION SPECTROSCOPY

The absorption spectra of a ZrO_2:Yb^{3+},Er^{3+} nanomaterial prepared with the sol-gel synthesis were measured with a Varian Cary 5E UV-vis-NIR spectrometer between 10 000 and 11 500 cm^{-1} at room and 10 K temperature. The material was mixed with KBr and then pressed to a disc.

The absorption spectrum of the whole blood was measured with a Shimadzu Biospec 1601 spectrometer between 9100 and 41 600 cm^{-1} at room temperature. The whole-blood solution contained 5 vol-% of blood diluted in 10×10^{-3} mol dm^{-3} Tris-HCl (pH 8.0) buffer solution.

3.2.8. UP-CONVERSION LUMINESCENCE AND LUMINESCENCE DECAY

The up-conversion luminescence spectra of the nanomaterials were measured at room temperature with an Ocean Optics PC2000-CCD spectrometer. The spectral response of the spectrometer was calibrated with an Ocean Optics LS-1-CAL-INT calibration source. The NIR excitation (970 nm) source was a HTOE FLMM-0980-711-1300m fiber-coupled IR laser diode. There was a longpass filter (850 nm, Edmund RG850) between the laser and the sample holder. The material was packed inside a capillary tube as evenly as possible. A shortpass filter (850 nm, Edmund 46386) between the sample and the detector was used to exclude the exciting radiation from the detector. Spectra were collected with the Ocean Optics OOIIrrad software. The laser diode was controlled with a Wavelength Electronics LDTC2/2. The correct absolute intensities of the luminescence spectra of the different samples were ensured by using always the same calibrated measurement practice and checking the reproducibility of individual measurements.

The decay curves were measured with the same excitation source at 650 nm. The width of the excitation pulse was 5, 20 or 40 milliseconds. After each pulse there was a 60-95 ms delay before the next pulse. One measurement consisted of 1000-10 000 pulse-delay cycles.

3.2.9. UV-VUV EXCITATION SPECTRA

The UV-VUV excitation spectra of the ZrO_2:Yb^{3+},Er^{3+} nanomaterials were measured between 3.7 and 40 eV by using synchrotron radiation (SR) at the SUPERLUMI beamline of HASYLAB at DESY (Hamburg, Germany). The samples were mounted on the cold finger of a liquid He flow cryostat. The spectra were recorded at 10 and 298 K with a 2-m McPherson type excitation monochromator attaining a resolution down to 0.02 nm. The emission spectra were obtained with a 0.3-m Acton Research Corp. Czerny-Turner-type triple-grating SpectraPro 300i monochromator (200 to 800 nm) equipped with a conventional photomultiplier (and a CCD-camera).

3.2.10. THERMOLUMINESCENCE

The thermoluminescence (TL) glow curves were measured with an upgraded Risø TL/OSL-DA-12 system using a constant heating rate of 5 °Cs^{-1} in the temperature range from 25 to 400 °C. The global TL emission from UV to 650 nm was monitored. Prior to the measurements, the samples were irradiated with a combination of Philips TL 20W/05 (emission maximum at 360 nm) and TL 20W/03

(420 nm) UV lamps for two minutes. A delay of 3 min between the irradiation and measurement was used. The analysis of the TL glow curves was carried out with the deconvolution method by using the program TLanal v.1.0.3 [181].

4. RESULTS AND DISCUSSION

4.1. Formation

4.1.1. $Y_2O_2S:Yb^{3+},Er^{3+}$

The TG curve of the precursors of the $Y_2O_2S:Yb^{3+},Er^{3+}$ nanomaterial shows the formation of the Na_2S_x flux (Fig. 16). According to the DTA curve, the formation of the flux is completed around 450 °C. The weight loss at 1100 °C indicates the decomposition of the oxysulfide back to the oxide.

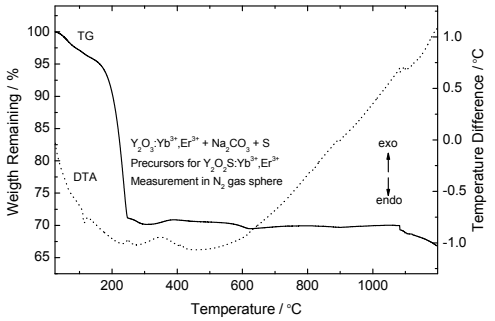

Figure 16. TG and DTA curves of the precursors of the $Y_2O_2S:Yb^{3+},Er^{3+}$ nanomaterial prepared with the flux method.

4.1.2. $ZrO_2:Yb^{3+},Er^{3+}$

The TG curve of the $ZrO_2:Yb^{3+},Er^{3+}$ nanomaterial prepared with the combustion synthesis shows the decomposition of nitrates at 250-450 °C (Fig. 17) [l].

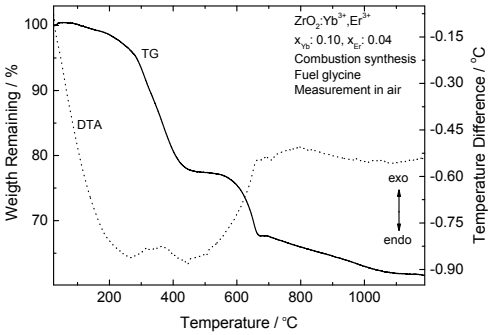

Figure 17. TG and DTA curves of the $ZrO_2:Yb^{3+},Er^{3+}$ nanomaterial prepared with the combustion synthesis [l].

A small amount of moisture is present because a low temperature weight loss is observed below 200 °C. With glycine used as the fuel, a further mass change is observed between 500 and 650 °C. This change is due to the decomposition of zirconium oxycarbonates/oxynitrates [182,183]. The exothermic signal in the DTA curve around 700 °C can be related to the appearance of a crystalline phase of $ZrO_2:Yb^{3+},Er^{3+}$ as indicated by the XPD patterns. The gradual weight loss at higher temperatures can be taken as an indication of evaporation of tightly bound species, *e.g.* OH^- groups (as water). The presence of these impurities may have a nefarious effect on the luminescence performance of these nanomaterials.

4.1.3. $NaYF_4:Yb^{3+},Er^{3+}$

The DTA curve of the $NaYF_4:Yb^{3+},Er^{3+}$ nanomaterial prepared with co-precipitation with EDTA shows an exothermic reaction at 500 °C due to the formation of the hexagonal phase from the low temperature cubic one (Fig. 18, left) [II]. Also the endothermic reaction at 665 °C due to the formation of high temperature cubic phase from the hexagonal one is observed. The DTA curve of the $NaYF_4:Yb^{3+},Er^{3+}$ nanomaterial prepared without EDTA (Fig. 18, right) shows an exothermic reaction at 440 °C and an endothermic one at 660 °C due to the phase formations described above.

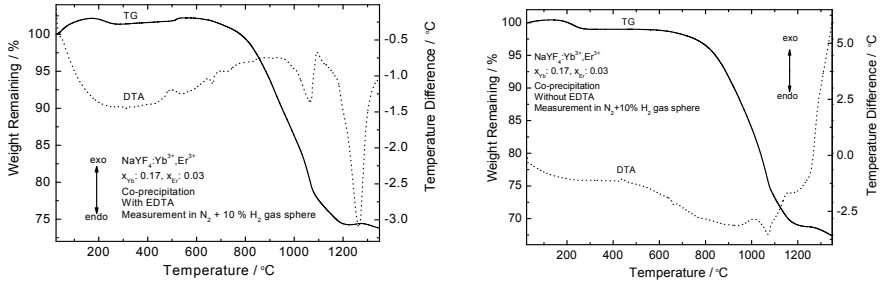

Figure 18. TG and DTA curves of the $NaYF_4:Yb^{3+},Er^{3+}$ nanomaterials prepared with co-precipitation with (left) and without EDTA (right) [II].

This revealed that the preparation of the nanomaterial with EDTA needs a higher temperature for the formation of the hexagonal phase. This might be due to the property of EDTA preventing the particle growth. The crystallite size of the hexagonal phase seems in most cases to be larger than that of the cubic ones (see Chapter 4.4.3) and because of that, higher temperatures are needed for the cubic phase changing to the hexagonal one. Finally, at 1100 °C, the materials were decomposed to NaF and Y_2O_3, and, at 1240 °C, the YF_3 compound was formed.

4.2. Materials' purity

4.2.1. $Y_2O_2S:Yb^{3+},Er^{3+}$

The FT-IR spectra of the $Y_2O_2S:Yb^{3+},Er^{3+}$ nanomaterials prepared with the flux method show vibrations of water due to KBr discs (Fig. 19). This is evidenced by the broad band around 3350 cm^{-1} as well as a narrower band observed at 1640 cm^{-1}, indicative of antisymmetric and symmetric OH stretching and HOH bending modes [184]. Also, strong Y-O vibrations at 450 cm^{-1} are observed due to the very good crystallization of the $Y_2O_2S:Yb^{3+},Er^{3+}$ products. The content of water is decreased when the annealing time is higher (Fig. 19, left). There are also weak signals at 1100 and 1388 cm^{-1} which are due to a small amount of SO_4^{2-}.

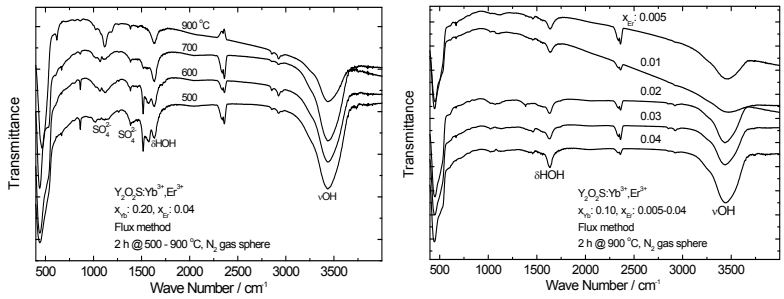

Figure 19. FT-IR spectra of the $Y_2O_2S:Yb^{3+},Er^{3+}$ nanomaterials prepared with the flux method.

4.2.2. $ZrO_2:Yb^{3+},Er^{3+}$

The FT-IR spectra reveal the conventional impurities (NO_3^-, OH^-) [184] in the nanomaterials prepared with the combustion synthesis (Fig. 20) [III,IV,185]. Although the organic compounds (fuels) have mainly decomposed to CO_2, H_2O and NO_x, the materials may contain carbon residues, since some $ZrO_2:Yb^{3+},Er^{3+}$ nanomaterials prepared with this synthesis are brown, whereas the body color of pure ZrO_2 is white. On the other hand, the coloration of the products may be due to color centers present because of the aliovalent substitution of Zr^{IV} with Yb^{3+} or Er^{3+}.

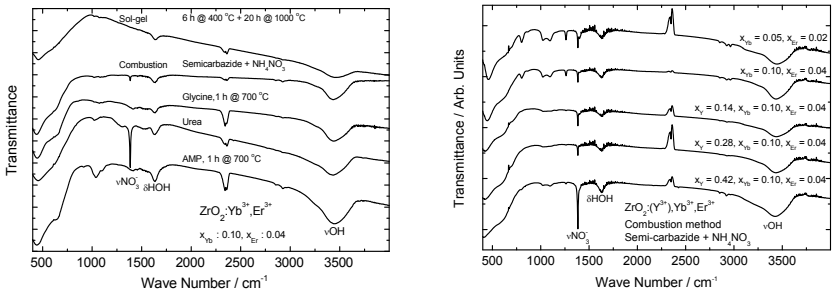

Figure 20. FT-IR spectra of the $ZrO_2:Yb^{3+},Er^{3+}$ nanomaterials prepared with the sol-gel and combustion synthesis [III,IV,185].

4.2.3. $NaYF_4:Yb^{3+},Er^{3+}$

4.2.3.1. Homogeneous materials

The FT-IR spectra of the $NaYF_4:Yb^{3+},Er^{3+}$ prepared with co-precipitation reveal that in the materials with both cubic and hexagonal phases, there are metal-fluoride vibrations of both phases; at 550 and *ca*. 400 cm^{-1} for cubic and hexagonal phase, respectively (Fig. 21) [II,184]. The strong OH stretching and HOH bending vibrations at 3350 and 1550 cm^{-1} [184] respectively, are mainly due to the water absorbed on the surface of the KBr disc during the disc preparation.

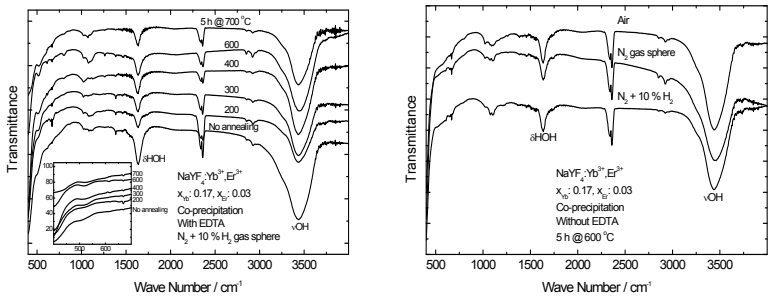

Figure 21. FT-IR spectra of the homogeneous $NaYF_4$:Yb^{3+},Er^{3+} nanomaterials prepared with co-precipitation and annealed at selected temperatures (left) and gas spheres (right) [II].

In the FT-IR spectra of the $NaYF_4$:Yb^{3+},Er^{3+} nanomaterials prepared with the solvothermal synthesis (Fig. 22), there are metal-fluoride vibrations, which reveals that there are both hexagonal and cubic phases: at 400 and *ca*. 530 cm^{-1}, respectively [V,184].

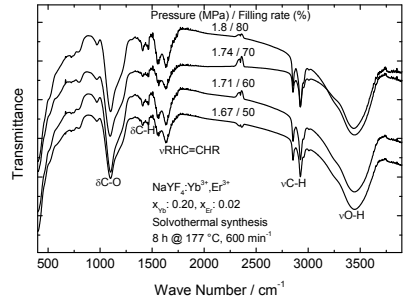

Figure 22. FT-IR spectra of the homogeneous $NaYF_4$:Yb^{3+},Er^{3+} nanomaterials prepared with the solvothermal synthesis at selected reaction pressures [V].

The strong vibration at 1100 cm^{-1} is due to the CO group (Fig. 22) [184]. The vibrations at 1408 and 1462 cm^{-1} are due to the bending vibrations of methylene (CH_2) in the long alkyl chain of the oleic acid and the vibration at 1633 cm^{-1} is due to the RHC=CHR double bond. The 2854 and 2924 cm^{-1} vibrations are assigned to the stretching vibrations of methylene (CH_2) group. The OH stretching (3445 cm^{-1}) vibration is mainly due to the water absorbed on the surface of KBr disc during the preparation. According to these results there is oleic acid in the materials but it is impossible to say, whether the oleic acid chains are unattached or coating the nanoparticle surfaces.

4.2.3.2. Core-shell materials

The FT-IR spectra (Fig. 23) reveal that in the core-shell $Na(Y,Yb)F_4$-$NaErF_4$ material prepared with the co-precipitation method, there were metal-fluoride vibrations of cubic and hexagonal phases; at 550 and *ca*. 400 cm^{-1}, respectively [VI,184]. The other materials show only the metal-fluoride vibrations at 350 cm^{-1} due to the pure hexagonal structure. The strong OH stretching and HOH bending vibrations at 3350 and 1550 cm^{-1}, respectively, are mainly due to the water absorbed on the surface of the KBr disc during the disc preparation.

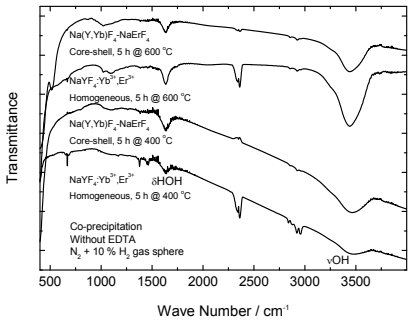

Figure 23. FT-IR spectra of the homogeneous $NaYF_4:Yb^{3+},Er^{3+}$ and core-shell $Na(Y,Yb)F_4$-$NaErF_4$ nanomaterials prepared with co-precipitation [VI].

4.3. Particle size, morphology and elemental distribution

4.3.1. $Y_2O_2S:Yb^{3+},Er^{3+}$

The TEM measurements for $Y_2O_2S:Yb^{3+},Er^{3+}$ nanomaterials prepared with the flux method allow the direct imaging of nanoparticles and provides information on the quality of individual particles, *e.g.* their size and size distribution (Fig. 24) [VII].

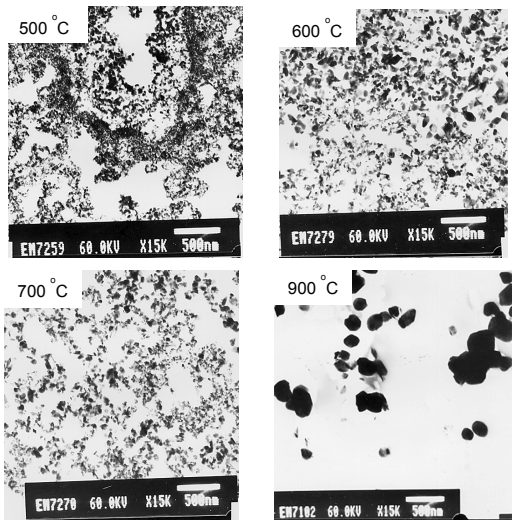

Figure 24. TEM images of selected $Y_2O_2S:Yb^{3+},Er^{3+}$ nanomaterials prepared with the flux method [VII].

The particle size is smaller for materials annealed at lower temperatures. The average particle size determined from TEM is equal to 10 nm for the materials annealed at 500 °C (Fig. 24A) and 20-40 nm for materials annealed at 700 or 600 °C (Figs. 24B and 24C). The particle size is *ca.* 70-110 nm for the materials annealed at 900 °C (Fig. 24D). These sizes agree with the calculations using the Scherrer equations.

4.3.2. $NaYF_4:Yb^{3+},Er^{3+}$

The TEM images of the $NaYF_4:Yb^{3+},Er^{3+}$ nanomaterials prepared with co-precipitation using EDTA as a chelating agent reveal that the particles are quite uniform in size (*ca.* 110 nm), and the shape is spherical-like (Fig. 25) [186]. The particles are strongly aggregated before annealing, but after annealing, they are more separate. This is probably due to the loss of the moisture during the heating. The annealing at low temperature (350 °C) did not increase the particle size.

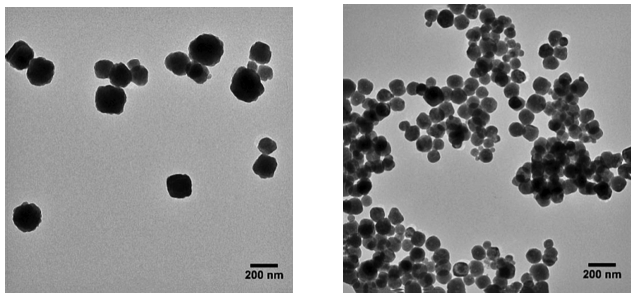

Figure 25. TEM images of the homogeneous $NaYF_4:Yb^{3+},Er^{3+}$ nanomaterials prepared with co-precipitation (not annealed (left) and annealed 5 h @ 350 °C in N_2+10 % H_2 gas sphere (right)) [186].

The TEM images of the $NaYF_4:Yb^{3+},Er^{3+}$ nanomaterials prepared with the solvothermal synthesis (Fig. 26) reveal that there are both small spherical and large cubic particles [V]. The particles are also strongly aggregated. The size of the spherical particles is 10-20 and the cubic particles *ca.* 50 nm. In addition, rods with the length of *ca.* 1 µm are observed. These rods are formed due to the high NaF to R^{3+} ratio (7:1) [68,187] and long reaction time.

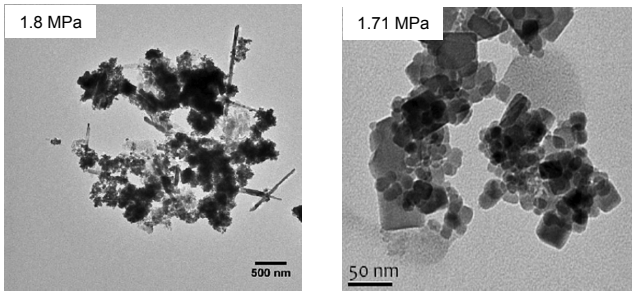

Figure 26. TEM images of the $NaYF_4:Yb^{3+},Er^{3+}$ nanomaterial prepared with the solvothermal synthesis for 8 h @ 177 °C [V].

According to the literature, the NaF to Y^{3+} molar ratio can greatly influence the morphology of the hexagonal β-$NaYF_4$ crystals [68]. The morphology evolution process of the hexagonal-phase $NaYF_4$ along with the molar ratio of NaF to Y^{3+} is interesting. The hexagonal crystal system has four crystal axes, three of which intersecting with each other at a skew angel 60° in a plane surface are assistant axes, and the other axis (c axis) perpendicular to the plane is the principle axis. According to the general principle of crystal growth, the most representative and common shape for hexagonal

compounds is the hexagonal prism. If the crystal growth rate on the directions of the assistant axes is quicker than that on the c axis in the crystal growth process, the crystal takes the hexagonal plate morphology. Otherwise, the crystal is likely to be a long and thin hexagonal prism, and even to be a long needle if the growth rate along the c-axis is much quicker than along the plane surface. As mentioned earlier, the growth rate at different directions of β-$NaYF_4$ has been reported to be profoundly affected by the NaF to Y^{3+} ratio. In the synthetic route, NaF is excessive compared with Y^{3+} and the excessive F is inevitably capped on the crystal surface due to the strong coordination effect between F^- and Y^{3+}. According to the Gibbs-Thompson theory, the relative chemical potential of a crystal is simply proportional to its surface-atom ratio, determined by the average number of dangling bonds per atom over the entire crystal. The capping effect of F^- would decrease the average number of dangling bonds, and further decrease the chemical potential of the crystal, as well as the crystal plane.

A detailed observation on the crystal structure of β-$NaYF_4$ reveals that the Y^{3+} density on different crystal planes varies. The density of Y^{3+} on the $(10\bar{1}0)$ crystal plane is larger than the density of Y^{3+} on the (0001) crystal plane. The capping effect of F^- on the $(10\bar{1}0)$ crystal plane is greater than it on the (0001) plane. As a result, the chemical potential of these crystal planes varies, and the relative growth rate on the different directions changes, finally leading to the different crystal morphologies.

The EDX spectroscopy measurements show a homogeneous distribution for all elements (Na, Y, Yb, Er) in the homogeneous $NaYF_4$:Yb^{3+},Er^{3+} prepared with co-precipitation without EDTA and annealed at 400 °C (Fig. 27, left). The Na(Y,Yb)F_4-$NaErF_4$ core-shell material prepared at 400 °C shows an inhomogeneous distribution of Er due to the lack of diffusion induced mixing of layers at such a low temperature (Fig. 27, middle). The homogeneous elemental distribution of the Na(Y,Yb)F_4-$NaErF_4$ core-shell materials prepared at the higher temperature (600 °C) indicates (at least a partial) mixing of the layers by diffusion of the Yb^{3+} and Er^{3+} ions (Fig. 27, right). According to the SEM images, the particle size in these materials is *ca.* 100 nm. However, the annealing at 600 °C caused particle aggregation.

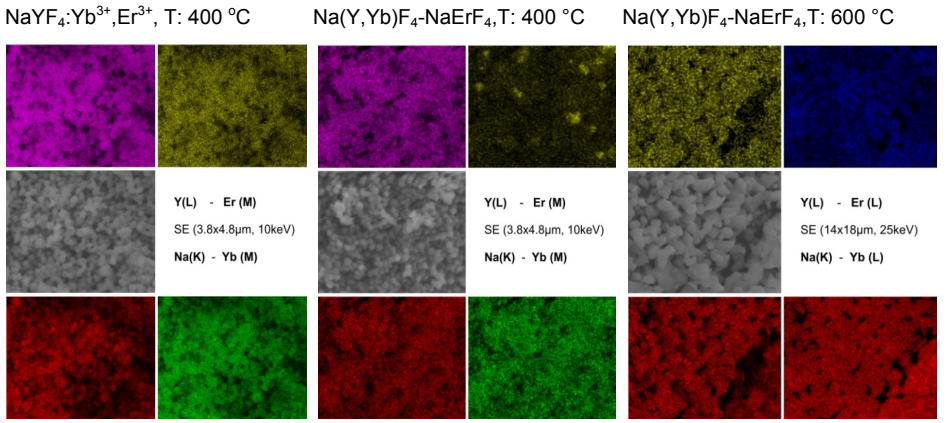

Figure 27. Elemental distribution of the homogeneous $NaYF_4$:Yb^{3+},Er^{3+} and the core-shell Na(Y,Yb)F_4-$NaErF_4$) nanomaterials prepared with co-precipitation (without EDTA).

4.4. Structure and phase purity

4.4.1. $Y_2O_2S:Yb^{3+},Er^{3+}$

The X-ray powder diffraction patterns (Fig. 28) [VII] confirm that the crystal structure of the $Y_2O_2S:Yb^{3+},Er^{3+}$ nanomaterials prepared with the flux method is hexagonal (space group $P\bar{3}m$, No 164, Z: 1) [178] composed of the alternating $(RO)_2^{2+}$ and S^{2-} layers [188].

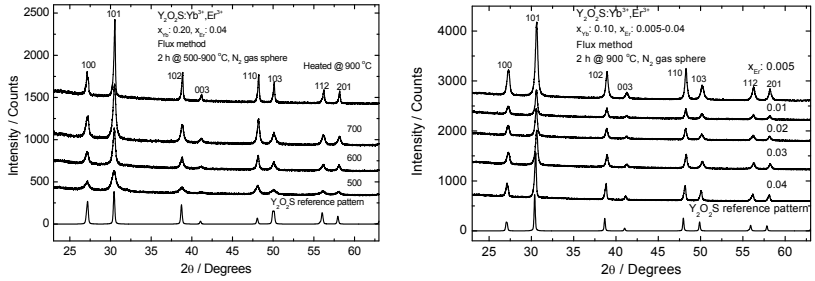

Figure 28. X-ray powder diffraction patterns of the selected $Y_2O_2S:Yb^{3+},Er^{3+}$ nanomaterials prepared with the flux method [III].

The structure is very closely related to the A-type rare earth oxide (A-R_2O_3) structure, the difference being that one third of the oxygen sites is occupied by sulfur. No oxide precursor material was found in the nanomaterials.

The high annealing temperature improved the crystallinity and increased the crystallite size (Fig. 28, left), as can be seen on the narrow and intense reflections. When the annealing temperature was low, the crystallite size was smaller and the crystallinity was poorer (broad and less intense reflections). The different erbium concentrations did not affect the crystallinity or the crystallite size (Fig. 28, right).

4.4.2. $ZrO_2:Yb^{3+},Er^{3+}$

The XPD measurements reveal that the structure of the $ZrO_2:Yb^{3+},Er^{3+}$ nanomaterials is that of the typical cubic yttria stabilized zirconia (YSZ phase, cubic with space group $Fm\bar{3}m$, No 225, Z: 4) [I,IV,VIII,178]. The nanomaterials prepared with the combustion synthesis (Fig. 29, left) are essentially pure, whereas small amounts of the monoclinic ($P2_1/a$, No 14, Z: 4) [178] zirconia phase as an impurity is found in the materials prepared with the sol-gel synthesis.

According to the literature [189,190], the structure of pure ZrO_2 is monoclinic but with small amounts of the trivalent lanthanide doping ions present (*e.g.* Y^{3+}, Eu^{3+}; ionic radii 1.02 and 1.07 Å, respectively [105]) there may exist also tetragonal and cubic phases. In the $ZrO_2:Y^{3+},Eu^{3+}$ system, if the dopant ion level is more than 10 % of the zirconium amount [191], there are no more monoclinic or tetragonal phases present, only the cubic one. If the doping level is greater than 57 %, one obtains the cubic C-type R_2O_3 phase. Because the ionic radii of Yb^{3+} (0.99) and Er^{3+} (1.00 Å) are closer to that of Zr^{IV} (0.84 Å) than those of Y^{3+} and Eu^{3+}, more Yb^{3+} and Er^{3+} than Y^{3+} and Eu^{3+} can probably be doped in the zirconia host. According to the Vegard's rule [192], a good solid solubility can occur when the difference in the ionic radii of the host and dopant ions is less than 15 %. In addition, the charges should be the same as well as the structures of the pure end member compounds be similar. In the $ZrO_2:Yb^{3+},Er^{3+}$ nanomaterial, the sizes of the ions are close to fulfilling the Vegard's rule. Also

the structures of the pure compounds (ZrO_2, C-R_2O_3) are very closely related to the fluorite type structure. Only the charge difference does not favor the solid solubility but this problem is compensated by the charge compensation and the closely related structures. This is valid for the nanomaterials prepared with the combustion synthesis because of the rapid method of synthesis enabling the lanthanide ions to substitute for Zr^{IV}. In contrast, in the nanomaterial prepared with the sol-gel method, the slow reaction rate results in the presence of the monoclinic and/or tetragonal phases due to the establishment of a chemical equilibrium during the reaction. This chemical equilibrium is not achieved during the fast combustion synthesis and phase segregation is thus a minor problem. Whether this segregation is partial (with low and high R^{3+} content ZrO_2:Yb^{3+},Er^{3+} phases) or complete (with ZrO_2 and $(Yb,Er)_2O_3$ phases) is not possible to be deduced from the X-ray powder patterns. The total absence of the reflections for the C-R_2O_3 phase suggests the former while the rather strong reflections - so far unknown - may belong to a lanthanide zirconite phase.

According to the X-ray powder diffraction patterns (Fig. 29, right), the crystal structure of the ZrO_2:Y^{3+},Yb^{3+},Er^{3+} nanomaterials was cubic (space group: $Fm\bar{3}m$, No. 225, Z: 4) [178]. Small amounts of the monoclinic (P21/a, No. 14, Z: 4) [178] and tetragonal (P42/nmc, No. 137, Z: 2) [178] zirconia phases were found as impurities when the nominal Yb^{3+} and Er^{3+} concentrations were 5 and 2 mole-%, respectively.

The mean crystallite sizes were calculated with the Scherrer equation [179]. The crystallite sizes were 5-30 nm for the nanomaterials prepared with the combustion synthesis and *ca.* 50 nm for those prepared with the sol-gel method (Fig. 29). The nanomaterials, prepared with semicarbazide and urea, were well crystallized compared to the nanomaterial prepared with AMP. The larger crystallite size of the nanomaterials prepared with the sol-gel method is due to the slower crystallization and can be taken as a further indication of the possible phase segregation. The crystallite sizes of the ZrO_2:Y^{3+},Yb^{3+},Er^{3+} nanomaterials estimated with the Scherrer equation were *ca.* 30 nm.

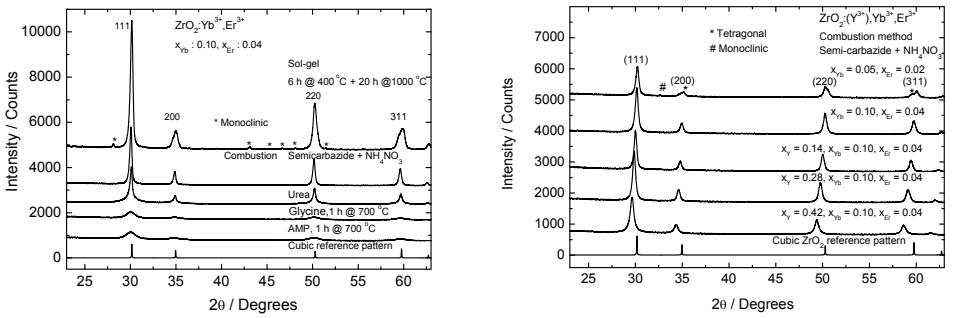

Figure 29. X-ray powder diffraction patterns of the ZrO_2:(Y^{3+},)Yb^{3+},Er^{3+} nanomaterials prepared with the combustion and sol-gel synthesis [I,IV,VIII].

4.4.3. $NaYF_4$:Yb^{3+},Er^{3+}

4.4.3.1. Homogeneous materials

The $NaRF_4$ materials are known to exist as either a cubic or hexagonal form (Fig. 30) [193]. The cubic form has a fluorite (CaF_2) type structure ($Fm\bar{3}m$, No. 225, Z: 2) and it may crystallize in various

stoichiometries $Na_{1-2w}Y_{1+2w}F_{4+4w}$ with w ranging at least from -0.04 to 0.18 [194]. The hexagonal structure has been suggested to be either that of $NaNdF_4$ ($P\bar{6}$, No. 174, Z: 1.5) [195] or related to Gagarinite ($NaCaLaF_6$) having the formula $Na_{1.5}R_{1.5}F_6$ ($P6_3/m$, No. 176, Z: 1) [143]. The (low-temperature) cubic form transforms to the hexagonal one and then to a (high-temperature) cubic upon heating. Both changes are irreversible [196]. The change from the hexagonal to the cubic form has been suggested to involve the gradual loss of NaF finally resulting before decomposition in a $Na_5Y_9F_{32}$ stoichiometry with an unknown crystal structure [143,193].

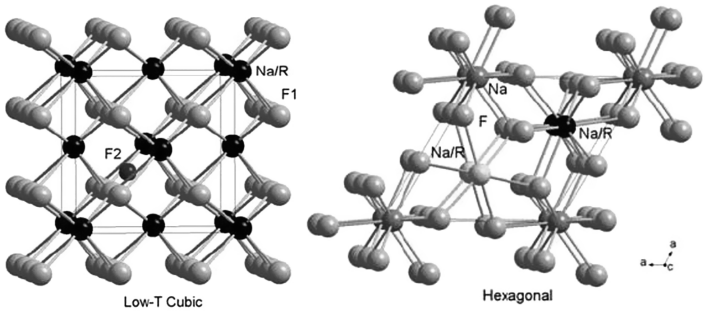

Figure 30. Cubic (left) and hexagonal (right) structure of $NaYF_4$ [IX].

The crystal structure of the $NaYF_4$:Yb^{3+},Er^{3+} materials prepared with co-precipitation with EDTA was cubic below the annealing temperature of 400 °C, both cubic and hexagonal between 400 and 600 °C and cubic again over 700 °C (Fig. 31, left) when annealed in N_2 + 10 % H_2 gas sphere [II]. The structure of the as-prepared $NaYF_4$:Yb^{3+},Er^{3+} material was cubic.

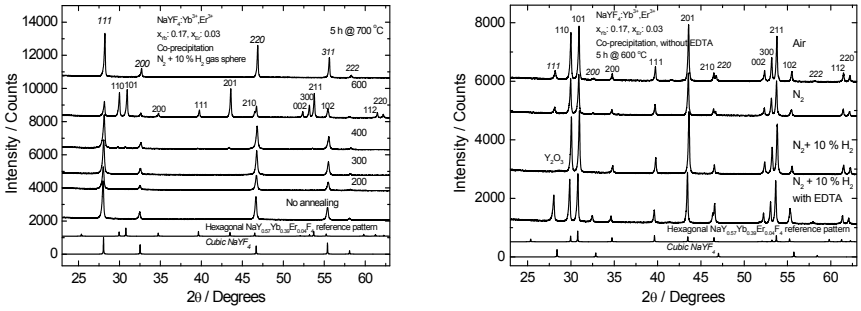

Figure 31. X-ray powder diffraction patterns of the $NaYF_4$:Yb^{3+},Er^{3+} nanomaterials prepared with co-precipitation and annealed at selected temperatures (left) and gas spheres (right) [II].

Annealing in the N_2 + 10 % H_2 gas sphere at 600 °C produced only hexagonal phase whereas a small amount of cubic phase was present in the materials annealed in air or in N_2 when prepared without EDTA (Fig. 31, right) [II]. There was more cubic phase present in the material prepared with EDTA. EDTA thus seems to hinder the formation of the hexagonal phase. There was also a small amount of R_2O_3 impurity in the material prepared without EDTA and annealed for 5 h at 600 °C in N_2 + 10 % H_2 gas sphere.

The calculated crystallite sizes were *ca.* 60-150 nm for the cubic phase and *ca.* 100 nm for the hexagonal phase. The smallest nanocrystallites were obtained with the lowest annealing temperature. EDTA did not have an effect on the crystallite size even though it is a strong chelator and should decrease the crystallite sizes as mentioned previously.

There were both cubic and hexagonal phases in the $NaYF_4$:Yb^{3+},Er^{3+} materials prepared with the solvothermal synthesis (Fig. 32) [V]. Also, a small amount of the NaF impurity was observed. The calculated crystallite sizes were 20-25 and over 140 nm for cubic and hexagonal particles, respectively. The size of the cubic particles did not change with the pressure or reaction time, whereas there was a large variation of the hexagonal particle sizes.

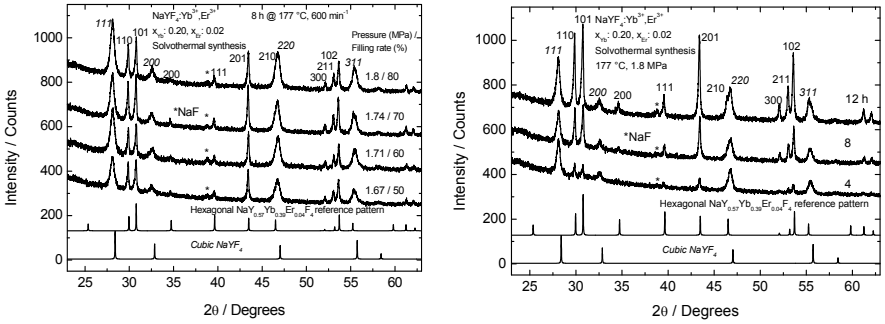

Figure 32. X-ray powder diffraction patterns of the $NaYF_4$:Yb^{3+},Er^{3+} nanomaterials prepared with the solvothermal synthesis with selected reaction pressures (left) and times (right) [V].

4.4.3.2. Core-shell materials

The XPD patterns revealed the presence of the hexagonal ($P\bar{6}$ (#174), Z: 1.5) [178] form of the homogeneous $NaYF_4$:Yb^{3+},Er^{3+} annealed at 400 or 600 °C as well as the core-shell $Na(Y,Yb)F_4$-$NaErF_4$ nanomaterial annealed at 400 °C (Fig. 33) [VI]. The materials were prepared with co-precipitation. The core-shell $Na(Y,Yb)F_4$-$NaErF_4$ nanomaterial annealed at 600 °C was a mixture of both the (high temperature) cubic ($Fm\bar{3}m$ (#225), Z: 2) [178] and hexagonal forms. There was also a very small amount of the C-R_2O_3 impurity in the homogeneous $NaYF_4$:Yb^{3+},Er^{3+} nanomaterial annealed at 600 °C.

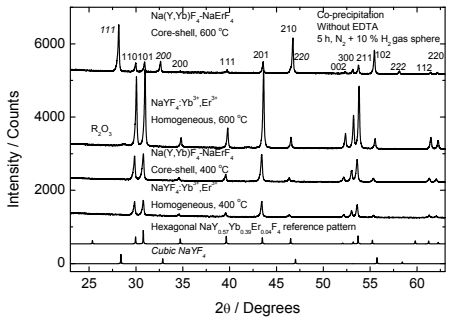

Figure 33. X-ray powder diffraction patterns of the $NaRF_4$-$NaR'F_4$ nanomaterials prepared with co-precipitation [VI].

In the case of the $Na(Y,Yb)F_4$-$NaErF_4$ materials (cubic/hexagonal ratio 6), it can be assumed that the structure of the core is mainly cubic and the shell hexagonal [VI]. In other words, the shell layer may prevent the phase transition from cubic to hexagonal of the core during the annealing.

The calculated crystallite sizes were approximately 80 nm for the materials annealed at 400 and *ca*. 100 and 150 nm for the cubic and hexagonal phases, respectively for the materials annealed at 600 °C [VI]. The crystallite sizes of the core-shell materials were nearly equal to those for the homogeneous $Na(Y,Yb,Er)F_4$. However, from the present diffraction data, it is difficult to judge whether core-shell structures have been formed or to what extent the core and shell contents have been mixed during the heating.

4.5. Environment of Yb and Er

4.5.1. ZrO_2:Yb^{3+},Er^{3+}

The XANES results of the ZrO_2:Yb^{3+},Er^{3+} up-conversion luminescence materials show only the trivalent ytterbium and erbium dopants (Fig. 34) [VIII,197]. When the dopants enter a tetravalent site, there has to be charge compensation. Most probably, oxygen vacancies are created for this purpose according to the following scheme: $2\ Zr_{Zr}^{x} \rightarrow 2\ R'_{Zr} + V_O^{\bullet\bullet}$. In this Kröger–Vink -notation, • denotes a positive and ' a negative charge relative to the environment of the lattice defect - either an oxygen vacancy or an aliovalent R^{3+} ion substituting Zr^{IV}, respectively. Neutral charge is marked as ×.

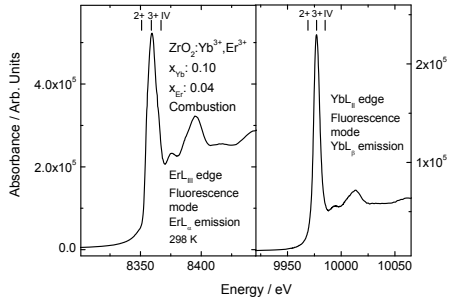

Figure 34. The room temperature XANES spectra of the Er L_{III} (left) and Yb L_{II} (right) edges in the ZrO_2:Yb^{3+},Er^{3+} nanomaterial prepared with the combustion method [VIII].

The distance distributions calculated from EXAFS (Fig. 35) correspond well to those calculated from the structural data [198] for the cubic rare earth stabilized ZrO_2. The similarity of the Zr-Zr, Yb-Zr/Er/Yb and Er-Zr/Yb/Er distances (3.63 Å for each) confirms that the Er^{3+} and Yb^{3+} ions occupy the Zr^{IV} sites in the structure. The R-O and R-M distributions are rather broad partly due to the high measuring temperature and partly to the multisite nature of the R positions. This means slightly different spatial positions of the oxygen vacancies created by the charge compensation inducing several slightly different R'_{Zr} sites [199]. The observed Yb-O (2.30) and Er-O (2.26 Å) distances are too short when compared with the calculated Zr-O distance (2.23 Å) when taking into account the ionic radii (Zr: 0.84, Yb: 0.985, and Er: 1.004; CN: 8 [199]). This indicates the rigidity of the structure but also the presence of oxygen vacancies around Er^{3+} and Yb^{3+}. The oxygen vacancies resulting from the charge compensation are expected to agglomerate with R'_{Zr} due to the electrostatic

reasons. This would effectively reduce the coordination number 8 around Zr to 7 (or even 6) around R^{3+}. This decrease in the coordination number by one unit corresponds to *ca.* 0.06 Å decrease in the R-O distances [199]. The R-O distances calculated from the ionic radii should be 2.375 and 2.394 Å for Yb^{3+} and Er^{3+}, respectively. The analysis of the EXAFS data shows, however, that the R-O distances obtained do not correspond to a coordination number lower than 7 for the R^{3+} ions. It may be even higher if the rigidity of the lattice is taken into account.

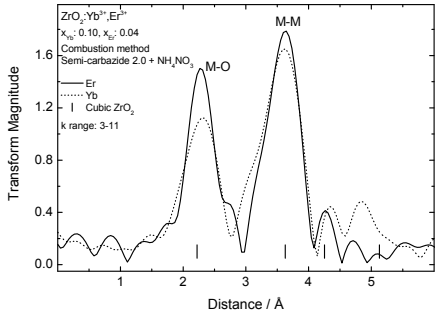

Figure 35. Distance distributions calculated from the Er L_{III} and Yb L_{II} EXAFS spectra the ZrO_2:Yb^{3+},Er^{3+} nanomaterials prepared with the combustion method [VIII].

According to the ionic radii, the Yb-O distance should be shorter than Er-O, but the opposite is observed. This is unexpected, since the higher charge density of Yb^{3+} should attract more the oxide ions. The reason for this could be that there are more oxygen vacancies around Er^{3+} than Yb^{3+}. On the other hand, these materials produced persistent up-conversion luminescence. This seems to require the (at least virtual) change of the oxidation state of one of the species involved. In the Yb^{3+},Er^{3+} system, the only change possible at ambient conditions, is the formation of the divalent Yb^{2+} (or Yb^{3+}-e^-) species which both demand more space than the simple Yb^{3+} ion.

4.5.2. $NaYF_4$:Yb^{3+},Er^{3+}

The XANES measurements show that there are present only trivalent erbium and ytterbium in the $NaRF_4$-$NaR'F_4$ (R: Y, Yb, Er) nanomaterials prepared with co-precipitation (Fig. 36).

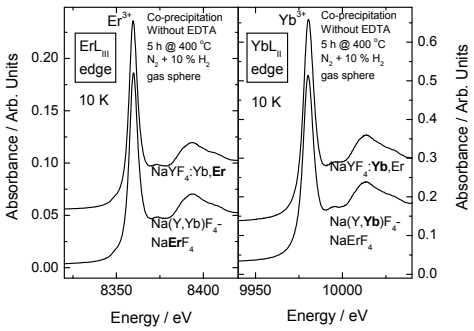

Figure 36. XANES spectra of the homogeneous $NaYF_4$:Yb^{3+},Er^{3+} and core-shell $Na(Y,Yb)F_4$-$NaErF_4$ nanomaterials prepared with co-precipitation [200].

The materials studied were prepared at 400 °C in a N_2 + 12 % H_2 atmosphere. The reducing conditions may affect the valences of Er and Yb. Especially, the Yb^{3+} ion may be reduced to Yb^{2+}. However, the XANES data indicated only the trivalent form for both erbium and ytterbium in both materials. This was suggested by the single white lines peaking on the absorption edges. The divalent forms would have been observed as white lines *ca.* 8 eV below the trivalent ones [200], but not a trace of such signals was detected. Trivalency was anticipated, since the Yb and Er dopants are expected to replace the Y^{3+} ion in the $NaYF_4$ host as well as the fact that both Er and Yb were trivalent in the starting materials.

The EXAFS measurements show good quality fine structure enabling distance distribution calculations (Fig. 37).

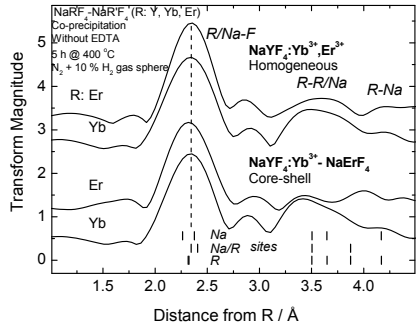

Figure 37. EXAFS spectra and calculated bond distances of the homogeneous $NaYF_4$:Yb^{3+},Er^{3+} and core-shell Na(Y,Yb)F_4-$NaErF_4$ nanomaterials prepared with co-precipitation [200].

Both the homogeneous and core-shell nanomaterials have very similar spectra for Er and Yb. The distance distributions obtained from the EXAFS data using the EXAFSPAK program [180] indicate that the surroundings of both Er^{3+} and Yb^{3+} are as calculated from structural data for the homogeneous hexagonal $NaRF_4$ structure [201]. In the core-shell material, the shell Er-F distance (*ca.* 2.32 Å) is shorter than the core Yb-F or the Er-F and Yb-F (*ca.* 2.35 for all three) for the homogeneous material. Assuming a complete solid solubility, the average radius of the R^{3+} ions [105] for the homogeneous material and the core should be 1.07 whereas 1.06 Å is expected for the shell. The results may thus indicate that a core-shell structure has been formed. However, the differences of the R-F distances between homogeneous and core-shell nanomaterials are very small.

4.6. Absorption spectroscopy

The absorption spectra of the ZrO_2:Yb^{3+},Er^{3+} nanomaterials prepared with the sol-gel synthesis showed the $^2F_{7/2} \rightarrow {}^2F_{5/2}$ transition of Yb^{3+} in the wave number region 10 000 - 11 500 cm^{-1} (Fig. 38) [III]. The absorption bands were broad both at the room temperature and 10 K. This is due to the lanthanide dopants possessing multisite positions in the zirconia matrix. The multisite position may thus improve the absorption efficiency. The strongest absorption band centered at 10 310 cm^{-1} fits well to the laser excitation used. Other absorption bands in the spectra are probably due to the vibrational fine structure. A comparison between the absorption spectra of the ZrO_2:Yb^{3+},Er^{3+}

nanomaterials and the whole-blood reveals that there is no blood absorption in the excitation wavelength region of the phosphor.

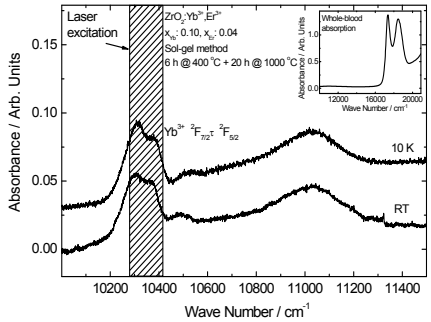

Figure 38. Absorption spectra of the $ZrO_2:Yb^{3+},Er^{3+}$ at RT and 10 K and the spectrum of the whole blood [III].

4.7. Excitation spectroscopy

The luminescence excitation spectra were collected to gain information on the band gap energy of the $ZrO_2:Yb^{3+},Er^{3+}$ nanomaterials. At 10 and 300 K, the E_g was 5.3 eV (234 nm) and 5.1 (243), respectively (Fig. 39) [VIII]. Such a decrease is common for band gap energies [202] and the observed values are in good agreement with data published earlier for non-doped ZrO_2 [*e.g.* 203].

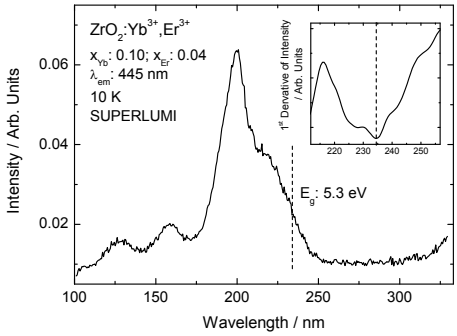

Figure 39. Synchrotron radiation luminescence excitation spectra of $ZrO_2:Yb^{3+},Er^{3+}$ nanomaterials at 10 K [VIII].

4.8. Up-conversion luminescence

4.8.1. $Y_2O_2S:Yb^{3+},Er^{3+}$

Strong red and moderate green up-conversion luminescence was obtained from the $Y_2O_2S:Yb^{3+},Er^{3+}$ nanomaterials prepared with the flux method (Fig. 40, left) [VII]. An increase in the annealing temperature brought up a rapid growth of the crystallites of the $Y_2O_2S:Yb^{3+},Er^{3+}$ nanomaterials. Along with the increased crystallite size, the intensity of the green up-conversion luminescence due to the $(^2H_{11/2},^4S_{3/2})\rightarrow{}^4I_{15/2}$ transitions increased more than that of the red ($^4F_{9/2}\rightarrow{}^4I_{15/2}$) one, *i.e.* the I_{red}/I_{green} intensity ratio (*ca.* 7 at 600/700 °C and 4 at 900 °C) decreases with increasing particle size.

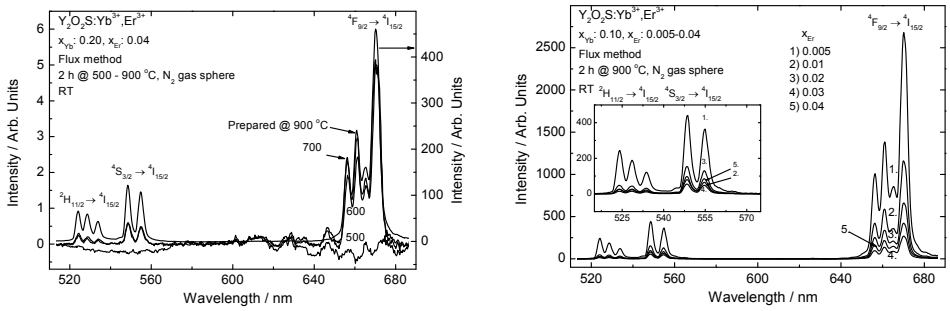

Figure 40. Up-conversion luminescence spectra of the $Y_2O_2S:Yb^{3+},Er^{3+}$ nanomaterials prepared with the flux method with selected annealing temperatures (left) and Er^{3+} concentrations (right) [VII].

The Er^{3+} ions tend to form clusters when the particle size decreases [VII,109]. This improves the probability of the cross-relaxation (CR) processes of Er^{3+} ions. The first process includes the $^2H_{11/2} \rightarrow {}^4I_{13/2}$ relaxation and the $^4I_{15/2} \rightarrow {}^4I_{9/2}$ excitation (energy difference: 12 500 cm^{-1}). In the second possible cross-relaxation process, there are coupled the $^2H_{11/2} \rightarrow {}^4I_{9/2}$ relaxation and the $^4I_{15/2} \rightarrow {}^4I_{13/2}$ excitation (energy difference: 6700 cm^{-1}). These two processes decrease the intensity of both the red and green luminescence. In the third possible cross-relaxation process, there are the $^4F_{7/2} \rightarrow {}^4F_{9/2}$ relaxation and the $^4I_{15/2} \rightarrow {}^4I_{11/2}$ excitation (energy difference: 5000 cm^{-1}). This process favors the red luminescence.

The weak total up-conversion luminescence from materials prepared at low temperatures is partly due to the increase in the particle surface area, which increases the amount of the surface defects and the adsorption of other defect impurities (*e.g.* CO_2, H_2O) [VII]. Both cause important losses in the luminescence. There is no up-conversion luminescence from the nanomaterials when the heating temperature is 500 °C (Fig. 40, left).

The comparison of the up-conversion luminescence spectra of materials with different erbium content showed that the intensity of the green luminescence decreases, although to lower extent compared to the red one, as the erbium concentration increases (Figs. 40, right; 41). At low Er^{3+} concentrations, the Er^{3+} ions are randomly distributed in the host lattice and this prevents the interionic CR processes. Therefore the green luminescence is stronger when compared to the red one. When the erbium mole fraction is higher than 0.005 the concentration quenching occurs and thus weakens the total up-conversion luminescence intensity.

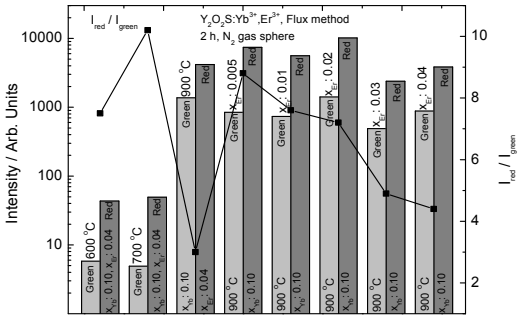

Figure 41. Red-to-green intensity ratios of the $Y_2O_2S:Yb^{3+},Er^{3+}$ nanomaterials prepared with the flux method with selected annealing temperatures and Er^{3+} concentrations.

4.8.2. $ZrO_2:Yb^{3+},Er^{3+}$

In the ZrO_2 matrix, the luminescence transitions are rather broad and without evident crystal field fine structure. This observation is in agreement with the multi-site positions occupied by the trivalent Yb^{3+} and Er^{3+} ions. This is due to the lack of any trivalent ion site in the ZrO_2 structure and the creation of oxide vacancies (Kröger-Vink notation: $V_O^{\bullet\bullet}$) as a result of the Yb^{3+} and Er^{3+} ions occupying the tetravalent Zr^{IV} site ($Yb_{Zr}^{'}$ or $Er_{Zr}^{'}$) in the cubic fluorite type structure (Fig. 42).

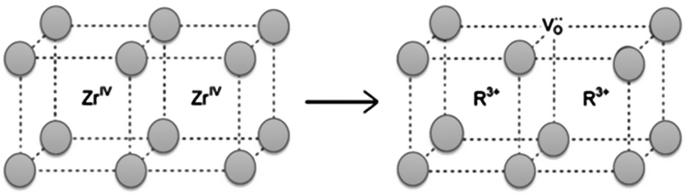

Figure 42. Structure of the environment of zirconium in ZrO_2 with and without R^{3+} substitution [204].

In the $ZrO_2:Y^{3+},Eu^{3+}$ system, at least three different oxide vacancy positions have been found around the R^{3+} ion [191,199]. A similar behavior is present in the $ZrO_2:Yb^{3+},Er^{3+}$ nanomaterial due to the similar ionic radii of the Y^{3+} and Yb^{3+}. In addition, because of the smaller ionic radius of Zr^{IV} compared to those of Yb^{3+} and Er^{3+}, further structural distortions around the R^{3+} ions are induced due to the different charge compensation schemes in the outer coordination spheres. These distortions cause the broadening of the individual lines in the luminescence spectra.

Owing to the general tendency of defects to form aggregates and because of the electrostatic attraction between the species, $Yb_{Zr}^{'}$-$V_O^{\bullet\bullet}$-$Er_{Zr}^{'}$ pairs are formed. These pairs can enhance the absorption efficiency and the energy transfer between Yb^{3+} and Er^{3+} ions though energy migration between Yb^{3+} ions may result, too. The energy migration may cause the excitation energy to reach an impurity and be lost before reaching an Er^{3+} ion.

The most intense up-conversion luminescence was observed from the ZrO_2:Yb^{3+},Er^{3+} nanomaterial prepared with the combustion synthesis with semicarbazide as the organic fuel (Fig. 43).

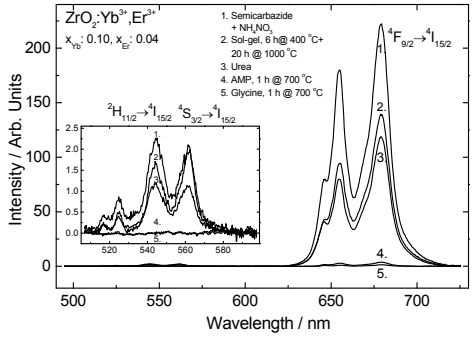

Figure 43. Up-conversion luminescence spectra of the ZrO_2:Yb^{3+},Er^{3+} nanomaterials prepared with the combustion and sol-gel synthesis [204].

This is due to the structurally pure cubic nanomaterial. The luminescence intensity was very weak from the nanomaterials prepared with the AMP or glycine as the fuel. This is due to the small crystallite size (*ca.* 5 nm) and the large surface area of the particles. Large surface area increases the amount of surface defects and the adsorption of impurities (*e.g.* CO_2, H_2O, NO_3^-) that decrease the luminescence intensity. Although there were considerable amounts of nitrate residues in the nanomaterial prepared with the urea as the fuel, there were observed rather intense up-conversion luminescence. This is due to the good crystallinity and large crystallite size of these nanomaterials.

The crystallite sizes of the ZrO_2:Yb^{3+},Er^{3+} nanomaterials prepared with the sol-gel synthesis were larger when compared to the nanomaterials prepared with the combustion synthesis. Despite this, the luminescence intensity was lower than that of the nanomaterials prepared with the combustion synthesis with semicarbazide as the fuel. The weak luminescence intensity is probably due to the fact that the sol-gel nanomaterial was a mixture of the cubic and monoclinic forms. This phase separation evidently weakens the luminescence intensity since the optimum concentrations for the R^{3+} ions are lost. Because of the ZrO_2 and R_2O_3 being in separate phases, concentration quenching might occur due to the too high Yb^{3+} and Er^{3+} concentrations in the R_2O_3 phase. Alternatively, if separate low and high R^{3+} content ZrO_2 phases are formed, the R^{3+} concentrations in the latter phase are too high and in the former too low. For this reason, concentration quenching (Er^{3+}) and energy migration (Yb^{3+}) to non-luminescent sites can occur just in a manner similar to R_2O_3. The different surrounding microdomains of the Yb^{3+} and Er^{3+} ions of the nanomaterials prepared with different methods might also affect the absorption efficiency and luminescence intensity.

The most intense red up-conversion luminescence (Fig. 44) was obtained when x_{Yb} : 0.10 and x_{Er}: 0.04 without Y^{3+} (curve 2) or with the lowest Y^{3+} concentration (x_Y: 0.14, curve 3). The weakness of the green luminescence is due to several cross-relaxation (CR) processes [IV].

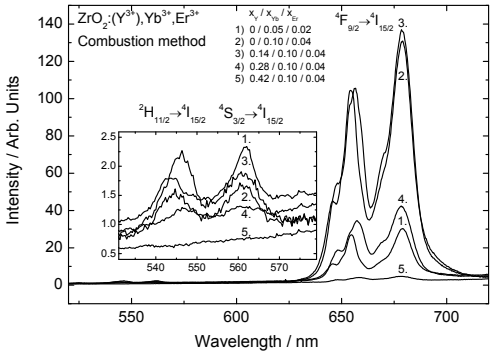

Figure 44. Up-conversion luminescence spectra of the ZrO_2:(Y^{3+},)Yb^{3+},Er^{3+} nanomaterials prepared with the combustion and sol-gel synthesis [IV].

The more there was yttrium in the materials the weaker was both the red and green up-conversion luminescence. This is due to the formation of Yb^{3+}-$V_O^{\bullet\bullet}$-Y^{3+} entities instead of the Yb^{3+}-$V_O^{\bullet\bullet}$-Er^{3+} (and Yb^{3+}-$V_O^{\bullet\bullet}$-Yb^{3+}) ones. The Yb^{3+}-$V_O^{\bullet\bullet}$-Y^{3+} entities cut the energy migration in the Yb^{3+} sublattice, increase the distance between ytterbium and erbium and thus prevent short range Yb^{3+}-Er^{3+} energy transfer. The energy transfer processes needed for the up-conversion are made more difficult and finally the up-conversion luminescence is weakened. When the nominal concentration of Er^{3+} was 2 % (curve 1), the green luminescence was slightly stronger when compared to higher (four) Er^{3+} concentration (curve 2). The cross-relaxation processes are favored by the higher erbium concentration because Er^{3+} ions can form Er^{3+}-$V_O^{\bullet\bullet}$-Er^{3+} pairs with the oxygen vacancies. These pairs increase, in addition to the intra-ion cross-relaxation processes, the inter-ion processes and thus the concentration quenching is more effective.

When the nominal Yb^{3+} and Er^{3+} concentrations were 5 and 2 %, respectively (Fig. 44, curve 2), the total up-conversion luminescence intensity was lower when compared to that of the ZrO_2 nanomaterial with x_{Yb}: 0.10 and x_{Er}: 0.04. In the first place, this is due to the low Yb^{3+} concentration (weak absorption of the NIR photons), but probably the low structural purity of the former material being a mixture of both the cubic and monoclinic phases may have an effect, too.

The ZrO_2:Yb^{3+},Er^{3+} nanomaterials exhibit a very high I_{red} / I_{green} ratio (Fig. 45) compared to the other host materials (*e.g.* $NaYF_4$) [I]. This is due to the very low intensity of the green luminescence. In the ZrO_2 host, there are three main reasons for the weak green luminescence: the multiphonon relaxation, the cross-relaxation and trapping of excitation energy by defects.

The prerequisites for efficient multiphonon relaxation are an energy level below the luminescent level and/or high-energy phonon. The energy difference between the $^4S_{3/2}$ (and $^2H_{11/2}$) levels yielding the green luminescence and the next lower level ($^4I_{9/2}$) is *ca.* 3000 (and *ca.* 3700) cm^{-1}. The Zr-O phonon energy is 470 cm^{-1} [18] and the Er-O energy is approximately the same. In pure materials, the multiphonon relaxation process is not probable because too many (six or seven) lattice phonons are needed. However, when the crystallite size is smaller, there exist usually more impurities (*e.g.* NO_3^-, OH^-) and the large surface area to facilitate the quenching of luminescence. The probability of

the multiphonon relaxation is then increased because the impurities have higher phonon energies (up to 1500 and 3500 cm^{-1}) and thus less phonons (one or two) are needed for quenching. Finally, the multiphonon relaxation of the green luminescence enhances the intensity of the red luminescence by populating the $^4F_{9/2}$ level.

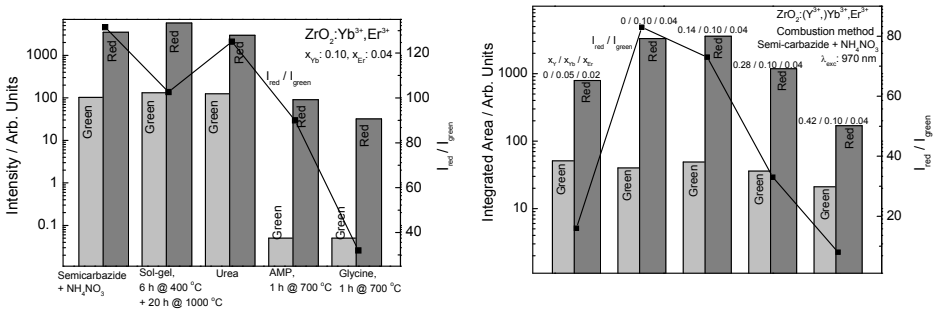

Figure 45. Red-to-green intensity ratios of the ZrO_2:(Y^{3+},)Yb^{3+},Er^{3+} nanomaterials prepared with the combustion and sol-gel synthesis [I].

The energy difference between the $^4F_{9/2}$ level yielding the red luminescent and the next lower level $^4I_{9/2}$ is also *ca.* 3000 cm^{-1}. This means that the probability for the multiphonon relaxation of the red luminescence should be comparable to that of the green luminescence. However, the red emission is quite strong and thus the multiphonon relaxation is not working efficiently in this case. It should also be noted that both the green and red luminescence of the ZrO_2:Yb^{3+},Er^{3+} nanomaterials are weak when compared to other host lattices (*e.g.* $NaYF_4$, Y_2O_2S) [I]. The multiphonon relaxation processes can thus explain the weakness of the total luminescence but not the individual green luminescence.

The second process that may affect the luminescence intensities is cross-relaxation [I]. The cross-relaxation processes of Er^{3+} are naturally favored by the rather high erbium concentration in the ZrO_2:Yb^{3+},Er^{3+} nanomaterials (nominally four mole-%) because then the erbium ions can locate near each other. As a special feature in the zirconia host, the Er^{3+} ions can form pairs with the aid of the oxide vacancy, *i.e.* Er^{3+}-$V_O^{\bullet\bullet}$-Er^{3+}. Thus the inter-ion cross-relaxation processes can occur easily between the Er^{3+} ions and decrease the intensity of the green luminescence.

The very weak green luminescence can thus be explained with both the multiphonon and the cross-relaxation processes [I]. However, in order to judge the relative probabilities of these processes, it should be noted that the cross-relaxation processes do not enhance the intensity of the red luminescence. In fact, if the cross-relaxation processes were the only processes that quench the green luminescence, there should not appear any red luminescence, because the cross-relaxation processes do not populate the $^4F_{9/2}$ level. Because efficient red luminescence is observed, the multiphonon relaxation process must be the dominating relaxation process.

The energy trapping caused by the oxygen vacancies is also a competing process with the multiphonon and cross-relaxation processes [I]. The total luminescence intensity can be quenched due to the absorption of the excitation energy. However, it is evident that the persistent luminescence following the energy released from the traps is originating from the $^4F_{9/2}$ level, *i.e.* is red.

The power curves (luminescence intensity versus excitation power) of the green and red Er^{3+} luminescence for the materials with x_Y: 0.14, x_{Yb}: 0.10 and x_{Er}: 0.04 (Fig. 46) were measured to verify the up-conversion luminescence process as described above [205].

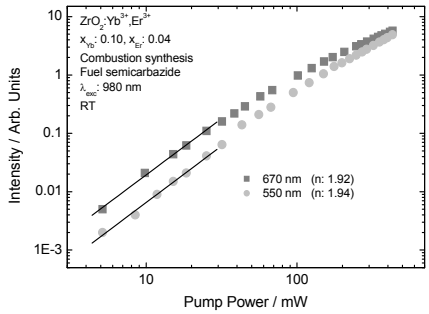

Figure 46. Up-conversion power curves of the ZrO_2:Yb^{3+},Er^{3+} nanomaterials prepared with the combustion synthesis [205].

Experimental results were fitted to the well-known equation $I_{em} \propto I_{exc}^n$ (Eq. 1), where I_{em} and I_{exc} stand for the up-conversion emitting and exciting signal, respectively, and n is an integer denoting the number of photons required to excite the corresponding emitting level. In the low-power region, the slopes in the dilogarithmic plot are close to 2, but in a higher-power region the slopes decrease as the power increases. Since for a two-photon up-conversion process a value of 2 for n is expected, it is assumed that the difference is a consequence of the cross-relaxation processes taking place.

4.8.3. $NaYF_4$:Yb^{3+},Er^{3+}

4.8.3.1. Homogeneous materials

The strongest up-conversion luminescence of the $NaYF_4$:Yb^{3+},Er^{3+} materials prepared with co-precipitation with EDTA was obtained when the annealing temperature was 700 °C due to the large crystallite size (*ca.* 150 nm) (Fig. 47, left) [II]. The smaller is the crystallite size the weaker is the total up-conversion luminescence due to the large surface area of the small particles. Large surface area increases the amount of the surface defects and the adsorption of the atmospheric impurities (*e.g.* CO_2, H_2O, NO_3^-) that decrease the total luminescence intensity. The total luminescence intensity of the as-prepared material and the material annealed at 200 °C were almost the same. This indicates that the crystallite sizes of the materials are the same, so the used annealing temperature is too low to improve the up-conversion luminescence intensity.

The up-conversion luminescence spectra showed also that the bands of the luminescence spectra have different shapes when annealed at different temperatures (Fig. 47, left) [II]. This is due to the different structures of the materials: the cubic and hexagonal phases have different microdomains around the luminescence centers. Also the low and high temperature cubic materials have differently shaped luminescence bands; this confirms that the $NaYF_4$ has two different cubic structures.

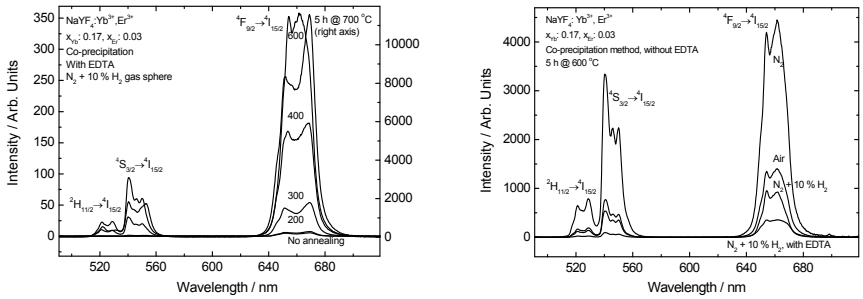

Figure 47. Up-conversion luminescence spectra of the $NaYF_4:Yb^{3+},Er^{3+}$ nanomaterials annealed at selected temperatures (prepared with EDTA, left) and gas spheres (prepared without EDTA, right) [IV].

When prepared without EDTA at 600 °C, the total up-conversion luminescence of the $NaYF_4:Yb^{3+},Er^{3+}$ materials was stronger than prepared with EDTA (Fig. 47, right) due to the efficiently luminescent hexagonal phase of the former material [II]. When prepared with EDTA there was cubic phase in the material that weakens the luminescence. Although the structure of the material annealed at 700 °C is cubic, the strong luminescence of the material is due to the large crystallite size which increases the up-conversion luminescence intensity. The most intense total luminescence of the materials prepared without EDTA and annealed at 600 °C was obtained with the inert N_2 gas sphere (Fig. 47, right) [IV]. This is due to the lack of the (surface) impurities caused by oxygen in air or hydrogen in the N_2 + 10 % H_2 gas sphere.

When prepared without EDTA and annealed at 600 °C in N_2 + 10 % H_2 the intensity of the green luminescence was higher compared to the materials prepared with EDTA (Fig. 48) [II]. This is due to EDTA that increases the probability of the cross-relaxation processes of Er^{3+}. The cross-relaxation processes decrease the intensity of green luminescence and increase the red one. Also the high I_{red}/I_{green} ratio at low annealing temperatures is due to the surface impurities of the small nanoparticles. The impurities weaken especially the green luminescence due to the cross-relaxation mechanisms.

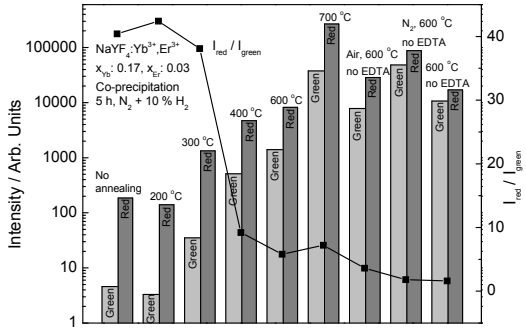

Figure 48. Red-to-green up-conversion luminescence intensity ratios of the homogeneous $NaYF_4:Yb^{3+},Er^{3+}$ materials prepared with co-precipitation [II].

The cross-relaxation processes of Er^{3+} are naturally favored by the rather high erbium concentration in the $NaYF_4:Yb^{3+},Er^{3+}$ nanomaterials (three mole-%) because the erbium ions can locate near each other. Also the strong red luminescence can be explained with the above mentioned cross-relaxation process.

The up-conversion luminescence of the $NaYF_4:Yb^{3+},Er^{3+}$ materials prepared with the solvothermal synthesis was stronger with the increasing reaction time and pressure as well as with the increasing proportion of the hexagonal crystal form (Fig. 49, left) [V]. The most intense luminescence was obtained with the material annealed for 8 h at 177 °C (1.8 MPa, filling rate 80 %). The large crystallite size increased the luminescence intensity due to the smaller surface area of the particles. Large surface absorbs more (atmospheric) impurities (like H_2O, CO_2) which decrease the luminescence intensity.

In the up-conversion luminescence spectra of the materials with selected reaction times (Fig. 49, right) the most intense luminescence is obtained with the material treated for 12 h due to the largest amount of the highly luminescent hexagonal form [V]. The shape of the red luminescence band of the material treated for 4 h is different than the two other luminescence bands. This is due to the different crystal field around the luminescence Er^{3+} center.

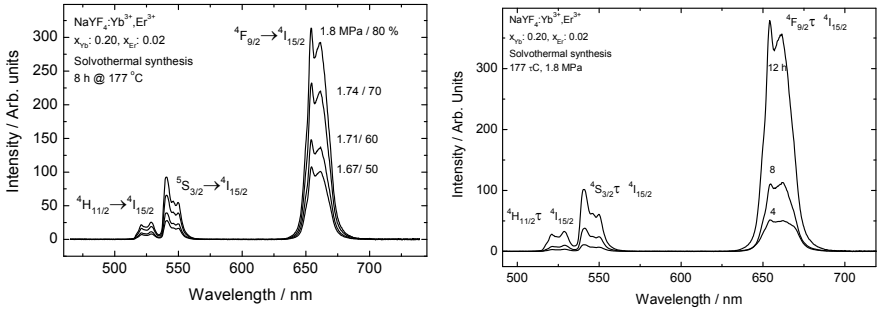

Figure 49. Up-conversion luminescence spectra of the $NaYF_4:Yb^{3+},Er^{3+}$ nanomaterials prepared with the solvothermal synthesis with selected pressures (left) and times (right) [V].

The red-to-green ratio was high with low reaction pressures (Fig. 50) [V]. This is due to the large amount of the cubic particles with small crystallite size. The small cubic particles absorb more the (atmospheric) impurities (like H_2O, CO_2) which weaken especially the green luminescence due to the multiphonon de-excitation mechanism.

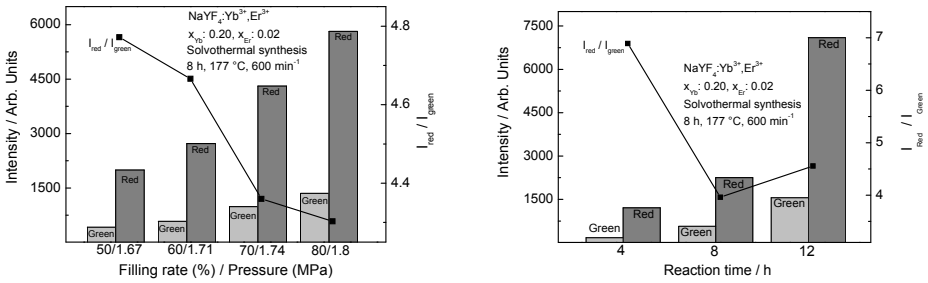

Figure 50. Red-to-green up-conversion luminescence intensity ratios of the $NaYF_4:Yb^{3+},Er^{3+}$ nanomaterial prepared with the solvothermal synthesis with selected reaction pressures (left) and times (right) [V].

4.8.3.2. Core-shell materials

The up-conversion luminescence spectra of the $NaRF_4$-$NaR'F_4$ (R: Y, Yb, Er) prepared with co-precipitation show strong red (centered at 660) and moderate green (525 and 545 nm) up-conversion luminescence due to the ($^4F_{9/2}\rightarrow{}^4I_{15/2}$) and ($^2H_{11/2}$, $^4S_{3/2}\rightarrow{}^4I_{15/2}$) transitions, respectively (Fig. 51) [VI]. When annealed at 600 °C, the partially cubic core-shell $Na(Y,Yb)F_4$-$NaErF_4$ nanomaterial produces stronger luminescence than the corresponding homogeneous $NaYF_4:Yb^{3+},Er^{3+}$ with the hexagonal structure. Although the hexagonal $NaYF_4$ phase is one of the most efficient lattices for up-conversion luminescence known to date [22,23], the up-conversion luminescence intensity of the hexagonal, homogeneous $Na(Y,Yb,Er)F_4$ material is rather weak compared to the partially cubic core-shell materials. This is due to the aggregation by diffusion at high annealing temperatures, probably enhanced by the interface between the core and the shell. In the homogeneous material, there is no concentration gradient for the optically active ions and they cannot move towards more favorable places for the up-conversion luminescence.

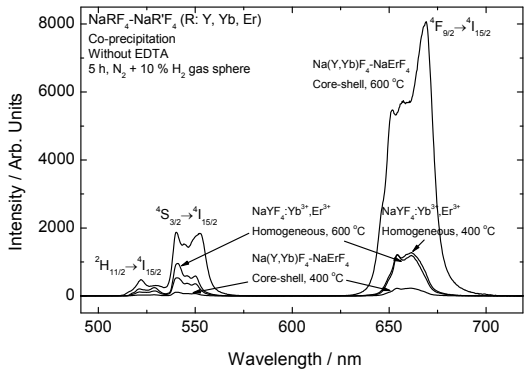

Figure 51. Up-conversion luminescence spectra of the homogeneous $NaYF_4:Yb^{3+},Er^{3+}$ and core-shell $Na(Y,Yb)F_4$-$NaErF_4$ nanomaterials prepared with co-precipitation [VI].

It could also be thought that it is easier to excite the ytterbium ion when it is in the shell layer and close to the erbium activator ions. However, according to these results, the up-conversion luminescence intensity is more efficient, when the ytterbium ions are in the core [VI]. The reason for this might be the inability of the atmospheric impurities (*e.g.* OH^-) to disturb the excitation energy absorption of the ytterbium if it is located in the core. The impurities can also weaken the luminescence of the erbium activator ions, but the effect seems to be rather insignificant.

The homogeneous $NaYF_4$:Yb^{3+},Er^{3+} material produces stronger luminescence than the core-shell Na(Y,Yb)F_4-$NaErF_4$ when annealed at 400 °C (Fig. 51) [VI]. The weak luminescence of the core-shell nanomaterial is probably due to the concentration quenching of Er^{3+} emission and/or the long distance between the Yb^{3+} sensitizer and the Er^{3+} activator ions weakening the Yb^{3+}-Er^{3+} energy transfer. Also the low annealing temperature might prevent the diffusion, and in this case, despite the concentration gradient, the optically active ions cannot move towards more favorable places for the up-conversion luminescence.

The low I_{red}/I_{green} ratio (Fig. 52) of the core-shell Na(Y,Yb)F_4-$NaErF_4$ (T: 400 °C) is due to the lack of the cross-relaxation processes [VI]. The lowest I_{red}/I_{green} ratio of the materials annealed at 600 °C is observed with the homogeneous $NaYF_4$:Yb^{3+},Er^{3+}. This is due to the random location of the erbium ions in the R^{3+} sites of the $NaYF_4$ host lattice. The high I_{red}/I_{green} ratio of the Na(Y,Yb)F_4-$NaErF_4$ material may be due to the cross-relaxation processes of the erbium ions (Fig. 52). These are enhanced by the high Er^{3+} concentration in the shell layer, which improves the probability of the cross-relaxation processes and increases the red luminescence intensity as well as decreases the green one.

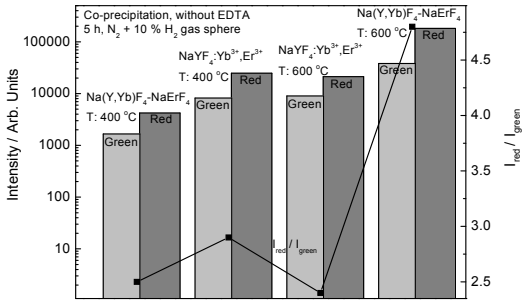

Figure 52. Red-to-green up-conversion luminescence intensity ratios of the homogeneous $NaYF_4$:Yb^{3+},Er^{3+} and core-shell Na(Y,Yb)F_4-$NaErF_4$ nanomaterials prepared with co-precipitation [VI].

4.9. Up-conversion luminescence decay

4.9.1. Y_2O_2S:Yb^{3+},Er^{3+}

The analysis of the red up-conversion luminescence decay curves (Fig. 53) revealed that the Y_2O_2S:Yb^{3+},Er^{3+} materials prepared with the flux method achieve the saturation point during the 20 ms excitation process. The longest feeding process with the material with the lowest Er^{3+} concentration (x_{Er}: 0.005) is due to the weak absorption of the NIR photons by Yb^{3+} and the low

probability of the energy transfer to the Er^{3+} ion. This, in turn, is due to the long distance between the Yb^{3+} and Er^{3+} ions. For the other materials, the higher concentrations of the Er^{3+} ions make the energy transfer process easier.

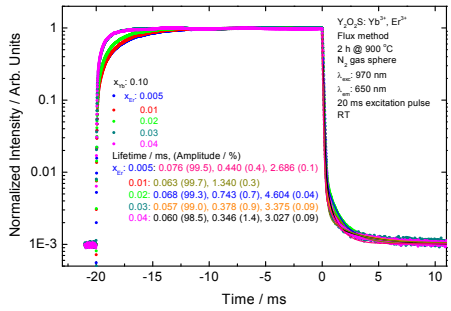

Figure 53. Red up-conversion luminescence decays of the $Y_2O_2S:Yb^{3+},Er^{3+}$ nanomaterials prepared with the flux method.

The short lifetimes (Table 3) of the $Y_2O_2S:Yb^{3+},Er^{3+}$ nanomaterials are due to the small particle size (70-110 nm) and large surface area to which the impurities (*e.g.* CO_2, H_2O, NO_3^-) can be absorbed from the atmosphere. These impurities can cause several side processes, which can cause the short luminescence lifetime.

Table 3. Up-conversion luminescence lifetimes of the $Y_2O_2S:Yb^{3+},Er^{3+}$ nanomaterials.

x_{Er}	Lifetime τ_1 / ms (Amplitude / %)	Lifetime τ_2 / ms (Amplitude / %)	Lifetime τ_3 / ms (Amplitude / %)
0.005	0.076 (99.5)	0.440 (0.40)	2.686 (0.1)
0.01	0.063 (99.7)	1.340 (0.3)	
0.02	0.068 (99.3)	0.743 (0.7)	4.604 (0.04)
0.03	0.057 (99.0)	0.378 (0.9)	3.375 (0.09)
0.04	0.060 (98.5)	0.346 (1.4)	3.027 (0.09)

4.9.2. ZrO_2:$(Y^{3+},)Yb^{3+},Er^{3+}$

The analysis of the red up-conversion luminescence decay curves of the $ZrO_2:Yb^{3+},Er^{3+}$ materials prepared with the combustion synthesis revealed that the saturation is achieved during the 20 ms feeding process (Fig. 54). For these $ZrO_2:Yb^{3+},Er^{3+}$ materials, the high concentrations of the Yb^{3+} and Er^{3+} ions (x_{Yb}: 0.10 and x_{Er}: 0.04, respectively) make the energy transfer process rather easy.

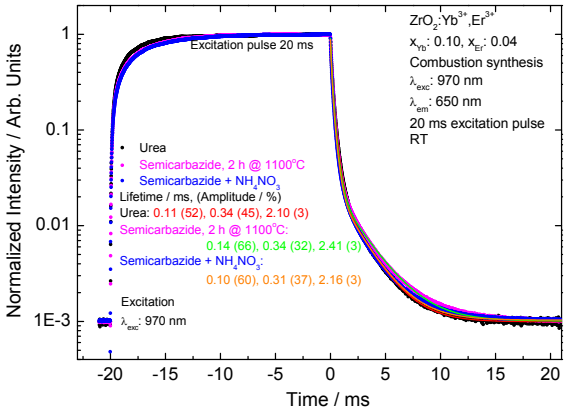

Figure 54. Red up-conversion luminescence decays of the ZrO_2:Yb^{3+},Er^{3+} nanomaterials prepared with the combustion synthesis.

ZrO_2:Yb^{3+},Er^{3+} has been observed to show persistent up-conversion luminescence, *i.e.* a combination of up-conversion and persistent luminescence [I,III,VIII]. When it was tried to enhance the persistent up-conversion luminescence without weakening the up-conversion luminescence intensity, Y^{3+} ions were doped in the ZrO_2:Yb^{3+},Er^{3+} materials to create more oxygen vacancies by charge compensation [IV]. The analysis of the up-conversion luminescence decay curves (Fig. 55) revealed that for the material with the lowest Yb^{3+} and Er^{3+} concentrations (x_{Yb}: 0.05, x_{Er}: 0.02, curve 1), the luminescence feeding process does not achieve the saturation point during the excitation process of five ms. This is due to the weak absorption of the NIR photons by Yb^{3+} and the low probability of the energy transfer to the Er^{3+} ion. This is, in turn, due to the long distance between the Yb^{3+} and Er^{3+} ions. For the other materials, the higher concentrations of the Yb^{3+} and Er^{3+} ions (x_{Yb}: 0.10 and x_{Er}: 0.04, respectively) make the energy transfer process easier. The saturation point for the material with the highest Y^{3+} concentration (x_Y: 0.42, curve 5) is achieved easily because of the formation of the Yb^{3+}-Y^{3+} pairs instead of the Yb^{3+}-Er^{3+} (or Yb^{3+}-Yb^{3+}) pairs. The up-conversion luminescence is rather weak, however, since only very few isolated Yb^{3+} and Er^{3+} ions (or, most probably, Yb^{3+}-Er^{3+}) contribute to the up-conversion.

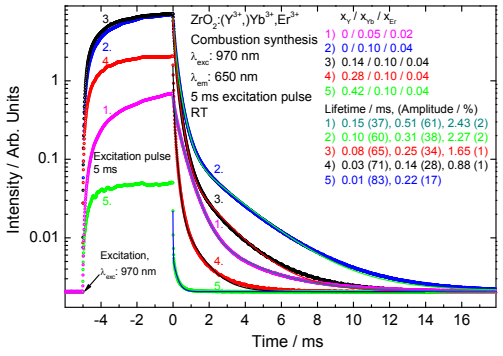

Figure 55. Red up-conversion luminescence decays of the ZrO_2:(Y^{3+},)Yb^{3+},Er^{3+} nanomaterials prepared with the combustion synthesis [IV].

In general, it is observed that the lower is the yttrium concentration the stronger is the up-conversion luminescence (Fig. 55) [IV]. This is due to the easier Yb^{3+}-Er^{3+} pair formation with lower yttrium concentration. With higher yttrium concentrations, the yttrium isolates the ytterbium and erbium ions from each other. This makes the energy transfer more difficult and causes the weak luminescence. There is no significant difference in the saturation times between the material with the lowest yttrium concentration compared to the corresponding material doped with Yb^{3+} and Er^{3+} only.

There are at least two different lifetimes (Table 4) for the red up-conversion luminescence at 650 nm (Fig. 55) [IV]. The short luminescence lifetimes fall in the range of 100 to 350 µs which is quite typical for the conventional Er^{3+} luminescence. The shortest luminescence lifetime is observed for the material with the highest yttrium concentration (x_Y: 0.42, curve 5). This is due to the presence of strong competing processes, probably involving energy transfer to oxygen vacancies formed by the Y^{3+} addition. These vacancies are thus acting as traps. The longer "short" luminescence lifetimes for the other Yb^{3+} and Er^{3+} doped materials indicate that such competing processes are of minor importance and underline the importance of the Y^{3+} doping in creation of energy storing traps.

Table 4. Up-conversion luminescence lifetimes of the ZrO_2:(Y^{3+},)Yb^{3+},Er^{3+} nanomaterials.

x_Y / x_{Yb} / x_{Er}	Lifetime τ_1 / ms (Amplitude / %)	Lifetime τ_2 / ms (Amplitude / %)	Lifetime τ_3 / ms (Amplitude / %)
0 / 0.05 / 0.02	0.15 (37)	0.51 (61)	2.43 (2)
0 / 0.10 / 0.04	0.10 (60)	0.31 (38)	2.27 (2)
0.14 / 0.10 / 0.04	0.08 (65)	0.25 (34)	1.65 (1)
0.28 / 0.10 / 0.04	0.03 (71)	0.14 (28)	0.88 (1)
0.42 / 0.10 / 0.04	0.01 (83)	0.22 (17)	

The long-duration part of the Er^{3+} decays extends well beyond 10 ms for the different ZrO_2:Yb^{3+},Er^{3+} materials (Fig. 55) [IV]. The relatively intense afterglow indicates that the energy stored in the traps created by the R^{3+} doping can be recovered later. This afterglow can be called "persistent up-conversion". However, it seems that the Y^{3+} addition cannot enhance that the use of the energy stored and this energy is predominantly lost. This is evident from the curves 3 to 5 (Fig. 52). Although the Y^{3+} co-doping should enhance the formation of the R^{3+}-R^{3+} pairs in the ZrO_2 host material; these may predominantly be the Y^{3+}-Y^{3+} pairs, not the Yb^{3+}-Er^{3+} or Yb^{3+}-Yb^{3+} ones with utility to the up-conversion luminescence. The less there are rare earth dopants in the material the longer is the luminescence lifetime.

4.9.3. $NaYF_4$:Yb^{3+},Er^{3+}

4.9.3.1. Homogeneous materials

The materials prepared with co-precipitation show slow feeding processes (Fig. 56). The strongest up-conversion luminescence intensity is obtained with the $NaYF_4$:Yb^{3+},Er^{3+} nanomaterial with the highest annealing temperature (700 °C, Fig. 56, left). This material shows also the longest luminescence lifetime (*ca.* 7 ms). This is due to the color centers which can cause the trapping of the excitation energy in the system followed by thermal bleaching of this energy and feeding to a

luminescence center finally causing the persistent up-conversion luminescence. The shortest lifetime (*ca.* 0.4 ms) is obtained with the nanomaterial annealed at 200 °C. This is due to the small particle size (*ca.* 80 nm) and large surface area to which the impurities (*e.g.* OH^-) can be absorbed from the atmosphere. These impurities can cause several side processes, which, in turn, can cause the short luminescence lifetime.

When annealed in selected gas spheres, the longest lifetime was obtained with N_2 (Fig. 56, right). This is due to the lack of the color centers caused by oxygen in air or hydrogen in the N_2 + 10 % H_2 gas sphere, which can cause the slightly shorter luminescence lifetimes.

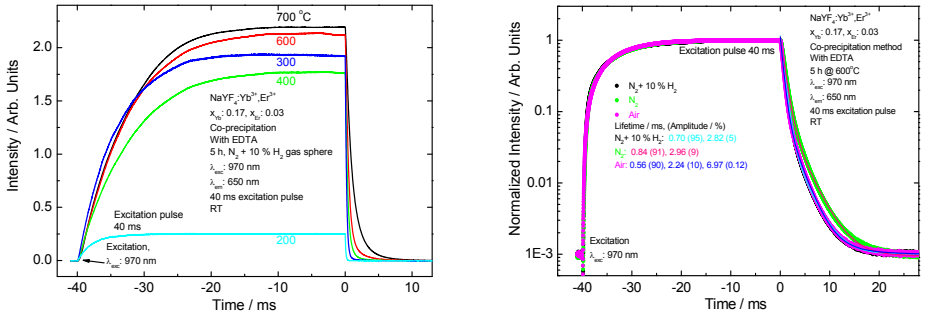

Figure 56. Red up-conversion luminescence decay measurements of the homogeneous $NaYF_4:Yb^{3+},Er^{3+}$ nanomaterials prepared with co-precipitation and annealed at selected temperatures (prepared with EDTA, left) and gas spheres (prepared without EDTA, right).

The red up-conversion luminescence decay curves reveal that the luminescence feeding process is very slow with the $NaYF_4:Yb^{3+},Er^{3+}$ nanomaterials prepared with the solvothermal synthesis (Fig. 57) [V].

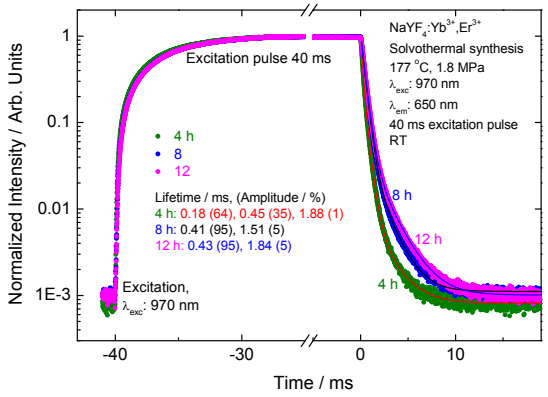

Figure 57. Red up-conversion luminescence decay measurements of the homogeneous $NaYF_4:Yb^{3+},Er^{3+}$ nanomaterials prepared with the solvothermal synthesis [V].

The saturation point is achieved not until the excitation of *ca.* 25 ms. The feeding processes of the materials with selected reaction times are almost similar. The long-duration part of the Er^{3+} decays extends beyond 10 ms for the different $NaYF_4$:Yb^{3+},Er^{3+} materials. The relatively intense afterglow of the material with the reaction time of 12 h indicates that the material is well crystallized and the amount of the side processes is small. This afterglow can be called “persistent up-conversion”. The short afterglow (*ca.* 7 ms) of the material with reaction time of 4 h is due to the poorly crystallized structure and the large amount of the side processes.

4.9.3.2. Core-shell materials

The materials prepared with co-precipitation show slow feeding processes (Fig. 58) [VI]. The strongest up-conversion luminescence intensity is obtained with the Na(Y,Yb)F_4-$NaErF_4$ core-shell nanomaterial with the highest annealing temperature (600 °C). This material shows also the longest luminescence lifetime (over 20 ms). This is due to the color centers which can cause the trapping of the excitation energy in the system followed by thermal bleaching of this energy and feeding to a luminescence center finally causing the persistent up-conversion luminescence. The shortest lifetime (*ca.* 15 ms) is obtained with the Na(Y,Yb)F_4-$NaErF_4$ core-shell nanomaterial annealed at 400 °C. This is due to the small particle size (*ca.* 80 nm) and large surface area to which the impurities (*e.g.* OH^-) can be absorbed from the atmosphere. These impurities can cause several side processes, which, in turn, can cause the short luminescence lifetime.

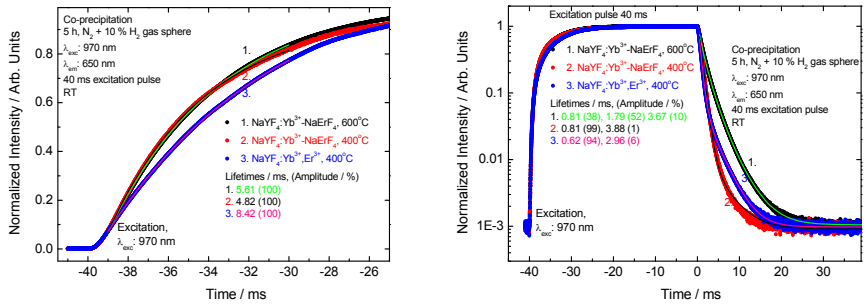

Figure 58. Red up-conversion luminescence decay measurements of the homogeneous $NaYF_4$:Yb^{3+},Er^{3+} and core-shell Na(Y,Yb)F_4-$NaErF_4$ nanomaterials prepared with co-precipitation [VI].

4.10. Thermoluminescence

As discussed above, the presence of the Er^{3+} ions and Yb^{3+} in the Zr^{IV} site (Er'_{Zr} and Yb'_{Zr}) requires charge compensation. The creation of Zr vacancies (V''''_{Zr}) is very improbable and thus the widely accepted option for charge compensation in the ZrO_2:R^{3+} are the oxide vacancies ($V^{\bullet\bullet}_O$). On the other hand, a similar decrease in the negative charge can be achieved by substituting oxide with hydroxide (OH^-) ions which, due to the low temperature synthetic method and aqueous media, are omnipresent. Energetically, the defects with a positive net charge ($V^{\bullet\bullet}_O$ or $OH^{\bullet}_O$) are considered to be

located close to the conduction band, while negatively charged defects (as cation vacancies or R'_{Zr}) are close to the valence band, which gives them the possibility to act as electron and hole traps, respectively.

In order to probe the existence of defects (traps), thermoluminescence (TL) glow curves were measured from room temperature up to 400 °C. Although it is very difficult to relate the origin and type of the defects to the details of the glow curves, at least the mere presence of them gives important information. The glow curve of the $ZrO_2:Yb^{3+},Er^{3+}$ nanomaterial shows a wide band with moderate intensity between 50 and 225 °C with a shoulder at 170 °C (Fig. 59) [VIII]. The weakness of the TL emission may be due to the weak detection in the red spectral region rather than to the weak emission itself. The deconvolution of the glow curve results in three traps with depths of 0.68, 0.85 and 1.03 eV. For efficient (regular) persistent luminescence, the main TL band is usually observed close to but below 100 °C, *e.g.* at 90 for $Sr_2MgSi_2O_7:Eu^{2+},R^{3+}$ [*e.g.* 206]. The TL results thus suggest that $ZrO_2:Yb^{3+},Er^{3+}$ has a rather ideal trap structure, but the TL intensity, *i.e.* the trap density, may not be as high as needed for really efficient persistent luminescence.

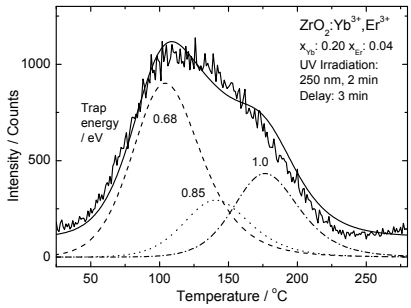

Figure 59. Thermoluminescence glow curve of the $ZrO_2:Yb^{3+},Er^{3+}$ nanomaterial [VIII].

4.11. Persistent up-conversion luminescence mechanism

As indicated by the TL measurements, there are vacancies (together with impurities, *e.g.*, OH^- groups) present in the $ZrO_2:Yb^{3+},Er^{3+}$ nanomaterials mainly due to the charge mismatch between the trivalent Yb^{3+} (and Er^{3+}) and the tetravalent Zr^{IV} ions [VIII]. Similar defects are known to store energy in the persistent luminescence materials (*e.g.* Eu^{2+}-doped alkaline earth aluminates and silicates) [207] as well as in the photostimulated materials (*e.g.* Eu^{2+}-doped BaF(Cl,Br)) [208]. As a further proof to the existence of persistent luminescence for either Yb^{3+}- or Er^{3+}- doped materials, experimental data for strong afterglow have been found from Yb^{3+}-doped garnets (YAG:Yb^{3+}, YbAG) [209,210], Si:Er^{3+} and oxysulfides ($Y_2O_2S:R^{3+}$, R: Ce-Nd, Sm-Yb, $Gd_2O_2S:Er^{3+}$ [211,212]. It can thus be assumed that the persistent up-conversion in the $ZrO_2:Yb^{3+},Er^{3+}$ nanomaterials is possible. Since there are two possible candidates, Yb^{3+} and Er^{3+}, it is of theoretical interest to find out which of these two may be involved in the persistent luminescence. The chemical behavior of these two rare earth ions is, however, rather different: Yb^{3+} can be reduced with relative ease (just after Eu^{3+} in the R^{3+} series) whereas Er^{3+} is a typical R^{3+} ion with no tendency to divalent or tetravalent state. An obvious

analogy can thus be drawn between the chemical behavior of Yb^{3+} and Eu^{3+}, both of which possess the stable divalent form, though massively more stable for europium.

The analogous chemical behavior is not, however, a sufficient proof for similar luminescence behavior. For the construction of the persistent up-conversion luminescence mechanism in the ZrO_2:Yb^{3+},Er^{3+} nanomaterials, the following knowledge, discussed above in detail, is required: the nature of the luminescent center(s), the persistent emission energy, the band gap energy as well as the nature and depths of the energy storage traps [VIII]. Furthermore, the location of the ground level of the emitting ion in the host band gap needs to be established.

Based on an empirical model [213], the location of any R^{2+} 4f ground level in the band structure of a material can be determined since these positions for different R^{2+} are close to host-independent, The most convenient R^{2+} is Eu^{2+} though any other R^{2+} is eligible, as well. For Eu^{2+}, the location of the 4f ground level is obtained from the energy of the charge transfer (CT) transition of $O^{2-}\rightarrow Eu^{3+}$ which two energy values are the same - as a first approximation - if *e.g.* relaxation energies are neglected. The value used here (4.95 eV, 40 000 cm^{-1}, 250 nm) is that reported earlier for ZrO_2:Eu^{3+} [214]. The R^{3+} 4f ground level locations follow a tendency similar to the one for R^{2+} but the energy difference for these two curves depends on the particular host. Data reported for $SrAl_2O_4$ [215] was used to place the position of the Eu^{3+} 4f ground level 5.8 eV below the Eu^{2+} one, in accordance with the approximate value of *ca.* 6 eV for oxide materials. The said empirical model was then used to obtain the locations of the Er^{3+} and Yb^{3+} 4f ground levels, while the excited level energies were obtained from earlier results [216] utilizing semiempirical calculations valid for all R^{3+} within an accuracy of a few 100 cm^{-1} that is largely sufficient for present considerations. As a result of the application of this model, the $^4f_{13}$ ground level $^2F_{7/2}$ of Yb^{3+} is located in the valence band of the ZrO_2 host (Fig. 60) which information is of importance when the charge carriers in persistent luminescence systems are considered [VIII]. Equally important is to observe that the Er^{3+} 4f ground level is well above the top of the valence band, at *ca.* 5000 cm^{-1}.

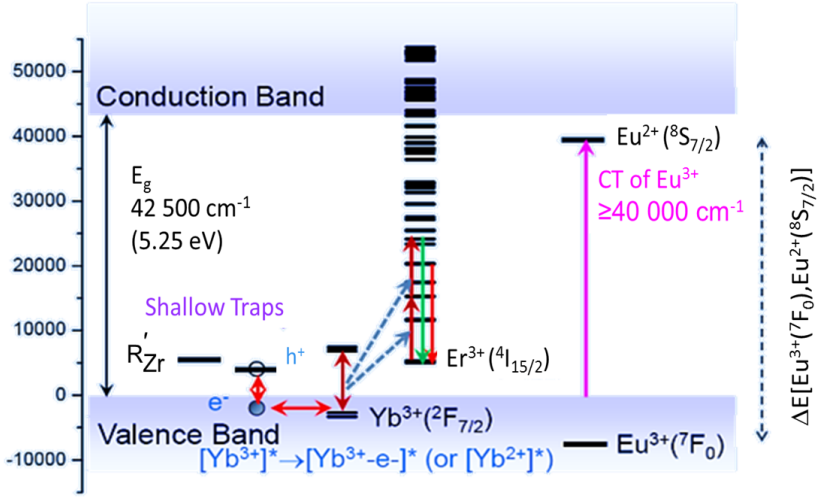

Figure 60. The mechanism of the persistent up-conversion luminescence [VIII].

The mechanism for the persistent up-conversion luminescence in ZrO_2:Yb^{3+},Er^{3+} nanomaterials is as follows (Fig. 60): initially, the Yb^{3+} is excited by NIR radiation exposure involving the transition from the $^2F_{7/2}$ ground state to the excited $^2F_{5/2}$ level [VIII]. Then a part of the excited energy is transferred to erbium and regular up-conversion luminescence is observed. Alternatively, some of the excited energy can be stored in the traps. Since the decay time of Yb^{3+} emission is 3 to 10 times that of Er^{3+}, it is more probable that the energy storage occurs in the vicinity of Yb^{3+} than Er^{3+}. Similarly to the Eu^{3+} persistent luminescence [217], the charge carriers are holes created in the valence band of ZrO_2 due to the formation of an Yb^{3+}-e- pair (or less probably Yb^{2+}). The holes are trapped to shallow traps immediately above the valence band with a release of thermal energy. The Yb^{3+} at the excited $^2F_{5/2}$ level is frozen until the trapped holes are released. The probability of trapping the excitation energy in this manner can be assumed to be a few orders of magnitude lower than the energy transfer to Er^{3+} since the persistent up-conversion luminescence is weak and its duration short. Other factors leading to similar results are: 1) the low mobility of holes in the valence band thus restricting the trapping process to the vicinity of ytterbium and 2) the consequent easy recombination. In contrast, the number of possible hole traps, Yb'_{Zr} is very high and should promote the persistent up-conversion luminescence. The actual luminescence involves the reverse process of freeing the holes from the traps to Yb^{3+} *via* the valence band of ZrO_2 by thermal energy. This process precedes the energy transfer to Er^{3+} and the radiative relaxation of excited Er^{3+} thus creating persistent up-conversion luminescence.

5. CONCLUSIONS

The flux method, the sol-gel, combustion and solvothermal syntheses as well as the co-precipitation method enabled the preparation of the pure nanocrystalline up-conversion phosphors. The heating temperature affected strongly on the $Y_2O_2S:Yb^{3+},Er^{3+}$ particle size, varying between 10 and 110 nm. The combustion synthesis was found to be an efficient way to prepare the nanocrystalline up-converting $ZrO_2:Yb^{3+},Er^{3+}$ luminescence materials with cubic ZrO_2 structure with the particle size of 20-40 nm. The sol-gel synthesis yielded $ZrO_2:Yb^{3+},Er^{3+}$ material with slightly larger crystallite sizes (*ca.* 50 nm) with monoclinic and cubic structures. The monoclinic phase was due to the too low rare earth dopant concentration to stabilize the cubic structure. The heating temperature affected the structure of the $NaYF_4:Yb^{3+},Er^{3+}$ nanomaterials producing a low temperature cubic phase below 400, hexagonal between 400 and 600 and a high temperature cubic one at 700 °C. The $NaYF_4:Yb^{3+},Er^{3+}$ nanomaterials prepared with co-precipitation were mainly spherical, whereas in the materials prepared with the solvothermal synthesis there were also large rod-like particles. This is due to the NaF to Y^{3+} molar ratio affecting the morphology of the hexagonal $NaYF_4$ crystals.

The $Na(Y,Yb)F_4$-$NaErF_4$ core-shell nanomaterials were a mixture of the hexagonal and high temperature cubic forms with the annealing temperature of 600 °C. This reveals that a relatively low annealing temperature is needed for obtaining the high temperature cubic form in the core-shell materials. The inhomogeneous Er distribution in the $Na(Y,Yb)F_4$-$NaErF_4$ (T: 400 °C) core-shell nanomaterial is probably due to the Er located only in the shell layer. This is due to the lack of the diffusion induced mixing of the layers at such a low temperature. The homogeneous Er distribution in the core-shell $Na(Y,Yb)F_4$-$NaErF_4$ (T: 600 °C) material may be due to the (at least a partial) mixing of the layers by diffusion of the Yb^{3+} and Er^{3+} ions.

The XANES measurements of the $NaYF_4:Yb^{3+},Er^{3+}$ and $Na(Y,Yb)F_4$-$NaErF_4$ nanomaterials show that there was only trivalent erbium and ytterbium as expected. Distance distributions calculated from EXAFS correspond well to expected distances and Er and Yb are on their regular sites in the $NaRF_4$ structure. The Er-F distance of the core-shell material (2.32) differs slightly from the other R-F distances (*ca.* 2.35 Å). This reveals that maybe there is a core-shell structure, but the differences are very small.

The $Y_2O_2S:Yb^{3+},Er^{3+}$ nanomaterials demonstrated strong red ($^4F_{9/2}\rightarrow{}^4I_{15/2}$) and moderate green ($^2H_{11/2},{}^4S_{3/2})\rightarrow{}^4I_{15/2}$ up-conversion luminescence under infrared excitation. Due to the cross-relaxation processes, as the crystallite size decreased, the green up-conversion luminescence intensity decreased more than the red one. Also the intensity of the green luminescence decreases, as the erbium concentration increases.

All the $ZrO_2:Yb^{3+},Er^{3+}$ materials showed rather efficient red up-conversion luminescence with broad features due to the multiple Er^{3+} sites originating from different charge compensation schemes because of aliovalent substitution. As a result of the structural purity, the combustion route yielded products with the highest luminescence intensity. The red/green intensity ratio was found to increase with the decreasing crystallite size due to the weakening of the green luminescence. This may be due to a very complex relaxation process involving the multiphonon and cross-relaxation as well as energy trapping caused by lattice defects. The multiphonon relaxation process must be the

dominating relaxation process of the green luminescence because of the efficient red luminescence observed.

The luminescence decay characteristics with at least two different lifetimes in the range typical of Er^{3+} luminescence agreed with the multisite nature of the ZrO_2 lattice. The materials obtained with different methods showed considerable differences in the longer lifetimes. Moreover, severe afterglow, *i.e.* persistent up-conversion luminescence, was observed for the products of the combustion route indicating the inherent energy storage capability of the ZrO_2:(Y^{3+},)Yb^{3+},Er^{3+} materials.

The $NaYF_4$:Yb^{3+},Er^{3+} nanomaterials produced very strong green and red up-conversion luminescence. The strongest total up-conversion luminescence was obtained from the material annealed at 700 °C due to the large crystallite size. In the up-conversion luminescence spectra, the bands corresponding to different transitions of Er^{3+} have different shapes when annealed at different temperatures. This is due to the different structures of the materials: the cubic and hexagonal phases have different arrangement of anions, *i.e.* different crystal field, around the luminescence Er^{3+} centers. Also the low and high temperature cubic materials have different shapes of the luminescence bands; this reveals that $NaYF_4$ has two different cubic structures.

The concentration quenching or the long distance between Yb and Er weakens the up-conversion luminescence intensity in the core-shell Na(Y,Yb)F_4-$NaErF_4$ materials. The low I_{red}/I_{green} ratio with the homogeneous $NaYF_4$:Yb^{3+},Er^{3+} is due to the lack of the cross-relaxation processes caused by the random location of the erbium ions in the R^{3+} sites of the $NaYF_4$ host lattice. The longest decay observed with Na(Y,Yb)F_4-$NaErF_4$ (T: 600 °C) is due to the color centers which causes the persistent up-conversion luminescence, whereas the shortest decay is observed with Na(Y,Yb)F_4-$NaErF_4$ (T: 400 °C) due to the impurities which can cause several side processes.

However, the differences in up-conversion luminescence intensities and lifetimes are strongly affected by the particle size, which makes different nanomaterials difficult to compare. Also the reproducibility of the nanomaterials was a challenge causing batch-to-batch variations of the up-conversion luminescence properties.

For efficient use in bioassays, more work is needed to yield nanomaterials with smaller and more uniform crystallite sizes. More work is also needed with the reproducibility of the materials, because only that way more liable results can be obtained. Surface modifications need to be studied to allow for the dispersion in water. Further work is needed to reveal the details of the persistent up-conversion luminescence, too, but already by now the mechanism is qualitatively consistent with the experimental findings. It also provides a major breakthrough in the understanding of the origin of the persistent up-conversion luminescence.

REFERENCES

1. Williams, F., *Theoretical Basis for Solid-State Luminescence*, in: Goldberg, P. (Ed.), *Luminescence in Inorganic Solids,* Academic Press, New York, USA, 1966, p. 2.
2. Auzel, F., *C.R. Acad. Sci. B Paris* **262** (1966) 1016-1019.
3. Auzel, F., *C.R. Acad. Sci. B Paris* **263** (1966) 819-821.
4. Ovsyankin, V. and Feofilov, P.P., *Jetp. Lett.* **3** (1966) 317-318.
5. Auzel, F., *J. Lumin.* **45** (1990) 341-345.
6. Auzel, F., *Chem. Rev.* **104** (2004) 139-173.
7. Mita, Y., In: Shionoya, S. and Yen, W.M. (Eds.) *Phosphor Handbook*, CRC Press, Boca Raton, FL, USA, 1999, pp. 643-650.
8. Bloembergen, N., *Phys. Rev. Lett.* **2** (1959) 84-85.
9. Snitzer, E. and Woodcock, R., *Appl. Phys. Lett.* **6** (1965) 45-46.
10. Nakazawa, E. and Shionoya, S., *Phys. Rev. Lett.* **25** (1970) 1710-1712.
11. Kleinman, D.A., *Phys. Rev.* **128** (1962) 1761-1775.
12. Kaiser, W. and Garrett, C.G.B., *Phys. Rev. Lett.* **7** (1961) 229-231.
13. Chivian, J.S., Case, W., and Eden, D.D., *Appl. Phys. Lett.* **35** (1979) 124-125.
14. Joubert, M., Guy, S., and Jacquier, B., *Phys. Rev. B* **48** (1993) 10031-10037.
15. Zou, X. and Izumitani, T., *J. Non-Cryst. Solids* **162** (1993) 68-80.
16. Rao, D.N., Prasad, J., and Prasad, P.N., *Phys. Rev. B* **28** (1983) 20-23.
17. Brown, M. and Shand, W.A., *J. Phys. C: Solid State Phys.* **4** (1971) 83-92.
18. Patra, A., Friend, C.S., Kapoor, R., and Prasad, P.N., *J. Phys. Chem. B* **106** (2002) 1909-1912.
19. Salley, G.M., Valiente, R., and Güdel, H.U., *J. Lumin.* **94-95** (2001) 305-309.
20. Jacquier, B., Linarès, C., Mahiou, R., Adam, J.L., Dénoue, E., and Lucas, J., *J. Lumin.* **60-61** (1994) 175-178.
21. Suyver, J.F., Aebischer, A., Biner, D., Gerner, P., Grimm, J., Heer, S., Krämer, K.W., Reinhard, C., and Güdel, H.U., *Opt. Mater.* **27** (2005) 1111-1130.
22. Auzel, F., *Proc. IEEE* **61** (1973) 758-786.
23. Song, F., Zhang, G., Shang, M., Tan, H., Yang, J., and Meng, F., *Appl. Phys. Lett.* **79** (2001) 1748-1750.
24. Yeh, D.C., Sibley, W.A., Suscavage, M., and Drexhage, M.G., *J. Appl. Phys.* **62** (1987) 266-275.
25. Pollnau, M., Gamelin, D.R., Lüthi, S.R., Güdel, H.-U., and Hehlen, M.P., *Phys. Rev. B* **61** (2000) 3337-3346.
26. Suyver, J.F., Aebischer, A., García-Revilla, S., Gerner, P., and Güdel, H.U., *Phys. Rev. B* **71** (2005) 125123 (9 pages).
27. Grubb, S.G., Bennett, K.W., Cannon, R.S., and Humer, W.F., *Electron. Lett.* **28** (1992) 1243-1244.
28. Downing, E., Hesselink, L., Ralston, J., and Macfarlane, R., *Science* **273** (1996) 1185-1189.
29. Finkel, J.R., Jacobs, P.F., Gustafson, K.I., and Green, W.D., US Patent 4678322, 1987.
30. Van de Rijke, F., Zijlmans, H., Li, S., Vail, T., Raap, A.K., Niedbala, R.S., and Tanke, H.J., *Nat. Biotechnol.* **19** (2001) 273-276.
31. Zijlmans, H.J.M.A.A., Bonnet, J., Burton, J., Kardos, K., Vail, T., Niedbala, R.S., and Tanke, H.J., *Anal. Biochem.* **267** (1999) 30-36.
32. Wright, W.H., Mufti, N.A., Tagg, N.T., Webb, R.R., and Schneider, L.V., *Proc. SPIE* **2985** (1997) 248-255.
33. Misra, S.N., Gagnani, M.A., Devi, I., and Shukla, R.S., *Bioinorg. Chem. Appl.* **2** (2004) 155-192.
34. Mathis, G. *Clin. Chem.* **39** (1993) 1953-1959.
35. Zijlstra, W.G., Buursma, A., and Meeuwsen-van der Roest, W.P., *Clin. Chem.* **37** (1991) 1633-1638.
36. Soini, E., Meltola, N.J., Soini, A.E., Soukka, J., Soini, J.T., and Hänninen, P.E., *Biochem. Soc. Trans.* **28** (2000) 70-74.
37. Soukka, T., Kuningas, K., Rantanen, T., Haaslahti, V., and Lövgren, T., *J. Fluoresc.* **15** (2005) 513-528.
38. Kuningas, K., Rantanen, T., Ukonaho, T., Lövgren, T., and Soukka, T., *Anal. Chem.* **77** (2005) 7348-7355.
39. Kuningas, K., Rantanen, T., Lövgren, T., and Soukka, T., *Anal. Chim. Acta* **543** (2005) 130-136.
40. Wang, F. and Liu, N., *Chem. Soc. Rev.* **38** (2009) 976-989.
41. Stouwdam, J.W. and Van Veggel, F.C.J.M., *Nano Lett.* **2** (2002) 733-737.
42. Kane, J., PCT Int. Appl. (1996) WO 96/01297.
43. Mho, S.-I., Chang, S.-Y., Jeon, C.-I., Puyn, C.-H., Won Choi, Q., and Kim, C.-H., *Bull. Korean Chem. Soc.* **11** (1990) 386-390.

44. Singh, V., Kumar Rai, V., Ledoux-Rak, I., Watanabe, S., Gundu Rao, T.K., Chubaci, J.F.D., Badie, L., Pellé, F., and Ivanova, S., *J. Phys. D: Appl. Phys.* **42** (2009) 065104 (9 pages).

45. McKittrick, J., Shea, L.E., Bacalski, C.F., and Bosze, E.J., *Displays* **19** (1999) 169-172.

46. Ekambaram, S., Patil, K.C., and Maaza, M., *J. Alloys Comp.* **393** (2005) 81-92.

47. Tukia, M., Hölsä, J., Lastusaari, M., and Niittykoski, J., *Opt. Mater.* **27** (2005) 1516-1522.

48. Zych, E., *Opt. Mater.* **16** (2001) 445-452.

49. Vetrone, F., Boyer, J.C., Capobianco, J.A., Speghini, A., and Bettinelli, M., *J. Appl. Phys.* **96** (2004) 661-667.

50. Ye, T., Guiwen, Z., Weiping, Z., and Shangda, X., *Mat. Res. Bull.* **32** (1997) 501-506.

51. Díaz-Torres, L.A., De la Rosa-Cruz, E., Salas, P., and Angeles-Chavez, C., *J. Phys. D: Appl. Phys.* **37** (2004) 2489-2495.

52. De la Rosa, E., Díaz-Torres, L.A., Salas, P., and Rodriquez, R.A., *Opt. Mater.* **27** (2005) 1320-1325.

53. Salas, P., Angeles-Chávez, C., Montoya, J.A., De la Rosa, E., Díaz-Torres, L.A., Desirena, H., Martinez, A., Romero-Romo, M.A., and Morales, J., *Opt. Mater.* **27** (2005) 1295-1300.

54. Yi, G., Lu, H., Zhao, S., Ge, Y., Yang, W., Chen, D., and Guo, L.-H., *Nano Lett.* **4** (2004) 2191-2196.

55. Yi, G., Sun, B., Chen, D., Zhou, Y., Cheng, J., Yang, W., Ge, Y., and Guo, L., US Patent 20060003466A1, 2006.

56. Chen, Z., Chen, H., Hu, H., Yu, M., Li, F., Zhang, Q., Zhou, Z., Yi, T., and Huang, C., *J. Am. Chem. Soc.* **130** (2008) 3023-3029.

57. Zhang, Q. and Zhang, Q.-M., *Mater. Lett.* **63** (2009) 376-378.

58. Liu, X., Zhao, J., Sun, Y., Song, K., Yu, Y., Du, C., Kong, X., and Zhang, H., *Chem. Comm.* (2009) 6628-6630.

59. Wang, M., Liu, J.-L., Zhang, Y.X., Hou, W., Wu, X.-L., and Xu, S.-K., *Mater. Lett.* **63** (2009) 325-327.

60. Tessari, G., Bettinelli, M., Speghini, A., Ajó, D., Pozza, G., Depero, L.E., Allieri, B., and Sangaletti, L., *Appl. Surf. Sci.* **144-145** (1999) 686-689.

61. Capobianco, J.A., Vetrone, F., Boyer, J.C., Speghini, A., and Bettinelli, M., *J. Phys. Chem. B* **106** (2002) 1181-1187.

62. Vetrone, F., Boyer, J.C., Capobianco, J.A., Speghini, A., and Bettinelli, M., *J. Phys. Chem. B* **107** (2003) 1107-1112.

63. Hirai, T. and Orikoshi, T., *J. Colloid Interface Sci.* **269** (2004) 103-108.

64. Shang, Q., Yu, H., Kong, X., Wang, H., Wang, X., Sun, Y., Zhang, Y., and Zeng, Q., *J. Lumin.* **128** (2008) 1211-1216.

65. Zhang, J., Wang, X., Zheng, W.-T., Kong, X.-G., Sun, Y.-J., and Wang, X., *Mater. Lett.* **61** (2007) 1658-1661.

66. Patra, A., Friend, C.S., Kapoor, R., and Prasad, P.N., *Appl. Phys. Lett.* **83** (2003) 284-286.

67. Suyver, J.F., Grimm, J., Van Veen, M.K., Biner, D., Krämer, K.W., and Güdel, H.U., *J. Lumin.* **117** (2006) 1-12.

68. Liang, X., Wang, X., Zhuang, J., Peng, Q., and Li, Y., *Adv. Funct. Mater.* **17** (2007) 2757-2765.

69. Wang, F., Han, Y., Lim, C.S., Lu, Y., Wang, J., Xu, J., Chen, H., Zhang, C., Hong, M., and Liu, X., *Nature* **463** (2010) 1061-1065.

70. Boyer, J.-C., Vetrone, F., Cuccia, L.A., and Capobianco, J.A., *J. Am. Chem. Soc.* **128** (2006) 7444-7445.

71. Mai, H.-X., Zhang, Y.-W., Sun, L.-D., and Yan, C.-H., *J. Phys. Chem. C* **111** (2007) 13730-13739.

72. Mai, H.-X., Zhang, Y.-W., Si, R., Yan, Z.-G., Sun, L.-D., You, L.-P., and Yan, C.-H., *J. Am. Chem. Soc.* **128** (2006) 6426-6436.

73. Wang, L., Li, P., and Li, Y., *Adv. Mater.* **19** (2007) 3304-3307.

74. Aebischer, A., Heer, S., Biner, D., Krämer, K., Haase, M., and Güdel, H.U., *Chem. Phys. Lett.* **407** (2005) 124-128.

75. Hebert, T., Wannemacher, R., Lenth, W., and Macfarlane, R.M., *Appl. Phys. Lett.* **57** (1990) 1727-1729.

76. Pollnau, M., Lüthy, W., Weber, H.P., Krämer, K., Güdel, H.U., and McFarlane, R.A., *Appl. Phys. B* **62** (1996) 339-344.

77. Yin, M., Makhov, V.N., Khaidukov, N.M., and Krupa, J.C., *J. Alloys Comp.* **341** (2002) 362-365.

78. Bouffard, M., Duvaut, T., Jouart, J.P., Khaidukov, N.M., and Joubert, M.F., *J. Phys.: Condens. Matter* **11** (1999) 4775-4782.

79. Nuñez, N.O., Quintanilla, M., Cantelar, E., Cussó, F., and Ocaña, M., *J. Nanopart. Res.* **12** (2010) 2553-2565.

80. Wang, G., Qin, W., Wei, G., Wang, L., Zhu, P., Kim, R., Zhang, D., Ding, F., and Zheng, K., *J. Fluorine Chem.* **130** (2009) 158-161.

81. Wang, Y., Qin, W., Zhang, J., Cao, C., Zhang, J., and Jin, Y., *J. Rare Earths* **26** (2008) 40-43.

82. Sivakumar, S., Van Veggel, FC.J.M., and May, P.S., *J. Am. Chem. Soc.* **129** (2007) 620-625.

83. Yi, G.-S., and Chow, G.-M., *J. Mater. Chem.* **15** (2005) 4460-4464.

84. Sudarsan, V., Sivakumar, S., Van Veggel, F.C.J.M., and Raudsepp, M., *Chem. Mater.* **17** (2005) 4736-4742.

85. Sivakumar, S., Van Veggel, F.C.J.M., and Raudsepp, M., *J. Am. Chem. Soc.* **127** (2005) 12464-12465.

86. Pushkar, A.A., Uvarova, T.V., and Kiiko, V.V., *Optics and Spectroscopy* **111** (2011) 273-276.

87. Kaminskii, A.A., Butashin, A.V., Hulliger, J., Egger, P., Bagayev, S.N., Eichler, H.J., Findeisen, J., Liu, B., Täuber, U., Peuser, P., and Sulyanov, S.N., *J. Alloys Comp.* **275-277** (1998) 442-446.

88. Jouart, J.P., Bouffard, M., Klein, G., and Mary, G., *J. Lumin.* **60-61** (1994) 93-96.

89. Fernández, J., Sanz, M., Mendioroz, A., Balda, R., Chaminade, J.P., Ravez, J., Lacha, L.M., Voda, M., and Arriandiaga, M.A., *J. Alloys Comp.* **323-324** (2001) 267-272.

90. Smith, A., Martin, J.P.D., Sellars, M.J., Manson, N.B., Silversmith, A.J., and Henderson, B., *Opt. Comm.* **188** (2001) 219-232.

91. Russell, D.L., Henderson, B., Chai, B.H., Nicholls, J.F.H., and Holliday, K., *Opt. Comm.* **134** (1997) 398-406.

92. Holliday, K., Russell, D.L., and Henderson, B., *J. Lumin.* **72-74** (1997) 927-929.

93. Grimm, J., Wenger, O.S., Krämer, K.W., and Güdel, H.U., *J. Lumin.* **126** (2007) 590-596.

94. Wenger, O.S., Salley, G.M., and Güdel, H.U., *J. Phys. Chem. B* **106** (2002) 10082-10088.

95. Hubert, S., Song, C.L., Genet, M., and Auzel, F., *J. Solid State Chem.* **61** (1986) 252-259.

96. Joubert, M.F., Guy, S., Cuerq, S., and Tanner, P.A., *J. Lumin.* **75** (1997) 287-293.

97. Wenger, O. and Güdel, H.U., *J. Phys. Chem. B* **106** (2002) 10011-10019.

98. Dereń, P.J., Stręk, W., Zych, E., and Drożdżyński, J., *Chem. Phys. Lett.* **332** (2000) 308-312.

99. Güdel, H.U. and Pollnau, M., *J. Alloys Comp.* **303-304** (2000) 307-315.

100. Wermuth, M. and Güdel, H.U., *J. Lumin.* **87-89** (2000) 1014-1016.

101. Wermuth, M. and Güdel, H.U., *Chem. Phys. Lett.* **323** (2000) 514-521.

102. Pollnau, M., Gamelin, D.R., Lüthi, S.R., Güdel, H.U., and Hehlen, M.P., *Phys. Rev. B* **61** (2000) 3337-3346.

103. Salley, G.M., Wenger, O.S., Krämer, K.W., and Güdel, H.U., *Curr. Opin. Solid State Mater. Sci.* **6** (2002) 487-493.

104. Han, J., Zhou, G., Zhang, S., Cheng, Z., and Chen, H., *Chinese Sci. Bull.* **45** (2000) 981-984.

105. Shannon, R.D., *Acta Cryst. A* **32** (1976) 751-767.

106. Ong, L.C., Gnanasammandhan, M.K., Nagarajan, S., and Zhang, Y., *Luminescence* **25** (2010) 290-293.

107. Liu, G.K., Chen, X.Y., Zhuang, H.Z., Li, S., and Niedbala, R.S., *J. Solid State Chem.* **171** (2003) 123-132.

108. Pires, A., Serra, O.A., and Davolos, M.R., *J. Alloys Comp.* **374** (2004) 181-184.

109. Hirai, T. and Orikoshi, T., *J. Colloid Interface Sci.* **273** (2004) 470-477.

110. Luo, X.-X. and Cao, W.-H., *Mater. Lett.* **61** (2007) 3696-3700.

111. Pires, A.M., Heer, S., Güdel, H.U., and Serra, O.A., *J. Fluoresc.* **16** (2006) 461-468.

112. Garskaite, E., Lindgren, M., Einarsrud, M.-A., and Grande, T., *J. Eur. Ceram. Soc.* **30** (2010) 1707-1715.

113. Heer, S., Wermuth, M., Krämer, K., Ehrentraut, D., and Güdel, H.U., *J. Lumin.* **94-95** (2001) 337-341.

114. Chen, X., Collins, J., DiBartolo, B., Bowlby, B., Dinerman, B., and Weyburne, D., *J. Lumin.* **72-74** (1997) 168-170.

115. Speghini, A., Piccinelli, F., and Bettinelli, M., *Opt. Mater.* **33** (2011) 247-257.

116. Venkatramu, V., Falcomer, D., Speghini, A., Bettinelli, M., and Jayasankar, C.K., *J. Lumin.* **128** (2008) 811-813.

117. Lee, S., Teshima, K., Shikine, N., and Oishi, S., *Cryst. Growth Design* **9** (2009) 4078-4083.

118. Rapaport, A., David, V., Bass, M., Deka, C., and Boatner, L.A., *J. Lumin.* **85** (1999) 155-161.

119. Heer, S., Lehmann, O., Haase, M., and Güdel, H.-U., *Angew. Chem. Int. Ed.* **42** (2003) 3179-3182.

120. Ghosh, P., Oliva, J., De la Rosa, E., Haldar, K.K., Solis, D., and Patra, A., *J. Phys. Chem. C* **112** (2008) 9650-9658.

121. Li, Z., Zheng, L., Zhang, L., and Xiong, L., *J. Lumin.* **126** (2007) 481-486.

122. Du, Y.-P., Zhang, Y.-W., Sun, L.-D., and Yan, C.-H., *J. Phys. Chem. C* **112** (2008) 405-415.

123. Li, A., Sun, L., Zheng, Z., Liu, W., Wu, W., Yang, Y., and Lv, T., *Appl. Phys. A* **89** (2007) 1005-1010.

124. Zhang, D.-L., Hua, P.-R., Cui, Y.M., Chen, C.-H., and Pun, E.Y.B., *J. Lumin.* **127** (2007) 453-460.

125. Sokólska, I., Kück, S., Dominiak-Dzik, G., and Baba, M., *J. Alloys Comp.* **323-324** (2001) 273-278.

126. Sokólska, I., *J. Alloys Comp.* **341** (2002) 288-293.

127. Chen, X. and Zhang, G., *Opt. Comm.* **102** (1993) 293-296.

128. Chen, X.B., Zhang, G.Y., Mao, Y.H., Hou, Y.B., Feng, Y., and Hao, Z., *J. Lumin.* **69** (1996) 151-160.

129. Meneses-Nava, M.A., Barbosa-García, O., Maldonado, J.L., Ramos-Ortíz, G., Pichardo, J.L., Torres-Cisneros, M., García-Hernández, M., García-Murillo, A., and Garrillo-Romo, F.J., *Opt. Mater.* **31** (2008) 252-260.

130. Battisha, I.K., Badr, Y., Shash, N.M., El-Shaarawy, M.G., and Darwish, A.G.A., *J. Sol-Gel Sci. Technol.* **53** (2010) 543-550.

131. Patra, A., Friend, C.S., Kapoor, R., and Prasad, P.N., *Chem. Mater.* **15** (2003) 3650-3655.

132. Yi, G., Sun, B., Yang, F., Chen, D., Zhou, Y., and Cheng, J., *Chem. Mater.* **14** (2002) 2910-2914.

133. Chen, W., Joly, A.J., and Zhang, J.Z., *Phys. Rev. B* **64** (2001) 041202 (4 pages).

134. Li, X., Liu, B., Li, Z., Li, Q., Zou, Y., Liu, D., Li, D., Zou, B., Cui, T., and Zou, G., *J. Phys. Chem. B* **113** (2009) 4737-4740.

135. Wang, H., Tu, C., You, Z., Yang, F., Wie, Y., Wang, Y., Li, J., Zhu, Z., Jia, G., and Lu, X., *Appl. Phys. B* **88** (2007) 57-60.

136. Galceran, M., Pujol, M.C., Zaldo, C., Díaz, F., and Aguiló, M., *J. Phys. Chem. C* **113** (2009) 15497-15506.

137. Lisiecki, R., Ryba-Romanowski, W., Cavalli, E., and Bettinelli, M., *J. Lumin.* **130** (2010) 131-136.

138. Lisiecki, R., Ryba-Romanowski, W., and Lukasiewicz, T., *Appl. Phys. B* **81** (2005) 43-47.

139. De Camargo, A.S.S., Nunes, L.A.O., Silva, J.F., Costa, A.C.F.M., Barros, B.S., Silva, J.E.C., De Sá, G.F., and Alves Jr, S., *J. Phys.: Condens. Matter* **19** (2007) 246209 (7 pages).

140. Lü, W., Ma, X., Zhou, H., Chen, G., Li, J., Zhu, Z., You, Z., and Tu, C., *J. Phys. Chem. C* **112** (2008) 15071-15074.

141. Brenier, A., Jurdyc, A.M., Verweij, H., Cohen-Adad, M.T., and Boulon, G., *Opt. Mater.* **5** (1996) 233-238.

142. Heer, S., Kömpe, K., Güdel, H.-U., and Haase, M*., Adv. Mater.* **16** (2004) 2102-2105.

143. Krämer, K.W., Biner, D., Frei, G., Güdel, H.U., Hehlen, M.P., and Lüthi, S.R., *Chem. Mater.* **16** (2004) 1244-1251.

144. Blasse, G. and Grabmaier, B.C., *Luminescent Materials*, Springer-Verlag, Berlin, Germany, 1994, pp. 10-32, 195-202.

145. Bai, X., Song, H., Pan, G., Lei, Y., Wang, T., Ren, X., Lu, S., Dong, B., Dai, Q., and Fan, L., *J. Phys. Chem. C* **111** (2007) 13611-13617.

146. Strohhöfer, C. and Polman, A., *Opt. Mater.* **21** (2003) 705-712.

147. Ohwaki, J. and Wang, Y., *Appl. Phys. Lett.* **65** (1994) 129-131.

148. Ohwaki, J. and Otsuka, M., *Electron. Lett.* **31** (1995) 752-753.

149. Sommerdijk, J.L., *J. Lumin.* **6** (1973) 61-67.

150. Gamelin, D.R. and Güdel, H.U., *Top. Curr. Chem.* **214** (2001) 1-56.

151. Auzel, F., In: Hull, R., Parisi, J., Osgood, R.M., Warlimont, H., Liu, G., and Jacquier, B. (Eds.), *Spectroscopic Properties of Rare Earths in Optical Materials*, Berlin, Heidelberg, Germany, 2005, pp. 266-319.

152. Yi, G. and Chow, G., *Adv. Funct. Mater.* **16** (2006) 2324-2329.

153. Ehlert, O., Thomann, R., Darbandi, M., and Nann, T., *ACS Nano* **2** (2008) 120-124.

154. Li, W.-J., Zhou, S.-M., Liu, N., Lin, H., Teng, H., Li, Y.-K., Hou, X.-R., and Jia, T.-T., *Mater. Lett.* **64** (2010) 1344-1346.

155. Kasprowicz, D., Brik, M.G., Majchrowski, A., Michalski, E., and Głuchowski, P., *Opt. Mater.* **33** (2011) 1595-1601.

156. Sun, C., Lü, W., Yang, F., and Tu, C., *J. Alloys Comp.* **512** (2012) 160-164.

157. Hölsä, J., Laihinen, T., Laamanen, T., Lastusaari, M., Pihlgren, L., Rodrigues, L.C.V., and Soukka, T., *Physica B* **439** (2014) 20-23.

158. Gamelin, D.R. and Güdel, H.U., *J. Phys. Chem. B* **104** (2000) 10222-10234.

159. Gamelin, D.R. and Güdel, H.U., *Inorg. Chem.* **38** (1999) 5154-5164.

160. Wermuth, M. and Güdel, H.U., *Chem. Phys. Lett.* **281** (1997) 81-85.

161. Wermuth, M. and Güdel, H.U., *J. Am. Chem. Soc.* **121** (1999) 10102-10111.

162. Vuojola, J., Luminescent Lanthanide Reporters: New Concepts for Use in Bioanalytical Applications, Ph.D. Thesis, University of Turku, 2013, pp. 36-40.

163. Sun, L.N., Peng, H., Stich, M.I., Achatz, D., and Wolfbeis, O.S., *Chem. Comm.* **33** (2009) 5000-5002.

164. Sedlmeier, A., Achatz, D.E., Fischer, L.H., Gorris, H.H., and Wolfbeis, O.S., *Nanoscale* **4** (2012) 7090-7096.

165. Mader, H.S. and Wolfbeis, O.S., *Anal. Chem.* **82** (2010) 5002-5004.

166. Achatz, D.E., Meier, R.J., Fischer, L.H., and Wolfbeis, O.S., *Angew. Chem. Int. Ed.* **50** (2011) 260-263.

167. Zhou, J., Yu, M., Sun, Y., Zhang, X., Zhu, X., Wu, Z., Wu, D., and Li, F., *Biomaterials* **32** (2011) 1148-1156.

168. Kuningas, K., Towards Photoluminescence-Based Homogeneous Immunoassays in Whole-Blood: Up-Converting Inorganic Lanthanide Phosphors as Novel Reporters, Ph.D. Thesis, University of Turku, 2007, p. 33.

169. Mita, Y., Hirama, K., Ando, N., Yamamoto, H., and Shionoya, S., *J. Appl. Phys.* **74** (1993) 4703-4709.

170. Robinson, M., Pastor, R.C., Turk, R.R., Devor, D.P., and Braunstein, M., *Mat. Res. Bull.* **15** (1980) 735-742.

171. Rodríguez, V.D., Méndez-Ramos, J., Tikhomirov, V.K., Del-Castillo, J., Yanes, A.C., and Moshchalkov, V.V., *Opt. Mater.* **34** (2011) 179-182.

172. Zhao, S., Xu, S., Jia, G., Deng, D., Huang, L., and Wang, H., *Mater. Lett.* **65** (2011) 2407-2409.

173. Antal, T., Harju, E., Pihlgren, L., Lastusaari, M., Tyystjärvi, T., Hölsä, J., and Tyystjärvi, E., *Int. J. Hydrogen Energy,* **37** (2012) 8859-8863.

174. Allakhverdiev, S.I., Thavasi, V., Kreslavski, V.D., Zharmukhamedov, S,K., Klimov, V.V., Ramakrishna, S., Los, D.A., Mimuro, M., Nishihara, H., and Carpentier, R., *J. Photochem. Photobiol. C Photochem. Rev.* **11** (2011) 101-113.

175. Hallenbeck, P.C. and Benemann, J.R., *Int. J. Hydrogen Energy* **27** (2002) 1185-1193.

176. Melis, A. and Melnicki, M.R., *Int. J. Hydrogen Energy* **31** (2006) 1563-1573.

177. Kraus, W. and Nolze, G., POWDER CELL FOR WINDOWS, VERSION 2.4, *Federal Institute for Materials Research and Testing*, Berlin, Germany, 2000.

178. PCPDFWIN v. 1.30, 1997, Powder Diffraction File, International Centre for Diffraction Data, entries 24-1424 (Y_2O_2S), 33-1286 ($Na_2S_2O_4$), 27-0997 (cubic ZrO_2), 37-1484 (monoclinic ZrO_2), 42-1164 (tetragonal ZrO_2), 06-0342 (cubic $NaYF_4$), 28-1192 (hexagonal $Na(Y_{0.57}Yb_{0.39}Er_{0.04})F_4$), and 36-1355 (NaF).

179. Klug, H.P. and Alexander, L.E., *X-ray powder diffraction procedures*, Wiley, New York, 1959, p. 491.

180. George, G.V. and Pickering, I.J.*, EXAFSPAK, A suite of computer programs for analysis of X-ray absorption spectra, SSRL, Stanford University, Stanford, CA, USA, 1993.*

181. Chung, K.S., TL Glow Curve Analyzer v. 1.0.3. (Korea Atomic Energy Research Institute and Gyeongsang National University, Korea, 2008).

182. Karppinen, M., Kyläkoski, P., Niinistö, L., and Rodellas, C., *J. Thermal Anal.* **35** (1989) 347-353.

183. Hölsä, J. and Turkki, T., *Thermochim. Acta* **190** (1991) 335-343.

184. Nakamoto, K., *Infrared and Raman Spectra of Inorganic and Coordination Compounds*, Wiley, New York, USA, 1986, pp. 101-152.

185. Hyppänen, I., Hölsä, J., Kankare, J., Lastusaari, M., Pihlgren, L., and Soukka, T., *J. Fluoresc.* **18** (2008) 1029-1034.

186. Arppe, R., Hyppänen, I., Hölsä, J., Kankare, J., Lastusaari, M., Pihlgren, L., Soukka, T., and Vuojola, J., *unpublished results.*

187. Wang, M., Huang, Q.-L., Hong, J.-M., Wu, W.-H., Yu, Z., Chen, X.-T., and Xue, Z.-L., *Solid State Commun.* **136** (2005) 210-214.

188. Zachariasen, W.H., *Acta Crystallogr.* **2** (1949) 60-62.

189. Gupta, T.K., Bechtold, J.H., Kuznicki, R.C., Cadoff, L.H., and Rossing, B.R., *J. Mater. Sci.* **12** (1977) 2421-2426.

190. Ho, S.M., *Mater. Sci. Eng.* **54** (1982) 23-29.

191. Dexpert-Ghys, J., Faucher, M., and Caro, P., *J. Solid State Chem.* **54** (1984) 179-192.

192. Vegard, L., *Z. Phys.* **5** (1921) 17-26.

193. Thoma, R.E., Insley, H., and Hebert, G.M., *Inorg. Chem.* **5** (1966) 1222-1229.

194. Sobolev, B.P., *The Rare Earth Trifluorides* (Barcelona, Spain: Institut d'Estudis Catalans), 2000, pp. 214-220.

195. Burns, J.H., *Inorg. Chem.* **4** (1965) 881-886.

196. Mathews, M.D., Ambekar, B.R., Tyagi, A.K., and Köhler, J., *J. Alloys Comp.* **377** (2004) 162-166.

197. Hyppänen, I., Hölsä, J., Kankare, J., Lastusaari, M., Nunes, L.A.O., Pihlgren, L., and Soukka, T., MAX-lab Activity Report 2010, pp. 308-309.

198. Martin, U., Boysen, H., and Frey, F., *Acta Cryst. B* **49** (1993) 403-413.

199. Tuilier, M.H., Dexpert-Ghys, J., Dexpert, H., and Lagarde, P., *J. Solid State Chem.* **69** (1987) 153-161.

200. Harju, E., Hölsä, J., Kankare, J., Laamanen, T., Lastusaari, M., Malkamäki, M., Pihlgren, L., Soukka, T., and Welter, E., HASYLAB Annual Report, 2009, Materials Science (http://hasylab.desy.de/annual_report/files/2009/2009763.pdf).

201. Zakaria, D., Mahiou, R., Avignant, D., and Zahir, M., *J. Alloys Comp.* **257** (1997) 65-68.

202. Pässler, R., *Phys. Stat. Sol. (b)* **236** (2003) 710-728.

203. Livraghi, S., Olivero, F., Paganini, M.C., and Giamello, E., *J. Phys. Chem. C* **114** (2010) 18553-18558.

204. Hyppänen, I., Hölsä, J., Kankare, J., Lastusaari, M., Malkamäki, M., and Pihlgren, L., *J. Lumin.* **129** (2009) 1739-1743.

205. Batalhão, T.B., Hyppänen, I., Hölsä, J., Kankare, J., Lastusaari, M., Malkamäki, M., Nunes, L.A.O., Pihlgren, L., and Soukka, T., *unpublished results.*

206. Brito, H.F., Hassinen, J., Hölsä, J., Jugner, H., Laamanen, T., Lastusaari, M., Malkamäki, M., Niittykoski, J., Novák, P., and Rodrigues, L.C.V., *J. Therm. Anal. Cal.* **105** (2011) 657-662.

207. Aitasalo, T., Hölsä, J., Jungner, H., Lastusaari, M., and Niittykoski, J., *J. Phys. Chem. B* **110** (2006) 4589-4598.

208. Schweizer, S., *Phys. Stat. Sol. (a)* **187** (2001) 335-393.

209. Guerassimova, N., Garnier, N., Dujardin, C., Petrosyan, A.G., and Pedrini, C., *J. Lumin.* **94-95** (2001) 11-14.

210. Guerassimova, N., Garnier, N., Dujardin, C., Petrosyan, A.G., and Pedrini, C., *Chem. Phys. Lett.* **339** (2001) 197-202.

211. Forcales, M., Gregorkiewicz, T., Bradley, I.V., and Wells, J.-P.R. *Phys. Rev. B* **65** (2002) 195208, 8 pages.

212. Zhang, J., Liu, Y.-L., and Man, S., *J. Lumin.* **117** (2006) 141-146.

213. Dorenbos, P., *J. Lumin.* **108** (2004) 301-305.

214. Dhiren Meetei, S., Dorendrajit Singh, S., Shanta Singh, N., Sudarsan, V., Ningthoujam, R.S., Tyagi, M., Gadkari, S.C., Tewari, R., and Vatsa, R.K., *J. Lumin.* **132** (2012) 537-544.

215. Dorenbos, P. and Bos, A.J.J., *Radiation Measurements* **43** (2008) 139-145.

216. Hölsä, J., Lamminmäki, R.-J., Lastusaari, M., and Porcher, P., *unpublished results*.

217. Hölsä, J., Brito, H.F., Laamanen, T., Lastusaari, M., Malkamäki, M., and Rodrigues, L.C.V., Proc. 16th Int. Conf. Lumin. (ICL'11), Ann Arbor, MI, USA, June 26-July 1, 2011, pp. 71-72.